CHARGE TRANSFER BY ELECTRONIC EXCITATION: HIGH RESOLUTION MEASUREMENTS VIA ROTATIONALLY RESOLVED SPECTROSCOPY IN THE GAS PHASE

by

Adam Joseph Fleisher

B.S., Elizabethtown College, 2007

Submitted to the Graduate Faculty of

Arts and Sciences in partial fulfillment

of the requirements for the degree of

Doctor of Philosophy

University of Pittsburgh

2011

UNIVERSITY OF PITTSBURGH

ARTS AND SCIENCES

This dissertation was presented

by

Adam Joseph Fleisher

It was defended on

August 15, 2011

and approved by

Committee Members:

Dr. David H. Waldeck, Professor and Department Chair
Department of Chemistry, University of Pittsburgh

Dr. Kenneth D. Jordan, Distinguished Professor of Computational Chemistry
Director of the Center for Simulation and Modeling
Department of Chemistry, University of Pittsburgh

Dr. David F. Plusquellic, Research Physical Chemist
Optical Technology Division
National Institute of Standards and Technology

Dissertation Advisor:

Dr. David W. Pratt, Professor
Department of Chemistry, University of Pittsburgh

CHARGE TRANSFER BY ELECTRONIC EXCITATION: HIGH RESOLUTION MEASUREMENTS VIA ROTATIONALLY RESOLVED SPECTROSCOPY IN THE GAS PHASE

Adam Joseph Fleisher, Ph.D.

University of Pittsburgh, 2011

Understanding the intricate molecular motions that occur in solvents is a scientific challenge for many fields, including biology, chemistry, and physics. Solvents are ever-present in living organisms, and may play a vital role in the folding of proteins and nucleic acid chains. Currently, ultrafast spectroscopic techniques are able to map long range networks of hydrogen bonds within the universal solvent water, where hindered motions are important. Presented in this dissertation is a detailed study of several highly resolved frequency spectra, each of which makes a unique contribution to the understanding of molecular structure, intermolecular bonding dynamics, and the forces that stabilize hydrogen bonds in the gas phase. It is here, in an isolated environment, that solute-solvent interactions can be dissected, both experimentally and theoretically, void of perturbations from the bulk.

Among the molecular systems investigated here, the photoacid β-naphthol was studied in the presence of water and ammonia, and the electric dipole moments of each complex were shown to contain intrinsic contributions from intermolecular charge transfer. This charge transfer is present in the ground electronic state, and increases upon excitation with ultraviolet light. Two rotamers of the donor-acceptor system *meta*-aminobenzoic acid have been identified by differences in their moments of inertia and dipole moments, and singly and doubly solvated complexes of this system were observed. The ground, S_1, and S_2 dipole moments of anomalous

dual fluorescence molecules, such as DMABN and phenylpyrrole, have also been determined, and their relevance to condensed phase solvatochromism is discussed.

The work reported here makes use of two ultraviolet laser spectrometers; a pulsed supersonic jet spectrometer, and a high resolution continuous wave molecular beam spectrometer. A wide variety of *ab initio* calculations were performed in support of these experiments.

TABLE OF CONTENTS

PREFACE XXVI

1.0 INTRODUCTION 1

1.1 REFERENCES 4

2.0 INTERNAL AND EXTERNAL PERTURBATIONS IN ELECTRONIC SPECTROSCOPY. THE STARK SPECTRUM OF INDOLE-NH_3. 5

2.1 ABSTRACT 6

2.2 INTRODUCTION 6

2.3 METHODS 7

2.4 RESULTS 10

2.4.1 Fluorescence excitation spectra 10

2.4.2 Theoretical structures and vibrational frequencies 19

2.4.3 Theoretical barrier heights to internal rotation 24

2.5 DISCUSSION 25

2.5.1 Structure of InA in its S_0 and S_1 electronic states 25

2.5.2 Internal rotation dynamics in InA 28

2.5.3 Dipole moments of InA in its S_0 and S_1 electronic states. 29

2.6 SUMMARY 31

2.7 ACKNOWLEDGEMENTS 33

2.8 REFERENCES 33

3.0 CHARGE TRANSFER BY ELECTRONIC EXCITATION: DIRECT MEASUREMENT BY HIGH RESOLUTION SPECTROSCOPY IN THE GAS PHASE .37

3.1 ABSTRACT 38

3.2 COMMUNICATION 38

3.3 ACKNOWLEDGEMENTS 49

3.4 REFERENCES 50

4.0 FLICKERING DIPOLES IN THE GAS PHASE. STRUCTURES, INTERNAL DYNAMICS, AND DIPOLE MOMENTS OF β-NAPHTHOL-H_2O IN ITS GROUND AND EXCITED ELECTRONIC STATES 53

4.1 ABSTRACT 54

4.2 INTRODUCTION 54

4.3 METHODS 56

4.3.1 Experimental 56

4.3.2 Theoretical 58

4.4 RESULTS AND INTERPRETATION 60

4.4.1 Rotationally resolved electronic spectrum 60

4.4.2 Water dynamics 65

4.4.3 Permanent electric dipole moments 70

4.5 DISCUSSION 70

4.5.1 S_0 and S_1 structures of *cis*-2HNW 72

4.5.2 Permanent electric dipole moments 76

4.5.3 Energy and dipole decomposition analysis 83

4.6 CONCLUSION 92

4.7 ACKNOWLEDGEMENTS 93

4.8 REFERENCES 93

5.0 HIGH RESOLUTION ELECTRONIC SPECTROSCOPY STUDIES OF *META*-AMINOBENZOIC ACID IN THE GAS PHASE REVEAL THE ORIGINS OF ITS SOLVATOCHROMIC BEHAVIOUR 97

5.1 ABSTRACT 98

5.2 INTRODUCTION 98

5.3 EXPERIMENTAL SECTION 100

5.3.1 Theory 100

5.3.2 Experiment 101

5.4 RESULTS AND DISCUSSION 103

5.4.1 Theoretical S_0 structures and dipole moments 103

5.4.2 Theoretical S_1 structures and dipole moments 103

5.4.3 Experimental rotational constants, transition moments, and dipole moments 105

5.4.4 Conformational assignment 111

5.4.5 Evaluation of theory 115

5.4.6 Connections with ABA solvatochromism 118

5.5 CONCLUSIONS 122

5.6 ACKNOWLEDGEMENTS 123

5.7 REFERENCES 124

6.0 HIGH RESOLUTION ELECTRONIC SPECTROSCOPY OF THE DOORWAY STATES TO INTRAMOLECULAR CHARGE TRANSFER. GAS PHASE DIPOLE MOMENTS OF BENCHMARK AMINOBENZONITRILE DERIVATIVES. 126

6.1 ABSTRACT 127

6.2 INTRODUCTION 128

6.3 METHODS 131

6.4 RESULTS 133

6.4.1 4-(1*H*-Pyrrol-1-yl)benzonitrile (PBN) 133

6.4.2 4,4′-Dimethylaminobenzonitrile (DMABN) 142

6.4.3 4-(1-Pyrrolidinyl)benzonitrile (PYRBN) 144

6.5 DISCUSSION 148

6.6 SUMMARY 155

6.7 ACKNOWLEDGEMENTS 158

6.8 REFERENCES 158

7.0 EXCITED STATE PROTON TRANSFER IN *SYN*-2-(2′-PYRIDYL)PYRROLE OCCURS ON THE NANOSECOND TIMESCALE IN THE GAS PHASE. 163

7.1 ABSTRACT 164

7.2 COMMUNICATION 164

7.3 ACKNOWLEDGEMENTS 174

7.4 REFERENCES 175

APPENDIX A 177

APPENDIX B 183

APPENDIX C 184

APPENDIX D **186**

APPENDIX E **200**

LIST OF TABLES

Table 2-1. Measured and assigned S_1 origin bands and intermolecular vibrational modes of InA and InA_2. 13

Table 2-2. Experimentally determined rotational constants and fitting parameters of the indole-$(NH_3)_1$ *A* band. 15

Table 2-3. Substitution coordinates (r_s) (Ref. 38) of the indole amino hydrogen atom and the InA ammonia molecule treated as a point mass in the indole-*h* inertial frame. 18

Table 2-4. Theoretical rotational constants, hydrogen bond lengths, ammonia C_3 symmetry axis angles, and low frequency vibrations of InA. An asterisk (*) indicates that no vibrational frequencies were calculated. The vibrational frequencies are not scaled. 20

Table 2-5. Theoretical rotational constants and low frequency vibrations of InA_2. An asterisk (*) indicates that no vibrational frequencies were calculated. The vibrational frequencies are not scaled. 21

Table 2-6. Permanent EDMs of indole, indole-H_2O, and indole-NH_3 in the gas phase. 30

Table 3-1. Experimental permanent EDMs of *cis*-2HN and *cis*-2HNA. The dipole moment angle with respect to the *a* inertial axis is defined as θ_a. 41

Table 3-2. Calculated dipole-dipole, polarizability-electric field, and charge-charge interaction energies of *cis*-2HNA. Below, *cis*-2HN is designated as 1, and NH_3 is designated as 2. The angles θ_1 and θ_2 are the angles that μ_1 and μ_2 make with the line R_{CM} (Ref. 32). 46

Table 4-1. Inertial parameters of *cis*-2HNW. The theoretical constants were calculated using M05-2X/aug-cc-pVDZ in S_0 and CIS/aug-cc-pVDZ in S_1. 63

Table 4-2. Absolute position of water treated as a point mass of 18 atomic mass units (u). The inertial frames of *cis*-2HN (dashed axes) and *cis*-2HNW (solid axes) are shown in Fig. 4-1. All values are in Angstroms (Å). 64

Table 4-3. Second-order torsion-rotation perturbation coefficients $W_{v\sigma}^{(2)}$, internal motion axis angles (α), effective barrier heights (*s*), barrier heights (V_2), and internal rotor constants (*F*) of *cis*-2HNW in each electronic state. 69

Table 4-4. Absolute permanent electric dipole moments of 2HN and 2HN acid-base complexes. The EDMs are shown as projections onto the inertial axes of each molecule or complex. Experimental uncertainty is shown in parenthesis, and is in the last digit. All values are in Debye (D). 71

Table 4-5. Change in rotational constants following excitation to S_1 in naphthalene ring systems. The values of *cis*-2HNW were derived using the structural constants listed in Table 4-1. 73

Table 4-6. Predicted energies of S_1 torsional levels relative to the electronic origin ($S_1 \leftarrow S_0$) of *cis*-2HNW. Transitions are listed using $|v',\sigma'\rangle \leftarrow |v'',\sigma''\rangle$ notation. 76

Table 4-7. Block-localized wavefunction energy decomposition. All values are in wavenumbers (cm^{-1}). 85

Table 4-8. Block-localized wavefunction dipole decomposition. All values are in Debye (D). ...90

Table 5-1. Theoretical rotational constants (MHz), inertial defects ($uÅ^2$), and dipole moments (Debye) of MABA. 104

Table 5-2. Experimentally determined inertial parameters of MABA. Each rotational constant has a standard deviation of 0.1 MHz. S_0 and S_1 rotational constants were varied, along with the origin, to produce the final fits to experiment shown in Figures 5-2 and 5-3. 109

Table 5-3. Measured permanent electric dipole moments of ABAs. In all cases, μ_c was measured as equal to zero. Standard deviations are shown in parentheses. 112

Table 5-4. Theoretical properties of the MABA S_1-S_0 electronic excitation. E is the CASSCF adiabatic excitation energy, and E_{PT2} is the CASPT2 corrected energy. The percentage of reference, single, double, and triple excitation configurations is shown, followed by the natural orbital population of each MO in the active space. SLCs are the single excitations with the largest CI coefficients.....114

Table 5-5. Root mean square deviations of theoretical rotational constants (*A*, *B*, *C*) and dipole moments (μ_a, μ_b) as compared to experiment.[a] Band I is assigned as *cis*-MABA, and Band II is assigned as *trans*-MABA. 116

Table 6-1. Experimental inertial parameters derived from the microwave and UV spectra of PBN. Columns with the headings "Band 1", *etc*. contain the excited electronic state parameters of each respective transition studied in Fig. 6-1. 138

Table 6-2. Experimental inertial parameters derived from the UV spectrum of PYRBN.[a] 146

Table 6-3. Permanent electric dipole moments and twist angles of PP, PBN, ABN, DMABN, and PYRBN measured in the gas phase (first row). Standard deviation is shown in parentheses. Also listed are the available theoretical data for each electronic transition observed (Refs. 41 and 44), second row. 156

Table 7-1. Inertial parameters of 2PP in its ground electronic state.[a] 168

Table 7-2. Inertial parameters of 2PP in its excited electronic state.[a] 169

Table A-1. Predicted V_3 barrier heights (cm^{-1}) using A subband ΔI_{eff} values ($uÅ^2$) from select NH_3 complexes. All predicted V_3 values overestimate the barrier height as compared to V_3 calculated from the first-order perturbation coefficients $W^{(1)}$ determined by fitting the respective E subbands. 180

Table B-1. Theoretical permanent EDMs of *cis*-2HN and *cis*-2HNA. The dipole moment angle with respect to the *a* inertial axis is defined as θ_a. S_0 calculations were done using the MP2 level of theory and the indicated basis set, while S_1 calculations were done using the CIS level of theory. Components of the molecular polarizability tensor for *cis*-2HN are also included. 183

Table C-1. Calculated electrostatic interaction energies of *cis*-2HNW. Below, *cis*-2HN is designated as 1 and H_2O is designated as 2. The angles θ_1 and θ_2 are the angles μ_1 and μ_2 make with the line R_{CM} 184

Table D- 1. Cartesian coordinates of the PYRBN optimized geometry (Å) 187

Table D-2. List of assigned rotational transitions in the Stark CP-FTMW spectrum of DMABN using QSTARK.[4,5] The F and M_F quantum numbers are in units of 1/2, and the frequencies are in MHz. The standard deviation of the fit is 0.057 MHz 190

Table D-3. Calculated rotational constants (A, B, C) in MHz are compared to the experimentally determined values below. Following the M05-2X/6-31+G* optimization, the dipole moment was calculated using MP2 theory (keywords *SCF=Tight* and *Density=Current*)[2] and either a double-ζ (D), triple-ζ (T), or quadruple-ζ (Q) basis set of the form aug-cc-pVXZ where X = D, T, or Q. The percent error in calculated parameters is shown in the column "%". The molecules investigated are abbreviated as follows: AN = aniline,[10] BN = benzonitrile,[11] ABN = 4-aminobenzonitrile,[11] DMABN = 4,4′-dimethylaminobenzonitrile, PYR-eq = pyrrolidine (equatorial conformer),[12] PYRBN = 4-(1-pyrrolidinyl)benzonitrile, P = pyrrole,[13] PP = 1-phenylpyrrole,[14] and PBN = 4-(1*H*-pyrrol-1-yl)benzonitrile 197

Table E-1. Observed frequencies and residuals for the rotational transitions of *syn*-2-(2′-pyridyl)pyrrole 200

LIST OF FIGURES

Figure 2-1. Low resolution fluorescence excitation spectrum (FES) of indole-*h*-NH_3 (InA, top) and indole-*d*-NH_3 (InA-d_4, bottom). 11

Figure 2-2. High resolution FES of the S_1-S_0 origin band of InA (black). The simulated spectrum (blue) reproduces the experimental trace at full rotational resolution, as shown in the bottom panel. 13

Figure 2-3. High resolution Stark spectra of the InA S_1-S_0 origin band recorded at several applied electric fields. The permanent EDMs of InA in S_0 and S_1 were used to simulate (blue) and fit the experimental (black) spectra. 18

Figure 2-4. DFT structures (M05-2X/aug-cc-pVxZ) and assigned vibrational modes of InA (x = Q) and InA_2 (x = T). 23

Figure 2-5. Predicted torsional potential energy surfaces for NH_3 internal rotation about the hydrogen bond in the S_0 state of InA. 26

Figure 2-6. Illustration of the dipole decomposition of InA (black dipole). The dipoles of indole (red), NH_3 (blue), and the induced dipole (orange) are shown above. The induced dipole measurements are preliminary, as ground and excited state calculations of the indole polarizability are still under investigation. 32

Figure 3-1. Shown in (a) is the zero-field origin band of the $S_1 \leftarrow S_0$ electronic spectrum of *cis*-2HN. At full rotational resolution, (b) shows a portion of the zero-field experimental spectrum (black trace) compared with the simulated spectrum (blue trace) using a convoluted line shape and a rotational temperature of 5 K. The most intense transition ($|J'\ K'_a\ K'_c\rangle \leftarrow |J''\ K''_a\ K''_c\rangle$) has

the assigned quantum numbers |854› ← |963›. At applied electric fields of (c) 846 and (d) 1776 V/cm, the simulated spectra using the dipole moment projections listed in Table 3-1 are in excellent agreement with the experiment. 40

Figure 3-2. Shown in (a) is the zero-field origin of the $S_1 \leftarrow S_0$ electronic spectrum of *cis*-2HNA, containing the overlapping *A* and *E* subbands. At full rotational resolution, (b) contains the zero-field experimental spectrum (black trace) compared with the simulated spectrum (blue trace, *A* subband transitions in blue, *E* subband transitions in red) using a convoluted line shape, a rotational temperature of 5 K, and the addition of both simulated subbands. Spectra obtained at (c) 423 and (d) 1269 V/cm are shown along with the spectra simulated using the dipole projections from Table 3-1. 43

Figure 3-3. The S_0 and S_1 dipole moments of *cis*-2HNA (black). This figure illustrates the components of Eq. 3-1, where μ_{c2HN} (red), μ_{NH_3} (blue), μ_{ind} (orange), and μ_{CT} (green) add to reproduce μ_{c2HNA} (black). 47

Figure 4-1. Ground state structure of *cis*-2HNW (M05-2X/aug-cc-pVDZ, see Table 4-1 for rotational constants). The in-plane inertial axes of *cis*-2HNW are shown as solid lines. The corresponding inertial axes of *cis*-2HN are shown as dashed lines. 59

Figure 4-2. The rotationally resolved spectrum of *cis*-2HNW. The A ($\sigma = 0$) subtorsional band is shown in red (relative intensity of 1), while the B ($\sigma = 1$) subtorsional band simulation is shown in blue (relative intensity of 3). At full rotational resolution, the fit of the combined simulation to experiment is excellent. 61

Figure 4-3. Possible locations of the water COM from a Kraitchman's analysis in the ground state of *cis*-2HNW. Water is shown in orange as a point mass. These locations were determined using inertial parameters of *cis*-2HN (Ref. 6) and *cis*-2HNW from this rotationally resolved work.....64

Figure 4-4. Difference in A-B subband splittings between S_1 and S_0 as a function of the S_1 internal motion axis angle, α'. Shown as a solid line is the measured splitting from the

rotationally resolved spectrum of 0.189 cm^{-1} (5673 MHz). The crossing occurs at $\alpha' = 30.6°$, a change of +12.1° following excitation. 69

Figure 4-5. Stark spectra of *cis*-2HNW at full rotational resolution. Each simulation is a sum of A and B sub-band contributions. All simulations were done using the inertial parameters in Table 4-1 and the dipole moments in Table 4-4. 71

Figure 4-6. Illustration of coupled torsion-inversion intermolecular motion in *cis*-2HNW which results in an exchange of H_1 and H_2. 73

Figure 4-7. (a) Dipole moment function of water calculated using the quadratic synchronous transit (QST) method. Blue dots are the 2HN-plane dipole projections of water from point structures. The black trace is a fit of these blue points to an expansion of torsion functions, with the following coefficients; V_4 = -0.239, V_8 = 0.0340, and C = 1.855. (b) Dipole moment function scaled by the probability of water taking on a given orientation as calculated using the QST method and a basis set of free rotor wavefunctions. The black trace is a fit to the data points using the following coefficients: V_2 = 0.157, V_4 = 0.058, V_8 = 0.00146, and C = -0.104. An image of the water dipole precession during internal motion is shown every 45°. 81

Figure 4-8. The S_0 and S_1 dipole moments of *cis*-2HNW. This figure illustrates the components of Eq. 4-7, where μ_{c2HN} (red), $\langle\mu_{H_2O}\rangle$ (blue), μ_{ind} (green), and μ_{CT} (yellow) add to reproduce μ_{c2HNW} (black). 82

Figure 4-9. B3LYP/aug-cc-pVDZ electron density difference contours of 2HNA (a)-(c) and 2HNW (d)-(f). The polarization effect is shown in (a) and (d), the charge transfer in (b) and (e), while (c) and (f) show the combined effect. The same isodensity value (0.003) is used for all the plots, and the colors blue and red represent gains and losses in electron density, respectively. ...89

Figure 5-1. Vibrationally resolved fluorescence excitation spectrum (FES) of MABA. The spectrum closely resembles the combined REMPI spectra of MABA (I and II), MABA-H_2O (W_1), and MABA-$(H_2O)_2$ (W_2) previously reported.[6,17] The transition marked with an asterisk (*) is the electronic origin of pyrimidine, a contaminant in the spectrometer. 106

Figure 5-2. Rotationally resolved FES of MABA I. The experimental spectrum is in black, and the fit simulation is in red. The top panel spans a frequency range of 2.61 cm^{-1}, whereas the middle and bottom panels span only 0.32 cm^{-1}. The Stark effect is shown in the bottom panel.107

Figure 5-3. Rotationally resolved FES of MABA II. The experimental spectrum is shown in black, and the fit simulation is in blue. The top panel spans a frequency range of 2.88 cm^{-1}, whereas the middle and bottom panels span only 0.32 cm^{-1}. The Stark effect is shown in the bottom panel. 108

Figure 5-4. Assigned structures and dipole moments of the MABA rotamers. 117

Figure 5-5. Molecular orbitals and excitation properties of MABA and PABA from the S_1 CASSCF optimized geometries of each isomer. The red and blue (opposite parity) MOs were created in AVOGADRO[25] using an isosurface value of 0.02. Electron density difference maps (EDDMs) were calculated as $(\pi_5)^2 - (\pi_3)^2$ with G03 and rendered in JMOL[26] using an isosurface value of 0.004. Areas of electron density gain upon excitation (black arrow) are shown in purple, and areas of electron density loss are shown in yellow. The electronic transition moment (TM) as estimated from the $(\pi_5 \otimes \pi_3)$ direct product is displayed below each EDDM as a green double-headed arrow.....120

Figure 6-1. Vibrationally resolved fluorescence excitation spectrum (FES) of PBN. The red arrows labeled 1, 2, and 3 identify the bands studied using high resolution FES. Reprinted with permission from *Chemical Physics Letters* (Ref. 33). Copyright 2002 *Elsevier*.....134

Figure 6-2. Rotationally resolved FES of PBN Band 1. The experimental trace shown in black was fit to two simulations, shown below in red and blue.....135

Figure 6-3. Rotationally resolved FES of PBN Band 2. The experimental trace shown in black was fit to a single simulation, shown in blue. The bottom two panels show the effects of an applied electric field on the high resolution spectrum. The blue and green simulations of the Stark spectra appear identical, therefore illustrating the difficulty encountered when trying to independently determine the EDM in each electronic state. 136

Figure 6-4. Rotationally resolved FES of PBN Band 3. The two asterisks identify areas of unassigned intensity found in the experimental spectrum (black trace) that are not accounted for by the simulation (blue trace). The presence of a second electronic band is suspected, as more of these "missing peaks" appear throughout the spectrum of PBN Band 3. 137

Figure 6-5. Plot of ΔI *vs.* ϕ as calculated from the ground state torsional PES shown in Fig. D-4 (blue data points). These data points were fit to a 2nd order polynomial (black curve), and used to determine ϕ for all PBN electronic states. The S_0 and S_1 extrapolations are shown in the figure. 140

Figure 6-6. Rotationally resolved FES of DMABN (Band 5) recorded at an applied electric field of 507 V/cm. The experimental trace is shown in black, and the combined simulation of both *A* (blue sticks) and *G* (red sticks) subbands is shown in blue. 143

Figure 6-7. Rotationally resolved FES of PYRBN. The experimental trace is shown in black, and the simulation is shown in blue. 145

Figure 7-1. Rotationally resolved fluorescence excitation spectrum of the origin band in the S_1-S_0 electronic transition of *syn*-2-(2′-pyridyl)pyrrole (2PP) in the gas phase, at ~ 318 nm. The lower part of the figure shows an expanded scale view of a portion of the P-branch region. The black trace is the experimental spectrum, and the red trace is the simulated spectrum with and without a convoluted line shape function; the vertical lines represent the individual rovibronic transitions responsible for the spectrum. 167

Figure 7-2. Contour fit of the high resolution fluorescence excitation spectrum of the 0,0 + 144 cm^{-1} vibronic band in the S_1-S_0 electronic transition of 2PP. The experimental spectrum is shown in black, and the simulation is shown in blue. 172

Figure A-1. Plot of V_3 *vs.* ΔI_{cor} for the four complexes listed in Table A-1. A best-fit trendline equation is shown in the top left corner. An asterisk (*) indicates an excited S_1 state. 181

Figure C-1. Stark effect in the electronic spectrum of *trans*-2HN at full rotational resolution. The blue trace is simulated using the dipole moments listed in Table 4-4. The most intense transition in the zero field spectrum is assigned the quantum numbers |854› ← |963›. 185

Figure C-2. Experimental ground and excited state dipole moments of *trans* and *cis*-2HN (scale: 1.0 D = 4.0 Å). The center images are the weighted electron density differences upon $S_1 \leftarrow S_0$ excitation calculated at the CIS/6-31G** level. Purple indicates electron density gain upon excitation, whereas yellow indicates electron density loss. 185

Figure D-1. CASSCF(12,10)/D95V molecular orbitals principally involved in the lowest energy π-π* excitation of PYRBN. Orbital populations were taken from the final density matrix. The vertical excitation energy is 4.54 eV, or approximately 36600 cm^{-1}, without corrections for dynamic electron correlation or zero-point energy. 188

Figure D-2. CP-FTMW spectrum of PBN recorded from 6.5 – 17 GHz. 189

Figure D-3. A portion of the Stark CP-FTMW spectrum of DMABN recorded at an applied electric field of 23.7 V/cm. 189

Figure D-4. The ground state PES for ring torsion in PBN is shown in black. Data points rendered blue were calculated at the M05-2X/6-31+G* level from $\phi = 0°$ to $\phi = 90°$, and then extrapolated over the entire 360° shown above. 193

Figure D-5. The ground state PES for ring torsion in PP is shown in black. Data points rendered blue were calculated at the M05-2X/6-31+G* level from $\phi = 0°$ to $\phi = 90°$, and then extrapolated over the entire 360° shown above. The following Eq. D-1 parameters were fit to the blue data points: V_2 = 67, V_{4+} = -210, V_{4-} = -210, V_8 = -38, and C_τ = 698 cm^{-1}. For PP, the V_4 shift is 39.65°. 194

Figure D-6. Plot of ΔI vs. ϕ as calculated from the ground state torsional PES shown in Fig. D-5 (blue data points). These data points were fit to a 2nd order polynomial (black curve), and used to determine ϕ for all PP electronic states. The S_0 and S_1 extrapolations are shown in the figure..194

Figure D-7. Linear dipole function for PBN, showing the high correlation between the measured μ″ and μ′ values determined for PBN band 2 (blue diamonds) and PBN band 3 (red squares). .196

LIST OF SCHEMES

Scheme 1-1 2

Scheme 1-2 3

Scheme 3-1 39

Scheme 4-1 55

Scheme 5-1 99

Scheme 5-2 122

Scheme 6-1 129

Scheme 6-2 153

Scheme 7-1 165

LIST OF EQUATIONS

Equation 2-1 14

Equation 2-2 14

Equation 2-3 16

Equation 2-4 25

Equation 2-5 31

Equation 3-1 44

Equation 3-2 45

Equation 3-3 48

Equation 4-1 62

Equation 4-2 66

Equation 4-3 66

Equation 4-4 66

Equation 4-5 67

Equation 4-6 70
Equation 4-7 77
Equation 4-8 78
Equation 4-9 79
Equation 4-10....79
Equation 4-11....84
Equation 4-12....86
Equation 4-13....86
Equation 4-14....87
Equation 5-1 115
Equation A-1....177
Equation A-2....178
Equation A-3....178
Equation A-4....178
Equation A-5....178
Equation A-6....178
Equation A-7....179

Equation A-8.....179

Equation A-9.....179

Equation A-10.....181

Equation D-1.....192

PREFACE

I am deeply indebted to many wonderful, talented people who have helped me accomplish the experimental measurements presented in this dissertation. I thank my advisor, Dr. David Pratt for his enthusiasm, encouragement, and professional drive. Our daily interactions over the past four years have been delightfully stimulating experiences that I will not soon forget. As an undergraduate student at Elizabethtown College, I also had the pleasure of inspiring conversations and research experiences with Dr. Charles Schaeffer, Jr., and I sincerely thank him for initially tutoring me on the finer points of chemical research.

As a graduate student, my first research experiences where performed under the guidance of several senior graduate student mentors. Dr. Philip Morgan was kind enough to teach me the high resolution instrumentation and spectral fitting procedures. The long hours he spent allowing me to 'just turn knobs' helped to foster a positive environment of laboratory exploration, and for this I can't thank him enough. Dr. Diane Miller spent many hours training me in the analysis and collection of Stark spectra, and without her I would not have enthusiastically investigated many of the Stark projects reported in this dissertation. I also had the pleasure of working with Dr. Leo Alvarez-Valtierra and Dr. John Yi, two encouraging laboratory partners whom I respect immensely, and I acknowledge their help and encouragement.

Throughout the last four years, Justin Young has been an ever-present partner in the lab. He has taught me to be creative, and not to fear challenging experiments. I will always look back

on my time at Pitt, and think fondly of the countless overnight adventures in ‘hires’ that we shared, and I wish to express my sincere gratitude for his help. I have enjoyed working with several other colleagues in the Pratt group, and I thank Dr. Ryan Bird, Dr. Jessica Thomas, Dr. Vanesa Vaquero, Casey Clements, Patrick Walsh, and Valerie Alstadt for numerous conversations, and most importantly, many Thai truck lunches spent together.

To all other colleagues who I may have regrettably forgotten to mention here, I am grateful for the interactions I have shared you. Within the Pitt community, I would like to thank the folks in the 1st and 2nd floor offices, the machine, electronics, and glass shops, and the chemistry stockrooms for their hard work. I also acknowledge the support of Dr. Richard Christie and the entire staff at the Center for Simulations and Modeling for their patience and expertise in all things theoretical.

Finally, I thank my family for unwavering support. Without you, none of my accomplishments would have been possible. To Emily, I love you, and I can’t think of anyone else I would rather have with me throughout the great adventure that is graduate school. I look forward to our time in Colorado, and to whatever else our future may bring.

Best regards, best wishes, and thank you.

Adam J. Fleisher

1.0 INTRODUCTION

Many different materials are capable of undergoing light-induced property changes at the molecular level. Many of them, such as DNA damage caused by overexposure to sunlight, have a noticeable impact on our daily lives. While we as a society are aware of the broad consequences of light driven processes, a full academic understanding of many systems at their smallest cooperative level (often the molecular level) is an active area of sophisticated and revolutionary scientific research in many disciplines. Research connecting chemistry, physics, astronomy, and biology is currently focused on understanding the negative effect overexposure to sunlight has on our DNA,[1] the influence of radiation on chemical reactions in Earth's atmosphere and in outer space,[2,3] the potential use of photosynthetic systems (both naturally occurring and artificial) as controllable energy harnessing resources,[4] and physiologically important protein motions.[5] All of these processes share a common requirement for a precise input of energy, in the form of visible or ultraviolet electromagnetic radiation, to promote electrons within these molecular systems to a higher energy level (known as the "excited state"). In the following introduction, work within the group of Dr. David Pratt centered on aggressively pursuing answers to fundamental questions of molecular biology, physics, and materials science will be presented.

This dissertation is focused on two topics; 1) the influence of internal dynamics and solvation on intermolecular charge transfer reactions, and 2) light-induced changes in the structures and electronic distributions within isolated molecules. As an experimental physical

chemistry group, we utilize high resolution laser techniques in the visible and ultraviolet (UV) portions of the electromagnetic spectrum to interrogate molecules in a cold, collisionless gas phase environment. Our high resolution apparatus is comprised of an argon ion gas laser operating continuously, a modified ring dye laser providing user control of the laser cavity, and an external frequency doubling cavity. These three instruments working together provide UV light of extremely narrow frequency bandwidth, allowing for eigenstate-resolved measurements of molecules and clusters entrained in a molecular beam.

While there is much to learn about the fundamental quantum mechanics of isolated molecules, our experiment is also sensitive to solvation-dependent chromophore changes. As an example, we have studied the electronic properties of the organic photoacid β-naphthol ($C_{10}H_7OH$) in the presence of a single ammonia (NH_3)[6] or water (H_2O)[7] molecule. In these systems, our goal is to quantify the extent to which a single solvent molecule drives the acid-base reactions shown below.

Scheme 1-1

$$R-OH\cdots NH_3 \xrightarrow{light} (R-O)^-\cdots(NH_4)^+$$
$$R-OH\cdots H_2O \xrightarrow{light} (R-O)^-\cdots(H_3O)^+$$

By measuring the dipole moment of the β-naphthol-NH_3 complex before and after its excitation by light, we have determined that the major stabilizing force in complex formation is charge transfer, which is detectable through its minor contribution to the measured dipole moment. This measurement is quantitative, leading to charge transfer values of Q = 0.09 electrons before, and Q = 0.14 electrons after photoexcitation. We have shown this to be a local phenomenon involving the hydroxyl group of β-naphthol and the nitrogen of NH_3.[6,7] In the β-naphthol-H_2O

complex, we also detect a contribution to the dipole moment from charge transfer. However, the motion of H_2O while attached to β-naphthol is extremely complicated, and we are still working on a theoretical interpretation of our experimental results. The H_2O dynamics, which we are able to quantify, show the same intermolecular signatures as found in the spectra of biomolecules in bulk water.[8]

Recently, we have analyzed the photoexcitation of 1-phenylpyrrole (PP), a model charge transfer system in which two unsaturated rings communicate differently before and after the introduction of a UV photon.[9] As seen below, the torsional angle between the phenyl and pyrrole rings changes from $\phi = 36°$ to $20°$ upon excitation, resolving a dispute in the literature concerning the excited state structure of PP.

Scheme 1-2

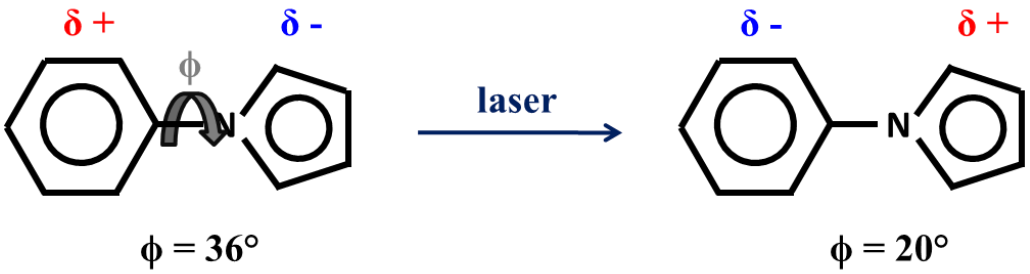

Also, the switch in partial charge (δ) localization following irradiation was measured and quantified. Molecular "switches" capable of charge reversal upon excitation are of increasing interest to materials chemists and engineers worldwide. Therefore, we have also investigated three benchmark aminobenzonitrile compounds in order to clarify the role of functional groups on laser-induced intramolecular charge transfer.

1.1 REFERENCES

1. G. D. Scholes, *J. Phys. Chem. Lett.*, **1**, 2 (2010).

2. P. F. Bernath, *Science*, **297**, 943 (2002).

3. J. H. Waite Jr., D. T. Young, T. E. Cravens, A. J. Coates, F. J. Crary, B. Magee, and J. Westlake, *Science*, 316, 870 (2007).

4. D. Zigmantas, E. L. Read, T. Mančal, T. Brixner, A. T. Gardiner, R. J. Cogdell, and G. R. Fleming, *Proc. Natl. Acad. Sci.*, **103**, 12672 (2006).

5. C. Fang, R. R. Frontiera, R. Tran, and R. A. Mathies, *Nature*, 462, 200 (2009).

6. A. J. Fleisher, P. J. Morgan, and D. W. Pratt, *J. Chem. Phys.*, **131**, 211101 (2009).

7. A. J. Fleisher, J. W. Young, D. W. Pratt, A. Cembran, and J. Gao, *J. Chem. Phys.* **134**, 114304 (2011).

8. D. Laage and J. T. Hynes, *Science*, **311**, 832 (2006).

9. J. A. Thomas, J. W. Young, A. J. Fleisher, L. Alvarez-Valtierra, and D. W. Pratt, *J. Phys. Chem. Lett.*, **1**, 2017 (2010).

2.0 INTERNAL AND EXTERNAL PERTURBATIONS IN ELECTRONIC SPECTROSCOPY. THE STARK SPECTRUM OF INDOLE-NH_3.

Adam J. Fleisher, Justin W. Young, and David W. Pratt

AJF and JWY performed the high resolution experiments. AJF performed the low resolution experiments, analyzed all experimental data, and performed theoretical calculations. AJF and DWP wrote the paper.

2.1 ABSTRACT

Hydrogen bond pairs involving the chromophore indole have been extensively studied in the gas phase. Here, we report rotationally resolved electronic spectroscopy experiments on the indole-NH_3 hydrogen bond pair in the absence and presence of an electric field. The S_1-S_0 origin band of this complex recorded at high resolution reveals two overlapping spectra; a consequence of NH_3 hindered internal rotation. The barrier to internal rotation is predicted by theory to be less than 20 cm^{-1} in the ground state, therefore requiring a non-rigid rotor Hamiltonian to interpret the spectra. Conducting the experiment in the presence of an applied electric field further perturbs the already congested spectrum, but allows for the permanent dipole moments of the complex to be measured. Efforts to interpret the unique perturbations that arise from both internal (molecular frame) and external (laboratory frame) sources are discussed.

2.2 INTRODUCTION

Indole, the chromophore of tryptophan, provides an excellent opportunity to probe the photophysics of larger biological systems in an isolated gas phase environment. Upon excitation with UV radiation, the electronic state ordering of indole is known to be highly sensitive to the surrounding environment. In the gas phase, the environment that surrounds indole can be carefully controlled, allowing for the systematic study of the solvent-dependent photophysics of this important biological chromophore. Numerous spectroscopic investigations of both polar and non-polar indole clusters afford a wealth of information on hydrogen bonding, van der Waals bonding, and solvation-controlled ^1L_a-^1L_b state coupling in indole and its derivatives.[1-10] At

significantly higher resolution, molecular beam measurements of indole and some select indole complexes have determined the lowest excited (S_1) state to be the ^1L_b state.[11-17] Recently, ^1L_a-^1L_b coupling in the bare molecule has been thoroughly explored using rotationally resolved data and a high level theoretical analysis.[18,19]

In this report, the hydrogen bond complexes formed between indole and ammonia were investigated with both low and high resolution fluorescence excitation spectroscopy in the gas phase. At low resolution, the indole-$(NH_3)_1$ (InA) and indole-$(NH_3)_2$ (InA_2) complexes were observed, along with intermolecular low frequency vibrations in the S_1 state. The identities of the intermolecular vibrations were assigned with the aid of theory and isotopic labeling experiments involving indole-*d* and ND_3. At high resolution, the InA complex was found to undergo tunneling between the equivalent minima of a potential energy surface with a low barrier to internal rotation. The assignment of rotational transitions accompanying electronic excitation has allowed for the structure of InA to be determined in both the ground (S_0) state and the excited S_1 state, including the hydrogen bond distances between indole and NH_3. Finally, the permanent electric dipole moments of InA indicate that ammonia induces a significant dipole on the indole host molecule, the magnitude of which is compared with analogous results on indole-(H_2O).[16]

2.3 METHODS

Indole-*h* was purchased from Alfa Aesar and used without further purification. Indole-*d* was synthesized by dissolving indole-*h* in methanol-*d* (purchased from Sigma-Aldrich) and stirring for 24 hours. The methanol-*d* was evaporated under vacuum using a hot water bath and the crystallized indole-*d* was collected, further dried on a vacuum line for 48 hours, and then stored

under Ar gas until used. Anhydrous ammonia (NH_3) was purchased from Matheson Tri-Gas, while ammonia-d_3 (ND_3) was purchased from Sigma-Aldrich.

The vibrationally resolved experiments were performed using a pulsed supersonic jet laser spectrometer.[20] The solid sample of indole-*h* (-*d*) was heated to ~ 50 °C inside a metal nozzle to create sufficient vapor pressure within a constant backing gas pressure of 2.8 ktorr consisting of He and NH_3 (ND_3). Ammonia is conservatively estimated to comprise < 3% of the total backing gas pressure. The stagnant sample gas was expanded through a 1 mm orifice into a vacuum chamber (pumped down to 10^{-5} torr) using a General Valve Series 9 pulsed valve operating at 10 Hz. The supersonic jet was crossed at a right angle 2 cm below the expansion with a pulsed UV laser beam, also operating at 10 Hz. The pulsed UV laser was created using a potassium dihydrogen phosphate (KD*P) crystal to frequency double the visible output of a dye laser (Quanta-Ray PDL-1) containing R6G laser dye purchased from Exciton. The dye laser was pumped with the second harmonic of a Nd^{+3}:YAG laser (Quanta-Ray DCR-1A). The total fluorescence excitation signal was collected by a photomultiplier tube (PMT) mounted perpendicular to both the supersonic jet and laser beam, processed by a boxcar integrator (Stanford Research Systems) and recorded digitally with Quick Data Acquisition software (Version 1.0.5).

The rotationally resolved experiments were performed with a molecular beam laser spectrometer.[21] In a quartz source, indole-*h* was heated to 110 °C and expanded through a 200 μm pinhole continuously at a constant backing pressure of 600 torr into the first of two differentially pumped vacuum chambers operating at 10^{-5} torr. The backing gas was an Ar:NH_3 mixture containing a 3% partial pressure of NH_3. The supersonic expansion was skimmed 2 cm downstream, and the resulting molecular beam was crossed at a right angle within the second

vacuum chamber (10^{-7} torr) by a continuous wave UV laser 13 cm downstream from the 1 mm diameter skimmer. The UV laser, with a bandwidth of < 1 MHz, was created using a Wavetrain external frequency doubling cavity (Spectra-Physics) containing a β-barium borate (BBO) crystal (Fujian Castech). The fundamental visible radiation was created using a modified scanning ring dye laser (Spectra-Physics 380D frequency stabilized RDL), an R6G laser dye jet, and the 514.5 nm line of an argon ion pump laser (Spectra-Physics 171 ion laser, Spectra-Physics 270 power supply). The total fluorescence excitation signal was collected by spherical optics mounted above and below the point of beam intersection, and focused into a PMT (EMI 9813 QB) mounted perpendicular to both beams. The absorption spectrum of I_2 was simultaneously recorded and used for absolute frequency calibration, while the frequency markers of a temperature-stabilized etalon (FSR = 299.7520 MHz in the visible) were recorded for relative frequency calibration. Stark optics, containing wire mesh grids above and below the point of beam intersection, were used to measure permanent electric dipole moments *via* the application of a static electric field.[22] The high resolution spectra, I_2 absorption spectra, and frequency markers were recorded using JBA95 acquisition software[23] and analyzed using JB95 software.[24]

Ground electronic state calculations were performed using GAUSSIAN 03[25] at the Center for Simulation and Modeling at the University of Pittsburgh. In the ground state, InA was optimized at both the M05-2X and MP2 levels of theory. Various correlation-consistent Dunning basis sets[26] were used for these optimizations, ranging from cc-pVDZ to aug-cc-pVQZ in the DFT optimizations, and up to aug-cc-pVTZ for the *ab initio* optimizations. The vibrational frequencies were calculated following each optimization, and no imaginary frequencies were found. Ground state M05-2X optimizations and frequency calculations were also performed on InA_2 clusters using several Dunning basis sets.

The NH_3 torsional potential energy surface of InA was explored by stepping the torsional angle α in 15° increments over the range 0 to 360°. These relaxed scans were performed with the following theory/basis set combinations: M05-2X/cc-pVDZ, M05-2X/6-31+G*, M05-2X/aug-cc-pVDZ, and MP2/cc-pVDZ. The data points obtained from the relaxed scans were then fit to an expansion of torsional functions. We find that a smooth one-dimensional surface is produced by truncating the expansion of torsional functions after the first term, the three-fold barrier (V_3) term.

2.4 RESULTS

2.4.1 Fluorescence excitation spectra

The low resolution fluorescence excitation spectrum (FES) of InA is shown at the top of Fig. 2-1. The excitation spectrum was recorded at frequencies to the red of the indole-*h* electronic origin, and closely resembles the FES previously reported by Hager *et al.*[2] The electronic origin of indole occurs at a frequency of 35231.4 cm^{-1}; the InA origin is shifted to the red by 218.8 cm^{-1}, and the InA_2 origin is shifted further to the red by a total of 364.0 cm^{-1}. A small amount of water was also present during the experiment, as the indole-$(H_2O)_1$ (InW) complex was also observed at 35099.6 cm^{-1}, exhibiting a smaller red shift of 131.8 cm^{-1}. The four transitions, labled "In", "InA", "InA_2", and "InW" in the top of Fig. 2-1 are the most intense transitions observed in this frequency region. Other weaker bands appear on the blue side of several of these transitions.

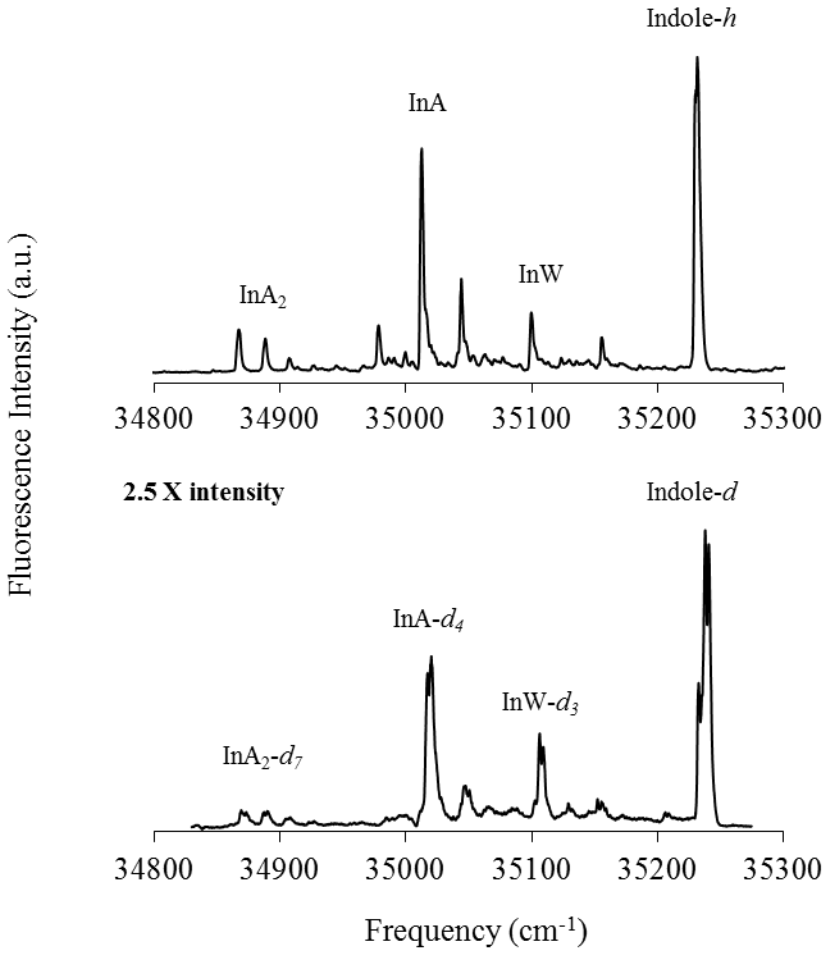

Figure 2-1. Low resolution fluorescence excitation spectrum (FES) of indole-*h*-NH_3 (InA, top) and indole-*d*-NH_3 (InA-d_4, bottom).

The low resolution FES of indole-*d* in the presence of ND_3 is shown at the bottom of Fig. 2-1. The indole-*d* origin is shifted 6.6 cm^{-1} to the blue of the less intense indole-*h*. Clearly, some indole-*h* remains in the deuterated sample, as the indole-*h* electronic origin appears as a shoulder to the red of the more intense indole-*d* origin. Broadened transitions appear for InA-d_4, InW-d_3 and InA_2-d_7, possibly due to hydrogen contamination which greatly increases the number of incompletely deuterated species present in the jet expansion. The perceived broadening at low resolution also could indicate a larger torsional splitting for the deuterated transitions as compared to those of the normal hydrogen species. The InA-d_4, InW-d_3, and InA_2-d_7 electronic origins are also all blue-shifted relative to the non-deuterated transition energies.

Table 2-1 lists the experimentally observed vibrational frequencies and approximate isotope shifts of the origin bands and a few of the low frequency bands that were observed upon indole-*d* and ND_3 deuteration, along with normal mode assignments. Varying isotopic shift ratios of ν_d/ν_h are observed, all of which are less than unity,[27] confirming their assignment as intermolecular vibrations involving the NH_3/ND_3 hydrogen bonding partners of indole.

The high resolution FES of the InA origin is shown in Fig. 2-2. The recorded spectrum spans almost 3.4 cm^{-1}, and is rich with rotationally resolved transitions that accompany electronic excitation. As will be seen, the congestion in this spectrum is caused by the presence of two superimposed rovibronic bands, produced by a hindered internal rotation of the attached NH_3.[28,29] The existence of a three-fold internal rotor splits the electronic spectrum into two subtorsional bands, labeled the *A* and *E* subbands by symmetry (irreducible representations of the C_3 point group), analogous to the distinct torsional levels observed in the rotational spectroscopy of molecules containing methyl rotors.[30-32] Thus, our analysis of this spectrum proceeded in two distinct steps.

Table 2-1. Measured and assigned S_1 origin bands and intermolecular vibrational modes of InA and InA_2.

Complex	ν_h (cm^{-1})	ν_d (cm^{-1})	ν_d / ν_h	Assignment
InA	35012.6	35018.7		origin
	+31.4	+28.4	0.90	$\nu_{b'}$ bend
	+143.0	+133.5	0.93	ν_s stretch
InA_2	34867.4	34871.3		origin
	+21.0	+17.5	0.83	ν_1 coupled stretch
	+39.2	+36.1	0.92	$2\nu_1$

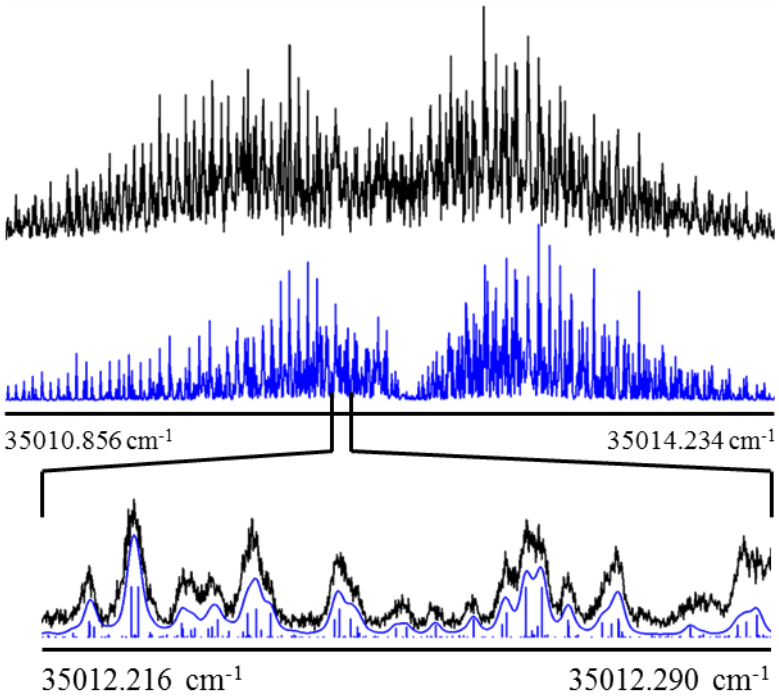

Figure 2-2. High resolution FES of the S_1-S_0 origin band of InA (black). The simulated spectrum (blue) reproduces the experimental trace at full rotational resolution, as shown in the bottom panel.

The first step in the analysis was to fit the individual rotational transitions of the *A* subband (shifted to the blue of the *E* subband by ~ 0.33 cm^{-1}) using a rigid rotor Hamiltonian for each electronic state and a least squares fitting method. In all, 399 assignments were made, yielding an overall observed-minus-calculated (OMC) value of 3.4 MHz. The rotational constants and fitting parameters used in the *A* subband simulation are listed in Table 2-2. The rigid rotor Hamiltonian was sufficient to assign transitions with values of $J < 25$. For transitions involving higher *J* values, the OMC of the fit was improved by including Watson's distortion terms (A-reduction)[33] to the Hamiltonians, and these parameters are also listed in Table 2-2. However, the rigid-rotor rotational constants were not altered by more than two standard deviations by this procedure, and therefore are used for analysis and interpretation throughout the remainder of this work.

The second step in the analysis was to fit the individual rotational transitions of the *E* subband using a non-rigid rotor Hamiltonian. This Hamiltonian consists of three components: ammonia torsion $\hat{H}_t$, overall rotation $\hat{H}_r$, and torsion-rotation coupling $\hat{H}_{tr}$. In the case of the *E* subband, the first-order contributions from $\hat{H}_{tr}$ are non-zero, and the appropriate total Hamiltonian in the high-barrier limit is:[30]

Equation 2-1

$$\hat{H} = A_{\text{eff}}\hat{P}_a^2 + B_{\text{eff}}\hat{P}_b^2 + C_{\text{eff}}\hat{P}_c^2 + D_a\hat{P}_a + D_b\hat{P}_b$$

Equation 2-2

$$A_{\text{eff}} = A + W_{v\sigma}^{(2)}\hat{\rho}_a^2, \textit{ etc.}$$

Table 2-2. Experimentally determined rotational constants and fitting parameters of the indole-$(NH_3)_1$ *A* band.

State	Parameter	Rigid Asymmetric Rotor	Distortable Asymmetric Rotor
S_0	*A* (MHz)	2095.75(10)	2095.90(10)
	B (MHz)	947.30(10)	947.49(10)
	C (MHz)	652.18(10)	652.20(10)
	ΔI (uÅ^2)	+0.27(13)	+0.36(13)
	κ	-0.59112(15)	-0.59093(15)
	Δ_J (kHz)		0.53(6)
	Δ_{JK} (kHz)		-3.2(3)
	Δ_K (kHz)		5.8(4)
	δ_J (kHz)		0.14(3)
	δ_K (kHz)		4.6(4)
S_1	*A* (MHz)	2000.55(10)	2000.63(10)
	B (MHz)	977.89(10)	978.06(10)
	C (MHz)	656.78(10)	656.81(10)
	ΔI (uÅ^2)	+0.04(12)	+0.11(12)
	κ	-0.52208(15)	-0.52189(15)
	Δ_J (kHz)		0.049(6)
	Δ_{JK} (kHz)		-3.2(2)
	Δ_K (kHz)		5.0(3)
	δ_J (kHz)		0.14(3)
	δ_K (kHz)		3.1(3)
	Origin (cm^{-1})	35012.626(1)	35012.626(1)
	Linewidth L/G (MHz)	25/25 ± 2	25/25 ± 2
	T_{rot} (K)	5 ± 1	5 ± 1
	Transition Moment *a*/*b*/*c* (%)	0/100/0 ± 5	0/100/0 ± 5
	Assigned Lines	399	399
	OMC	3.4	2.3

Equation 2-3

$$D_a = FW_{\nu\sigma}^{(1)}\rho_a, \textit{ etc.}$$

An approximate simulation of the *E* subband using this Hamiltonian yields very large perturbation terms D_a and D_b in each electronic state. We estimate $D_a \approx 3800 \pm 300$ cm^{-1} and $D_b \approx 900 \pm 100$ cm^{-1} in both electronic states, which translate into extremely low barrier heights of approximately 4-6 cm^{-1}. Transitions within the *E* subband with quantum numbers $J \approx K_a$ and low *J* values appear the most perturbed, and therefore were the focus of the fitting process to this point.

Without accurate values of D_a and D_b, other data were used to determine the perturbative contributions of internal rotation to the rotational energy levels. As noted above, the first-order contributions to the *A* subband rotational constants are zero. However, second-order contributions remain, which lead to the effective rigid-rotor rotational constants shown in Eq. 2-2. Collectively, the *A*, *B*, and *C* constants in the rigid-rotor column of Table 2-2 result in positive inertial defect values of $\Delta I'' = 0.27$ and $\Delta I' = 0.04$ uÅ^2. A static InA structure in which no internal rotation of the NH_3 molecule occurs would have an inertial defect value of $\Delta I_{stat} \approx -2.67$ uÅ^2 (see Section 2.4.2), quite different from the values observed experimentally. If vibrational contributions to ΔI are neglected, the difference between the experimental and theoretical ΔIs can be attributed to the second-order perturbation coefficents shown in Eq. 2-2.[34,35] By requiring $\Delta I_{stat} = \Delta I_{exp}$, it is possible to solve for the second-order $W^{(2)}$ coefficients, which are related to the barrier heights in each electronic state *via* Herschbach's equations.[31,36] This analysis yields upper-limits to the barrier heights, with values of $V_3'' = 44$ and $V_3' = 48$ cm^{-1}, respectively (see Appendix A).

The rotational constants reported for InA are different from those found for bare indole.[11-13,37] While internal rotation clearly contributes, the overwhelming reason for this difference is the attachment of NH_3 to the indole frame *via* a hydrogen bond. We can use the measured differences in rotational constants to determine the NH_3 position and hydrogen bond structure using Kraitchman's equations.[38,39] In this analysis, the *A* subband constants of InA were used as an estimate of the rigid body rotational constants. The substitution coordinates (r_s) were calculated by treating NH_3 as a point mass of 17 atomic mass units (u). Within the InA inertial frame (substitute, *s*), the NH_3 coordinates are measured to be x''_s = 3.9869(6) and y''_s = -1.1465(3) Å in S_0, and x'_s = 3.8937(6) and y'_s = -1.1665(4) Å in S_1. The NH_3 coordinates within the indole-*h* inertial frame (parent, *p*) are listed in Table 2-3.

The substitution coordinates of the indole amino hydrogen are known from previous rotationally resolved experiments performed on isotopically labeled compounds,[13,37] and are also listed in Table 2-3. Through an extension of Kraitchman's equations,[39] a transformation matrix and translation vector were written to express the known indole-*h* coordinates in the InA inertial frame. From there, the hydrogen bond length (r_{NH-H}) can be estimated in each electronic state as the distance between the indole-*h* atom and the NH_3 point mass. Also, the hydrogen bond angle with respect to the *a* inertial axis of InA (θ_r) can be calculated from this data. These hydrogen bond parameters are listed in the final column of Table 2-3, and will be directly compared to calculated properties from DFT and *ab initio* geometry optimizations in later discussion.

High resolution Stark spectra of the InA electronic origin band were recorded in the presence of several applied electric fields ranging from 200 to 1700 V/cm; see Fig. 2-3. When an electric field is applied, the rotational energy levels of the InA complex are perturbed. As a result, rotational energy levels shift and split, as the $2J + 1$ degeneracy in M_J levels is removed

Table 2-3. Substitution coordinates (r_s) (Ref. 38) of the indole amino hydrogen atom and the InA ammonia molecule treated as a point mass in the indole-*h* inertial frame.

State	Parameter	In-*h*	In-NH_3	Hydrogen bond[c]
S_0	x''_p (Å)	1.8638(7)[a]	2.3927(7)	
	y''_p (Å)	2.0232(7)[a]	4.110(2)	
	$r''_{NH\text{-}N}$ (Å)			2.153(1)
	θ''_r (deg)			32.041(7)
S_1	x'_p (Å)	1.861(6)[b]	2.1511(7)	
	y'_p (Å)	2.095(1)[b]	4.131(2)	
	$r'_{NH\text{-}N}$ (Å)			2.036(3)
	θ'_r (deg)			35.99(7)

[a]From Ref. 37.
[b]From Ref. 13.
[c]InA inertial frame (Ref. 39).

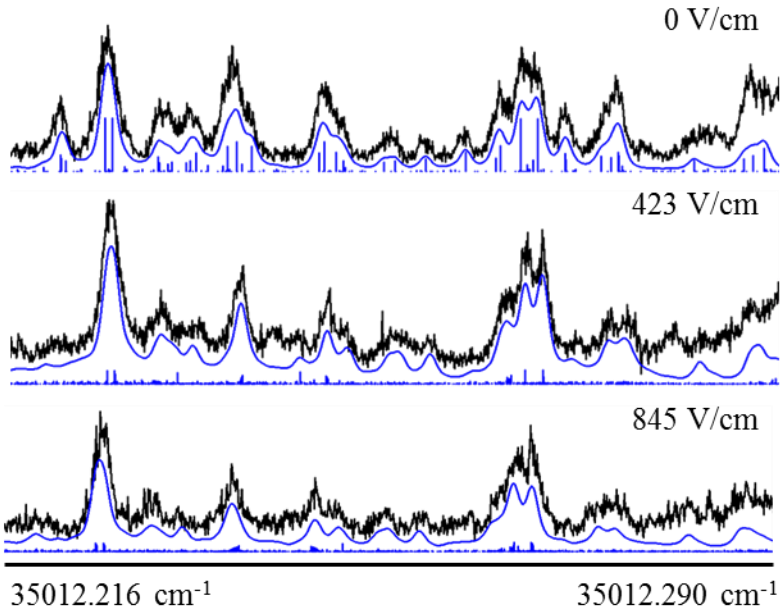

Figure 2-3. High resolution Stark spectra of the InA S_1-S_0 origin band recorded at several applied electric fields. The permanent EDMs of InA in S_0 and S_1 were used to simulate (blue) and fit the experimental (black) spectra.

by the field.[22,30] The electric field dependent rotational energy level shifts are related to the permanent electric dipole moments (EDMs) of InA *via* the Stark Hamiltonian, which was added as a perturbation to the asymmetric rigid rotor Hamiltonian in the analysis of the Stark spectra.[22,40]

A simulation of the Stark spectrum recorded at an applied electric field of 423 V/cm was fit by least squares using 48 transitions observed in the experimental spectrum. This fit produced the following EDM projections onto the inertial axes of InA: μ_a = 4.69(3) and μ_b = 1.1(2) D in S_0, and μ_a = 4.53(3) and μ_b = 1.1(4) D in S_1. No contributions from μ_c were detected, as expected for symmetry reasons. The experimentally measured total EDMs are 4.8(1) D in S_0 and 4.7(2) D in S_1. The EDMs measured using the 423 V/cm Stark spectrum reproduce the remaining Stark spectra well, as shown in the various panels of Fig. 2-3.

2.4.2 Theoretical structures and vibrational frequencies

Ground state structures of InA and InA_2 were optimized using DFT and *ab initio* methods. Tables 2-4 and 2-5 list the ground state rotational constants, hydrogen bond lengths, NH_3 C_3 symmetry axis angles, and the four lowest frequency vibrations calculated for the two complexes. Beginning with the M05-2X data in Table 2-4, the double-ζ basis sets appear inadequate at predicting a reliable structure, as their rotational constants differ significantly from those predicted using larger basis sets. However, the hydrogen bond length $r_{NH\text{-}N}$ is basis-set independent beyond cc-pVDZ, indicating that the differences observed in the calculated rotational constants beyond this point pertain to the indole ring. In the aug-cc-pVDZ optimization, the largest θ_r angle made by the C_3 symmetry axis of NH_3 relative to the *a* inertial axis of the complex is calculated to be 36°. This "outlier" value of θ_r relative to the other basis

Table 2-4. Theoretical rotational constants, hydrogen bond lengths, ammonia C_3 symmetry axis angles, and low frequency vibrations of InA. An asterisk (*) indicates that no vibrational frequencies were calculated. The vibrational frequencies are not scaled.

	M05-2X						MP2			
Parameter	cc-pVDZ	cc-pVTZ	cc-pVQZ	aug-cc-pVDZ	aug-cc-pVTZ	aug-cc-pVQZ	cc-pVDZ	cc-pVTZ	aug-cc-pVDZ	aug-cc-pVTZ
A (MHz)	2045.9	2061.7	2088.5	2008.1	2083.4	2083.8	2068.6	2096.7	2020.5	2092.1
B (MHz)	978.5	965.1	950.8	977.0	953.1	952.2	958.5	962.4	967.3	959.6
C (MHz)	664.2	659.7	655.6	659.2	656.2	655.8	657.2	661.9	656.4	660.2
ΔI (uÅ^2)	-2.66	-2.67	-2.67	-2.68	-2.67	-2.67	-2.66	-2.65	-2.69	-2.67
$r_{NH\text{-}N}$ (Å)	1.99	2.07	2.08	2.07	2.07	2.08	1.94	1.97	1.98	1.99
θ_r (deg)	34	33	31	36	32	32	33	32	35	32
$\nu_{b'}$ (cm^{-1})	32.6	24.8	27.2	23.4	26.1	26.7	9.6	24.7	29.2	*
$\nu_{b''}$ (cm^{-1})	33.9	25.2	28.6	41.1	30.1	28.8	38.3	34.6	31.3	*
ν_τ (cm^{-1})	54.3	47.7	33.8	50.7	42.1	37.3	42.6	40.0	45.9	*
ν_s (cm^{-1})	166.3	144.1	142.2	141.7	142.2	140.8	173.0	160.4	155.8	*

Table 2-5. Theoretical rotational constants and low frequency vibrations of InA_2. An asterisk (*) indicates that no vibrational frequencies were calculated. The vibrational frequencies are not scaled.

				M05-2X			MP2
Parameter	cc-pVDZ	cc-pVTZ	cc-pVQZ	aug-cc-pVDZ	aug-cc-pVTZ	aug-cc-pVQZ	cc-pVDZ
A (MHz)	1403.7	1394.9	1397.5	1368.1	1380.5	1381.3	1404.7
B (MHz)	826.9	822.4	822.4	835.8	830.7	830.9	817.6
C (MHz)	668.1	668.7	670.7	671.5	672.9	673.1	663.4
ΔI (uÅ^2)	-214.8	-221.1	-222.7	-221.5	-223.5	-223.3	-216.1
ν_1 (cm^{-1})	29.6	31.2	31.2	29.8	29.3	*	26.8
ν_2 (cm^{-1})	37.2	36.9	35.6	34.5	34.8	*	39.6
ν_3 (cm^{-1})	51.2	48.0	46.2	46.1	46.3	*	51.8
ν_4 (cm^{-1})	100.4	109.2	104.4	78.9	95.7	*	120.9

sets used in Table 2-4 may explain the drastically different rotational constants predicted by the M05-2X/aug-cc-pVDZ combination. Taking the M05-2X/aug-cc-pVQZ optimization to be the most accurate of the DFT calculations, the theoretical hydrogen bond length is 2.07 Å in S_0, and the NH_3 symmetry axis makes an angle of 32° with the *a*-axis of InA. The MP2 data in Table 2-4 are less complete; however, it again appears that a triple-ζ basis set is required to predict a reliable geometry. Comparatively, using the aug-cc-pVTZ basis set, identical θ_r angles are predicted by both DFT and *ab initio* methods; however, the MP2 optimization predicts a smaller hydrogen bond distance of $r_{NH\text{-}N}$ = 1.99 Å.

Each structure listed in Table 2-4 has a similar inertial defect of $\Delta I \approx$ -2.67 uÅ^2. The inertial defect is a very sensitive measure of the out-of-plane distribution of mass within a molecule or complex. For example, the ΔI of indole is nearly zero in each electronic state; with values of -0.112 in S_0 and +0.168 in S_1.[12,37] In the case of InA, all heavy atoms are contained in the *ab* inertial plane. The optimized structures indicate that two hydrogen atoms belonging to the ammonia molecule are out of the *ab* plane. These two hydrogen atoms are responsible for the non-zero inertial defects calculated in Table 2-4. In Table 2-5, $\Delta I \approx$ -223 uÅ^2 for InA_2, a nearly 100-fold increase in magnitude as compared to InA. In the double ammonia cluster, one NH_3 molecule sits above the indole molecule, and the hydrogen bonding network pulls the first NH_3 bound to the amino hydrogen up and out of the indole plane entirely. This $(NH_3)_2$ arrangement is similar in structure to that found in the $(NH_3)_2$ dimer, as measured in great detail using far-infrared and microwave spectroscopy.[41-43] Examples of the optimized structures of InA and InA_2 are shown in Fig. 2-4.

Next, the S_0 vibrational frequencies listed in Tables 2-4 and 2-5 were used to estimate the S_1 vibrational frequencies responsible for several transitions observed in Fig. 2-1; see also Table

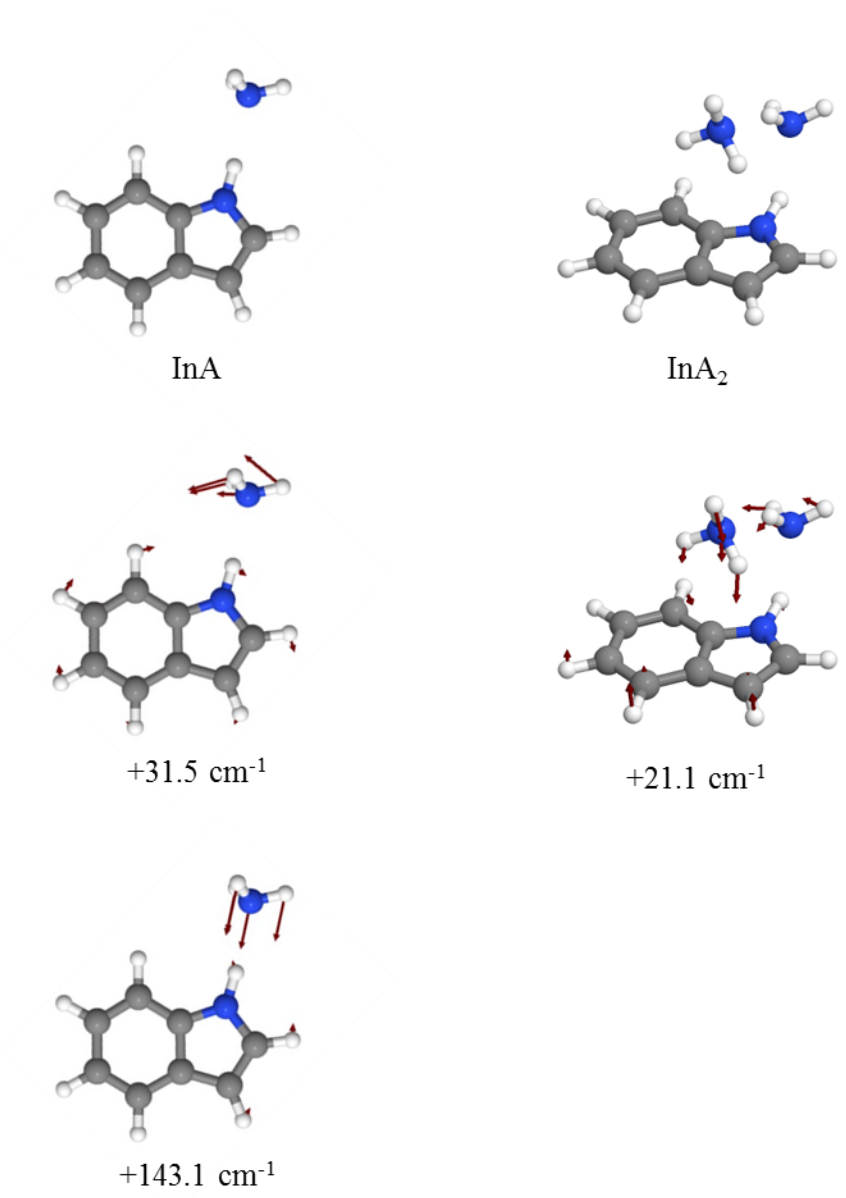

Figure 2-4. DFT structures (M05-2X/aug-cc-pVxZ) and assigned vibrational modes of InA (x = Q) and InA_2 (x = T).

2-1. The two lowest frequency theoretical vibrations are both intermolecular hydrogen bond bends, labeled $\nu_{b'}$ and $\nu_{b''}$. Although there were no symmetry restrictions imposed on the calculations, the structure of InA effectively belongs to the C_s point group. Therefore, we classify the in-plane bending mode as $\nu_{b'}$ (A' irreducible representation) and the out-of-plane bending mode as $\nu_{b''}$ (A'' irreducible representation). The remaining two low frequency vibrations are also intermolecular in nature. We label the ammonia torsional mode ν_τ and the hydrogen bond stretching mode ν_s.

Two of the InA intermolecular modes were detected in the low resolution FES (Fig. 2-1). At an absolute frequency of 35044.0 cm^{-1}, we assign the intermolecular bending mode $\nu_{b'}$ to have a frequency shift relative to the InA origin of +31.4 cm^{-1} (*cf.* Fig. 2-4). We see no evidence for the excitation of the torsional mode ν_τ in S_1. We can, however, assign the stretching mode ν_s to a relative frequency of +143.0 cm^{-1} (35155.6 cm^{-1}). A single progression appears in the low resolution FES of the InA_2 cluster. We assign the +21.0 cm^{-1} (34888.4 cm^{-1}) mode as the coupled NH_3-NH_3 hydrogen bond stretching and second NH_3 π-hydrogen bond stretching mode ν_1 (*cf.* Fig. 2-4). Two quanta of the coupled stretching mode appear as the +39.2 transition (34906.6 cm^{-1}). Alternatively, the +39.2 transition could be a coupled rocking mode (either ν_2 or ν_3). However, we believe a Franck-Condon progression in ν_1 is the most likely. The torsion of the π-hydrogen bound NH_3 molecule appears at a higher frequency, and is labeled ν_4.

2.4.3 Theoretical barrier heights to internal rotation

As detected by measuring the high resolution FES of InA, the NH_3 molecule undergoes hindered internal rotation about its C_3 axis (*i.e.*; the hydrogen bond). Tunneling between the three equivalent minima along this coordinate results in the splitting observed at high resolution. In

order to investigate the potential energy surface (PES) governing this motion, we have calculated the relaxed geometries of InA by stepping the torsional angle α in 15° increments from 0 to 360° using either M05-2X or MP2 theory. The basis sets employed for these calculations are cc-pVDZ for both M05-2X and MP2, as well as 6-31+G* and aug-cc-pVDZ for M05-2X DFT. The four relaxed PES scans provided the relative energies of 25 points spaced evenly along the α coordinate. Each set of data points was fit to the torsional PES function

Equation 2-4

$$V(\alpha) = \frac{V_3}{2}(1 - \cos 3\alpha),$$

where V_3 is the barrier height to NH_3 internal rotation. The PESs are plotted in Fig. 2-5 with the following theoretical V_3 barrier heights: MP2/cc-pVDZ = 10.5, M05-2X/cc-pVDZ = 12.2, M05-2X/6-31+G* = 16.4, and M05-2X/aug-cc-pVDZ = 26.0 cm^{-1}, respectively. The standard errors between each PES curve and the calculated relaxed scan energy points are small: 0.8, 0.4, 0.5, and 1.3 cm^{-1}, respectively. The theoretical values are in good agreement with the upper-bound ground state V_3'' experimental value of 44 cm^{-1}.

2.5 DISCUSSION

2.5.1 Structure of InA in its S_0 and S_1 electronic states

Indole, the chromophore of tryptophan, has two low-lying π-π* singlet excited electronic states known as the ^1L_b and ^1L_a states.[44] The ^1L_a-^1L_b energy gap is ~ 2000 cm^{-1} in the gas phase, with

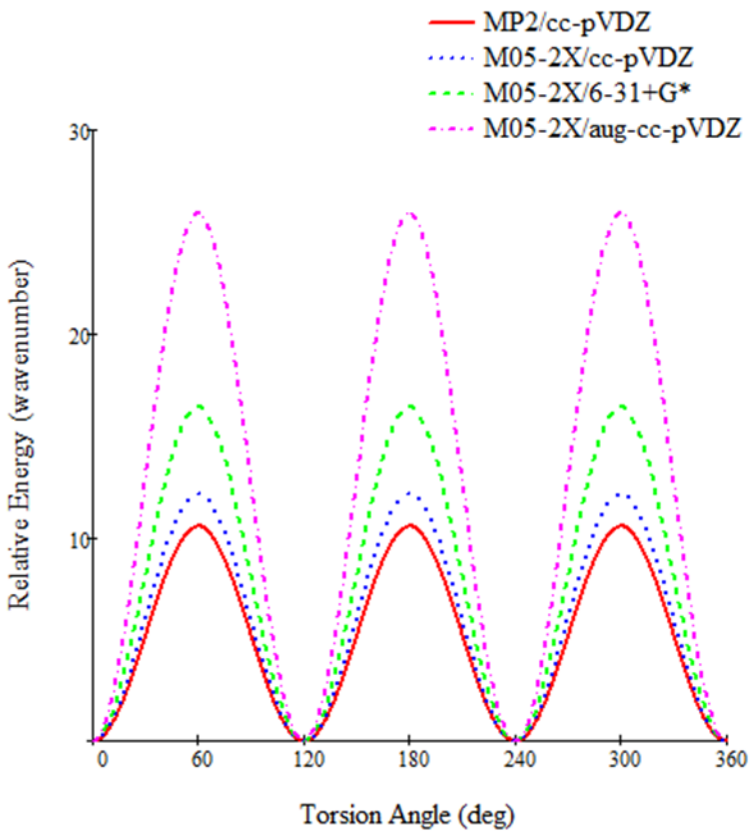

Figure 2-5. Predicted torsional potential energy surfaces for NH_3 internal rotation about the hydrogen bond in the S_0 state of InA.

the ^1L_b state lying lower in energy.[18,19] This energy gap is extremely sensitive to solvent polarity in the condensed phase, a finding that has motivated many studies of the gas phase photophysics of indole-solvent clusters.[45] The high resolution FES of the indole-H_2O (InW) electronic origin determined that S_1 is indeed the ^1L_b state,[14] as was the case for bare indole. The electronic transition moment of InW lies almost entirely along the *b* inertial axis of the complex, identical to our findings here for InA. Therefore, we also assign the S_1 state of InA as the ^1L_b state. No evidence for solvent-induced ^1L_a-^1L_b state mixing was found in the electronic origin band of InA.

Using the measured S_0 and S_1 *A* band rotational constants of InA, we have estimated the hydrogen bond parameters in each electronic state through the calculation of r_s coordinates. The intermolecular hydrogen bond is linear, between the amino hydrogen on indole and the nitrogen of ammonia, along the C_3 symmetry axis of NH_3. In the ground state, the hydrogen bond distance is $r''_{NH\text{-}N}$ = 2.15 Å, and makes an angle with respect to the *a* inertial axis of θ_r = 32°. Comparing these parameters to the theoretical parameters listed in Table 2-4, we see that DFT reproduces the experimental estimates quite well, while being computationally less expensive than the *ab initio* method. The *ab initio* calculations underestimate the hydrogen bond length by 0.1-0.2 Å in S_0. Upon excitation to S_1, we measure a decrease in the hydrogen bond length of $\Delta r_{NH\text{-}N}$ = 0.11 Å to an excited state value of $r'_{NH\text{-}N}$ = 2.04 Å. This hydrogen bond length reduction of ~ 0.1 Å was also observed in the InW complex.[14,46]

It must be noted that the theoretically calculated rotational constants and hydrogen bond parameters are characteristic of fundamentally different structures than those parameters determined experimentally. Theory calculates the equilibrium structure and atomic coordinates (r_e), whereas the experimentally determined rotational constants are those of the vibrationally averaged atomic coordinates (r_0) and structure. Additionally, the *A* subband rotational constants

contain a contribution from internal rotation, a topic that has already been addressed. Also, we report here substitution coordinates (r_s) for the indole-*h* and indole-NH_3 positions, which neglect differences in zero-point vibration between the parent and substitute isotopomers.[38] While these differences between experiment and theory exist, the synergy between the two is still apparent; the experimentally derived and theoretically calculated geometries of InA are in overall excellent agreement.

2.5.2 Internal rotation dynamics in InA

The observation of a splitting in the electronic origin of InA confirms the existence of NH_3 tunneling through a barrier to internal rotation. An estimate of the origin frequency of the *E* subband was derived from the high resolution FES to be ~ 35012.3 cm^{-1}. The *E*-*A* subband origin frequency difference is therefore small, only ~ 9900 MHz (0.33 cm^{-1}), meaning that the change in barrier height upon electronic excitation must also be small. The *E* subband origin is red-shifted from the *A* subband origin. Therefore, the barrier height in S_1 must be slightly larger than that found in S_0 (*i.e.;* $V'_3 > V''_3$), in accord with the finding that the intermolecular hydrogen bond is shorter in the S_1 state than in the S_0 state.

Theory predicts that a low barrier to internal rotation exists in S_0; the estimated V_3 barrier heights range from 10-26 cm^{-1}. A second estimate of this barrier comes from the measured inertial defects. While we have no measure of the "static" rotational constants, theory does show that a static InA structure would contain only two out-of-plane atoms; two of the hydrogen atoms on NH_3. The inertial defect of this static structure would be $\Delta I_{stat} \approx$ -2.67 u$Å^2$, significantly different from the measured values for the *A* subband found in Table 2-2. This large difference between $\Delta I_{stat} \approx$ -2.67, $\Delta I'' =$ +0.27, and $\Delta I' =$ +0.04 u$Å^2$ confirms that the barrier heights to

internal rotation are low in each electronic state. In the microwave spectrum of pyrrole-NH_3, a similarly large and positive ΔI = +0.5 was reported. In that case, the barrier height to internal rotation was predicted to be extremely low, measuring only 1.2 cal/mol (0.24 cm^{-1}).[47]

2.5.3 Dipole moments of InA in its S_0 and S_1 electronic states.

Finally, we discuss the charge distributions in the two electronic states of InA, as revealed by their measured permanent EDMs. Table 2-6 lists these values, along with the known values for indole and InW for comparison. In both S_0 and S_1, the total dipole moment of InA is the largest, larger even than the dipoles measured for InW. Initially, this was surprising, as the dipole moment of H_2O (1.85 D) is larger than that of NH_3 (1.42 D). The larger value of the EDM in ground state InA may be traced to the mutual orientations of the dipoles of the component parts, which in InA are nearly aligned. Upon excitation, the EDMs are observed to decrease in magnitude in bare indole and in both of the indole complexes, which is another surprising result. While the decrease in InW is quite large (-0.4 D), the decrease is smaller in indole (-0.10 D) and InA (-0.1 D). The larger decrease in InW is associated with solvent reorganization,[14,16] which changes the orientation of the water dipole relative to indole. Additionally, the large amplitude dynamics of water that comprise the internal rotation creates a non-uniform time-varying electric field.[48] These large solvent rearrangements do not occur in InA, as the hydrogen bond remains linear upon excitation and throughout NH_3 internal rotation about its symmetry axis.

The remaining differences between the EDMs of InA and InW arise from more subtle effects. Previously, it was shown using an electrostatic model[16] that the InW dipole in each electronic state could be reproduced by a sum of three terms; the EDM of indole (μ_{indole}), the EDM of water ($\mu_{\mathrm{H_2O}}$), and the indole polarization EDM induced by the dipole and quadrupole

Table 2-6. Permanent EDMs of indole, indole-H_2O, and indole-NH_3 in the gas phase.

State	Parameter	Indole[a]	In-H_2O[b]	In-NH_3
S_0	μ''_a (D)	1.376(8)	4.20(6)	4.69(3)
	μ''_b (D)	1.40(1)	1.2(3)	1.1(2)
	μ'' (D)	1.96(1)	4.4(3)	4.8(1)
S_1	μ''_a (D)	1.556(8)	3.90(6)	4.53(3)
	μ''_b (D)	1.01(1)	0.9(3)	1.1(4)
	μ'' (D)	1.86(1)	4.0(3)	4.7(2)
	$\Delta\mu$ (D)	-0.10(1)	-0.4(4)	-0.1(2)

[a]S_0 EDMs from Ref. 37, S_1 EDMs from Ref. 16.

[b]EDMs from Ref. 16.

[c]This work.

moments of water (μ_{ind}). In addition, we anticipate a possible contribution from charge transfer (μ_{CT}), as was observed in the case of β-naphthol-NH_3,[48,49] and write:

Equation 2-5

$$\mu_{\text{total}} = \mu_{\text{indole}} + \mu_{\text{solvent}} + \mu_{\text{ind}} + \mu_{\text{CT}}$$

In the case of InW, $\mu_{\text{CT}} = 0$ D, as mentioned above. However, in the case of InA, a charge transfer contribution may be required, as shown in Figure 2-6. We explain this fundamental difference between the H_2O and NH_3 indole complexes as follows; the internal motion of H_2O significantly modulates the electric field felt by the host indole molecule, even more so than in the case of β-naphthol-H_2O (2HNW).[48] Therefore, the hydrogen bond found in the InA complex is significantly stronger and, importantly, unchanged in an electronic sense by internal rotation. Additionally, ammonia is a much stronger base than water. We therefore hypothesize that some CT exists in the InA complex, which additionally accounts for the larger red shift found in the electronic spectrum of indole in the presence of NH_3. Further support for such a hypothesis is being explored using electrostatic[49] and DFT decomposition[48] techniques.

2.6 SUMMARY

Reported here are the rotationally resolved fluorescence excitation spectra of the S_1-S_0 electronic origin band of the single ammonia complex of indole, InA, and its deuterated analog. The first excited state of InA is a ^1L_b state, identical to the corresponding states in bare indole and the InW

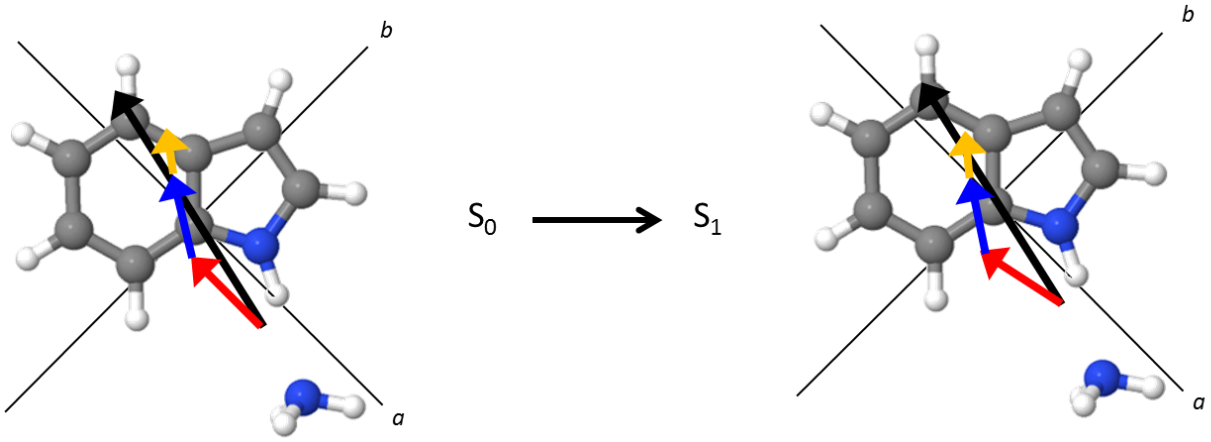

Figure 2-6. Illustration of the dipole decomposition of InA (black dipole). The dipoles of indole (red), NH_3 (blue), and the induced dipole (orange) are shown above. The induced dipole measurements are preliminary, as ground and excited state calculations of the indole polarizability are still under investigation.

complex. The indole-NH_3 hydrogen bond is measured to be 2.15 Å in the ground state, and decrease upon excitation by 0.1 Å. Also, we report the qualitative finding that the barrier height to NH_3 internal rotation is larger in S_1 than in S_0, thus confirming the increase in hydrogen bond strength upon excitation with UV light. The permanent electric dipole moments of the complex were measured, and indicate the existence of a substantial induced dipole upon complex formation, and possibly the existence of charge transfer between the hydrogen bond donor and acceptor. A thorough theoretical investigation of the ground state structure and internal rotation potential energy surface corroborate the experimental findings, and indicate that, at a minimum, a triple-ζ basis set is required for the investigation of hydrogen bond geometries.

2.7 ACKNOWLEDGEMENTS

This work has been supported by the Andrew Mellon Predoctoral Fellowship and the U.S. National Science Foundation (CHE-0911117), to whom we are grateful. We also acknowledge the help of Patrick Walsh during the low resolution experiments.

2.8 REFERENCES

1. J. Hager and S. C. Wallace, *J. Phys. Chem.* **87**, 2121 (1983).

2. J. Hager and S. C. Wallace, *J. Phys. Chem.* **88**, 5513 (1984).

3. J. Hager, M. Ivanco, M. A. Smith, and S. C. Wallace, *Chem. Phys. Lett.* **113**, 503 (1985).

4. J. Hager and S. C. Wallace, *Can. J. Chem.* **63**, 1502 (1985).

5. J. Hager, M. Ivanco, M. A. Smith, and S. C. Wallace, *Chem. Phys.* **105**, 397 (1986).

6. J. W. Hager, D. R. Demmer, and S. C. Wallace, *J. Phys. Chem.* **91**, 1375 (1987).

7. G. A. Bickel, G. W. Leach, D. R. Demmer, J. W. Hager, and S. C. Wallace, *J. Chem. Phys.* **88**, 1 (1988).

8. G. A. Bickel, D. R. Demmer, E. A. Outhouse, and S. C. Wallace, *J. Chem. Phys.* **91**, 6013 (1989).

9. D. R. Demmer, G. W. Leach, E. A. Outhouse, J. W. Hager, and S. C. Wallace, *J. Phys. Chem.* **94**, 582 (1990).

10. E. A. Outhouse, G. A. Bickel, D. R. Demmer, and S. C. Wallace, *J. Chem. Phys.* **95**, 6261 (1991).

11. L. A. Philips and D. H. Levy, *J. Chem. Phys.* **85**, 1327 (1986).

12. G. Berden, W. L. Meerts, and E. Jalviste, *J. Chem. Phys.* **103**, 9596 (1995).

13. R. M. Helm, M. Clara, T. L. Grebner, and H. J. Neusser, *J. Phys. Chem. A* **102**, 3268 (1998).

14. T. M. Korter, D. W. Pratt, and J. Küpper, *J. Phys. Chem. A* **102**, 7211 (1998).

15. T. M. Korter, J. Küpper, and D. W. Pratt, *J. Chem. Phys.* **111**, 3946 (1999).

16. C. Kang, T. M. Korter, and D. W. Pratt, *J. Chem. Phys.* **122**, 174301 (2005).

17. C. Kang and D. W. Pratt, *Int. Rev. Phys. Chem.* **24**, 1 (2005).

18. C. Brand, J. Küpper, D. W. Pratt, W. L. Meerts, D. Krugler, J. Tatchen, and M. Schmitt, *Phys. Chem. Chem. Phys.* **12**, 4968 (2010).

19. J. Küpper, D. W. Pratt, W. L. Meerts, C. Brand, J. Tatchen, and M. Schmitt, *Phys. Chem. Chem. Phys.* **12**, 4980 (2010).

20. J. R. Johnson, K. D. Jordan, D. F. Plusquellic, and D. W. Pratt, *J. Chem. Phys.* **93**, 2258 (1990).

21. W. A. Majewski, J. F. Pfanstiel, D. F. Plusquellic, and D. W. Pratt, in *Laser Techniques in Chemistry*, edited by A. B. Myers and T. Rizzo (Wiley, New York, 1995), p. 101.

22. T. M. Korter, D. R. Borst, C. J. Butler, and D. W. Pratt, *J. Am. Chem. Soc.* **123**, 96 (2001).

23. D. F. Plusquellic, Ph.D. Thesis, University of Pittsburgh, 1992.

24. D. F. Plusquellic, R. D. Suenram, B. Mate, J. O. Jensen, and A. C. Samuels, *J. Chem. Phys.* **115**, 3057 (2001).

25. M. J. Frisch, G. W. Trucks, H. B. Schlegel, G. E. Scuseria, M. A. Robb, J. R. Cheeseman, J. Montgomery, J. A., T. Vreven, K. N. Kudin, J. C. Burant, J. M. Millam, S. S. Iyengar, J.

Tomasi, V. Barone, B. Mennucci, M. Cossi, G. Scalmani, N. Rega, G. A. Petersson, H. Nakatsuji, M. Hada, M. Ehara, K. Toyota, R. Fukuda, J. Hasegawa, M. Ishida, T. Nakajima, Y. Honda, O. Kitao, H. Nakai, M. Klene, X. Li, J. E. Knox, H. P. Hratchian, J. B. Cross, V. Bakken, C. Adamo, J. Jaramillo, R. Gomperts, R. E. Stratmann, O. Yazyev, A. J. Austin, R. Cammi, C. Pomelli, J. W. Ochterski, P. Y. Ayala, K. Morokuma, G. A. Voth, P. Salvador, J. J. Dannenberg, V. G. Zakrzewski, S. Dapprich, A. D. Daniels, M. C. Strain, O. Farkas, D. K. Malick, A. D. Rabuck, K. Raghavachari, J. B. Foresman, J. V. Ortiz, Q. Cui, A. G. Baboul, S. Clifford, J. Cioslowski, B. B. Stefanov, G. Liu, A. Liashenko, P. Piskorz, I. Komaromi, R. L. Martin, D. J. Fox, T. Keith, M. A. Al-Laham, C. Y. Peng, A. Nanayakkara, M. Challacombe, P. M. W. Gill, B. Johnson, W. Chen, M. W. Wong, C. Gonzalez, and J. A. Pople, GAUSSIAN 03 (Gaussian, Inc., Wallingford, CT, 2004).

26. T. H. Dunning Jr., *J. Chem. Phys.* **90**, 1007 (1989).

27. E. B. Wilson Jr., J. C. Decius, and P. C. Cross, *Molecular Vibrations: The Theory of Infrared and Raman Vibrational Spectra*. (Dover Publications, Inc., New York, 1955).

28. D. F. Plusquellic, X.-Q. Tan, and D. W. Pratt, *J. Chem. Phys.* **96**, 8026 (1992).

29. S. J. Humphrey and D. W. Pratt, *J. Chem. Phys.* **104**, 8332 (1996).

30. W. Gordy and R. Cook, L., *Microwave Molecular Spectra*, 2nd ed. (John Wiley & Sons, New York, 1984).

31. D. R. Herschbach, *J. Chem. Phys.* **31**, 91 (1959).

32. D. F. Plusquellic and D. W. Pratt, *J. Phys. Chem. A* **111**, 7391 (2007).

33. J. K. G. Watson, in *Vibrational Spectra and Structure*, edited by J. R. Durig (Elsevier Scientific Publishing Company, New York, 1977), Vol. 6, pp. 1.

34. A. C. Fantoni and W. Caminati, *J. Chem. Soc., Faraday Trans.* **92**, 343 (1996).

35. W. Caminati, J. C. Lopez, S. Blanco, S. Mata, and J. L. Alonso, *Phys. Chem. Chem. Phys.* **12**, 10230 (2010).

36. *Tables Relating to Mathieu Functions*. (Columbia University Press, New York, 1951).

37. W. Caminati and S. Di Bernardo, *J. Mol. Struct.* **240**, 253 (1990).

38. J. Kraitchman, *Am. J. Phys.* **21**, 17 (1953).

39. H. D. Rudolph, *J. Mol. Spectrosc.* **89**, 430 (1981).

40. D. R. Borst, Ph.D. Thesis, University of Pittsburgh, 2001.

41. J. G. Loeser, C. A. Schmuttenmaer, R. C. Cohen, M. J. Elrod, D. W. Steyert, R. J. Saykally, R. E. Bumgarner, and G. A. Blake, *J. Chem. Phys.* **97**, 4727 (1992).

42. G. Cotti, H. Linnartz, W. L. Meerts, A. van der Avoird, and E. H. T. Olthof, *J. Chem. Phys.* **104**, 3898 (1996).

43. E. N. Karyakin, G. T. Fraser, J. G. Loeser, and R. J. Saykally, *J. Chem. Phys.* **110**, 9555 (1999).

44. J. R. Platt, *J. Chem. Phys.* **17**, 484 (1949).

45. T. S. Zwier, *Annu. Rev. Phys. Chem.* **47**, 205 (1996).

46. In Ref. 14, the heavy-atom separation was reported to decrease by 0.1 Å. Using the same r_s method discussed here, we measure the hydrogen bond distance of InW to be 2.08 Å in S_0 and 1.99 Å in S_1.

47. C. Rensing, H. Maeder, and F. Temps, *J. Mol. Spectrosc.* **251**, 224 (2008).

48. A. J. Fleisher, J. W. Young, D. W. Pratt, W., A. Cembran, and J. Gao, *J. Chem. Phys.* **134**, 114304 (2011).

49. A. J. Fleisher, P. J. Morgan, and D. W. Pratt, *J. Chem. Phys.* **131**, 211101 (2009).

3.0 CHARGE TRANSFER BY ELECTRONIC EXCITATION: DIRECT MEASUREMENT BY HIGH RESOLUTION SPECTROSCOPY IN THE GAS PHASE

Reprinted with permission from *Journal of Chemical Physics*.

A.J. Fleisher, P.J. Morgan, and D.W. Pratt, *J. Chem. Phys*. **131**, 211101 (2009).

AJF and PJM performed the experimental measurements. AJF analyzed the spectra and performed theoretical calculations. AJF and DWP wrote the paper.

3.1 ABSTRACT

We report a quantitative measurement of the amount of charge that is transferred when the single ammonia complex of the photoacid β-naphthol (2HNA) is excited by light. The measurement was made by comparing the permanent electric dipole moments of *cis*-2HNA in its ground (S_0) and excited (S_1) states, determined by Stark-effect studies of its fully resolved $S_1 \leftarrow S_0$ electronic spectrum. While the increase in electron transfer from the donor (NH_3) to the acceptor (2HN) upon excitation is small (~0.05*e*), it is sufficient to redshift the electronic spectrum of the complex by ~600 cm^{-1} (~0.1 eV). Thereby explored is the incipient motion of the acid-base complex along the excited state (electron-coupled) proton transfer coordinate.

3.2 COMMUNICATION

The electronic structure of isolated molecules is of paramount importance to their chemical behavior. Organic and inorganic molecules must communicate efficiently with a variety of other entities to creating a working biological system. The most important building blocks of life, including nucleic acids,[1] the amino acids that form proteins,[2] and light harvesting chromophores comprising photosynthetic systems[3] cannot function without charge transfer (CT) processes. Complex systems such as membrane ion pumps, molecular wires, and bulk solvent systems all require organized charge motion along specific intra- and intermolecular coordinates.[4] In the field of nonlinear optics, CT states in organometallic systems often have large hyperpolarizabilities, and therefore important second-order optical properties essential for various materials science applications.[5]

Several experimental techniques have been used to directly observe CT in molecular systems.[6-20] Importantly, very few of these methods are capable of measuring the actual amount of charge transferred between the component parts of the studied molecular system, particularly in electronically excited states. Here, we demonstrate that this desirable objective can be achieved by comparing the permanent electric dipole moments (EDMs) of a solvent-solute cluster and its component parts before and after they are excited by light to promote CT,

Scheme 3-1

$$\mathrm{R-OH} + \mathrm{NH_3} \overset{h\nu}{\rightarrow} (R-O)^- \cdots (\mathrm{NH_4})^+.$$

Our "proof-of-principle" experiment was performed on a single conformer of the 1:1 acid-base complex of β-naphthol and ammonia (*cis*-2HNA) using rotationally resolved electronic Stark-effect spectroscopy in a molecular beam.[21,22] Previous experiments[10] have shown that this reaction occurs with unit efficiency in large clusters of $2HNA_n$ with $n \geq 4$. In the single ammonia complex, we thus explore incipient motion along the excited state proton transfer coordinate.

Figure 3-1 shows a portion of the fully resolved $S_1 \leftarrow S_0$ fluorescence excitation spectrum of *cis*-2HN at 30903.3 cm^{-1}, both in the absence[23] and presence[24] of an applied electric field. The Stark-induced splittings of the different M_J states is evident. To determine the permanent EDMs of the isolated molecules in both electronic states, ten Stark spectra were taken at full rotational resolution with applied electric fields ranging from 85 to 2115 V/cm. The experimental spectra were fit by carrying out exact diagonalizations of truncated matrices using the appropriate Hamiltonian for each electronic state,[22] and simulated using a Voigt line shape function.[25] The dipole moment components and standard deviations shown in Table 3-1 are taken

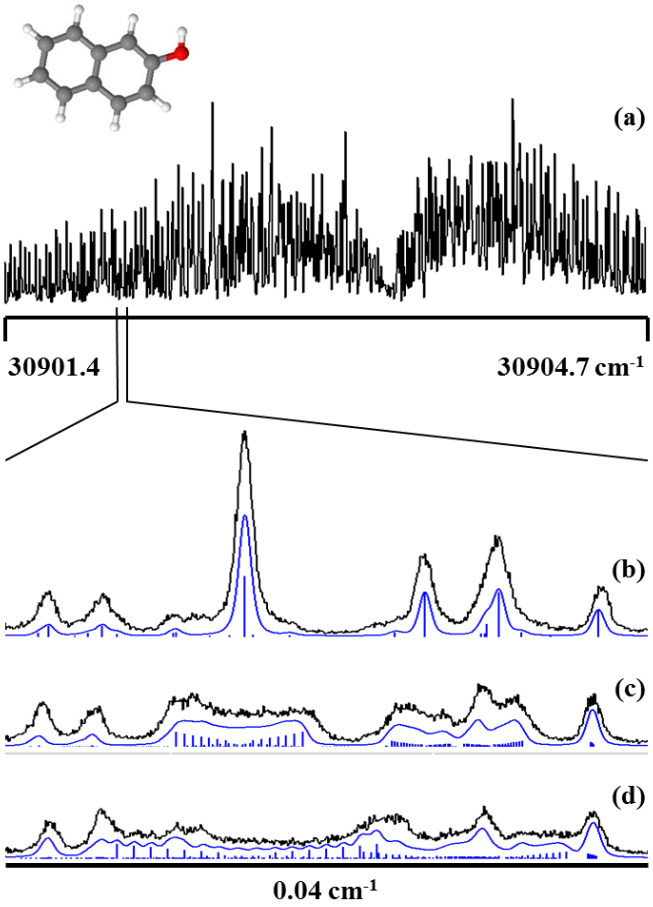

Figure 3-1. Shown in (a) is the zero-field origin band of the $S_1 \leftarrow S_0$ electronic spectrum of *cis*-2HN. At full rotational resolution, (b) shows a portion of the zero-field experimental spectrum (black trace) compared with the simulated spectrum (blue trace) using a convoluted line shape and a rotational temperature of 5 K. The most intense transition ($|J'\ K'_a\ K'_c\rangle \leftarrow |J''\ K''_a\ K''_c\rangle$) has the assigned quantum numbers $|854\rangle \leftarrow |963\rangle$. At applied electric fields of (c) 846 and (d) 1776 V/cm, the simulated spectra using the dipole moment projections listed in Table 3-1 are in excellent agreement with the experiment.

Table 3-1. Experimental permanent EDMs of *cis*-2HN and *cis*-2HNA. The dipole moment angle with respect to the *a* inertial axis is defined as θ_a.

	cis-2HN	*cis*-2HN·NH_3
S_0		
μ_a (D)	±0.344(3)	∓2.56(2)
μ_b (D)	∓0.951(8)	∓2.93(4)
μ_c (D)	0.00(2)	0.00(2)
μ (D)	1.01(1)	3.89(4)
θ_a (deg)	70.1(4)	131.2(9)
S_1		
μ_a (D)	∓0.159(3)	∓3.76(2)
μ_b (D)	∓1.160(8)	∓3.21(4)
μ_c (D)	0.00(2)	0.00(1)
μ (D)	1.17(1)	4.94(4)
θ_a (deg)	97.8(4)	139.6(9)

from a least-squares fit of 254 transitions at a field of 1269 V/cm, with an observed-minus-calculated (OMC) standard deviation of 3.0 MHz, small compared with the single rovibronic linewidth of ~33 MHz. *Ab initio* (MP2 and CIS levels of theory)[26] values are listed in Appendix B. The calculations show that the EDM orientations in 2HN are dominated by the lone pairs of electrons on the oxygen atom. The change in magnitude of the *cis*-2HN EDM upon excitation to the S_1 state is $\Delta\mu = 0.16(2)$ D, small compared with solvatochromic estimates of 0.5 D (Table 8-1 of Ref. 8).

The situation is changed dramatically by the attachment of a single ammonia molecule to *cis*-2HN. Figure 3-2 shows rotationally resolved electronic spectra of the $S_1 \leftarrow S_0$ origin band of *cis*-2HNA, which consists of two overlapping subbands (owing to an internal-rotation tunneling motion of the attached NH_3) at 30317.7 and 30316.9 cm^{-1}, respectively.[22] In the Stark experiments on the complex, a total of seven spectra were taken of the two subbands at applied electric fields ranging from 211 to 2115 V/cm. These were fit in a similar manner; for both *cis*-2HN and *cis*-2HNA, a rotational temperature of 5 K as well as all zero-field inertial parameters were held constant during the Stark fitting process. Figure 3-2 shows the high accuracy of these fits for both the *A* and *E* subbands over several applied fields. The EDM components and standard deviations for *cis*-2HNA listed in Table 3-1 were taken from a fit of 87 transitions within the *A* band at a field of 1269 V/cm, with an OMC of 5.1 MHz. Immediately apparent upon comparison of these data to those of *cis*-2HN are two facts; the magnitude of the EDM is much larger in the complex than in the isolated molecule (3.89 *versus* 1.01 D in the S_0 state) and the EDM of the complex increases substantially when it is excited by light (4.94 D in S_1 *versus* 3.89 D in S_0), a change of nearly 30%. There also are significant light-induced changes in the orientations of the EDMs in the two species.

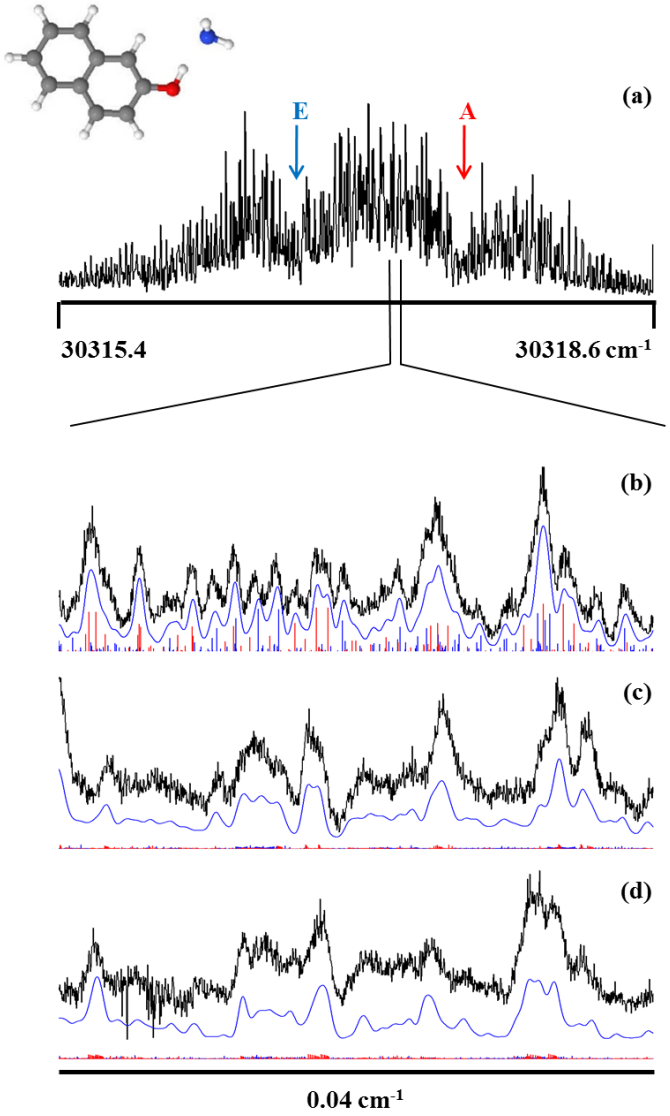

Figure 3-2. Shown in (a) is the zero-field origin of the $S_1 \leftarrow S_0$ electronic spectrum of *cis*-2HNA, containing the overlapping *A* and *E* subbands. At full rotational resolution, (b) contains the zero-field experimental spectrum (black trace) compared with the simulated spectrum (blue trace, *A* subband transitions in blue, *E* subband transitions in red) using a convoluted line shape, a rotational temperature of 5 K, and the addition of both simulated subbands. Spectra obtained at (c) 423 and (d) 1269 V/cm are shown along with the spectra simulated using the dipole projections from Table 3-1.

Insight into the origin of these differences is provided by a comparison of the present results on *cis*-2HNA with those of a similar system, indole-H_2O.[27] There it was found that the (S_0 and S_1) EDMs of the complex also are different from those of the isolated molecule, and that the complex EDMs are not equal to the simple vector sum of the EDMs of the component parts; in this case, isolated indole and water molecules. Careful consideration of the possible reasons for these differences then showed that quantitative agreement between theory and experiment could be achieved by postulating the existence of an induced dipole moment, produced by attaching the water dipole (and quadrupole) to the polarizable indole molecule. (Parenthetically, it is important to note that the experiment places significant constraints on a calculation of this sort, since both the distance between the attached solvent molecule and its orientation relative to the solute are known for both electronic states from the rotationally resolved spectra.)

In the case of *cis*-2HNA, it is clear upon inspection of Table 3-1 that the complex EDMs in the two electronic states also are not simply equal to the vector sum of the EDMs of the component parts [*cis*-2HN = 1.01 D in S_0, 1.17 D in S_1, and NH_3 = 1.472 D[28]]. Further, as shown in Table 3-2, values of the induced EDMs (calculated from the *ab initio* molecular polarizabilities of *cis*-2HN and the dipole and quadrupole moments of NH_3[28,29]) are not large enough to make up the substantial difference between a vector model calculation and experiment. We therefore postulate the existence of an additional contribution to the EDM of *cis*-2HNA, CT between the "solvent" and "solute," and write

Equation 3-1

$$\vec{\mu}_{c2\mathrm{HNA}} = \vec{\mu}_{c2\mathrm{HN}} + \vec{\mu}_{\mathrm{NH_3}} + \vec{\mu}_{\mathrm{ind}} + \vec{\mu}_{\mathrm{CT}}.$$

Here, $\vec{\mu}_{c2\mathrm{HNA}}$ is the permanent EDM of the complex, $\vec{\mu}_{c2\mathrm{HN}}$ is the permanent EDM of bare *cis*-2HN, $\vec{\mu}_{\mathrm{NH_3}}$ is the permanent EDM of ammonia, $\vec{\mu}_{\mathrm{ind}}$ is the induced EDM (calculated from the molecular polarizability of *cis*-2HN and the dipole and quadrupole moments of NH_3,[28,29] separated by R_{CM}, the distance between the centers of mass of *cis*-2HN and NH_3[22]), and $\vec{\mu}_{\mathrm{CT}}$ is the contribution to from CT in both electronic states. (All vectors contributing to $\vec{\mu}_{c2\mathrm{HNA}}$ have been expressed in the principal axis system of the complex[30] and are illustrated in Fig. 3-3.) Then, after completing the vector subtraction

Equation 3-2

$$\vec{\mu}_{\mathrm{CT}} = \vec{\mu}_{c2\mathrm{HNA}} - \vec{\mu}_{c2\mathrm{HN}} - \vec{\mu}_{\mathrm{NH_3}} - \vec{\mu}_{\mathrm{ind}}$$

and taking the projection of the remaining EDM onto the hydrogen bond axis (assumed to be the internal rotation axis of NH_3), the magnitude of CT was calculated using $\vec{\mu}_{\mathrm{CT}} = Qd$, where d is the heavy atom separation along the hydrogen bond in both electronic states.[22] We find, from experiment, the magnitude of CT to be $Q = 0.09e$ in S_0 and $Q^* = 0.14e$ in S_1. (The derived values of Q and Q^* are very sensitive to the hydrogen bond axis orientation.)

Of course, the model used to describe the observed behavior is only approximate. It relies on the adequacy of a multipole expansion at close range and on *ab initio* polarizabilities. The multipole expansion is expected to diverge if the center of mass distance R_{CM} is less than the spatial extent of the two interacting charge distributions.[31] However, while they have nearly the same magnitudes, the EDMs of *cis*-2HN and *trans*-2HN are oriented in opposite directions. Thus, most of the relevant charge in *cis*-2HNA is localized on the two heavy atoms (O and N), whose separation is much less than R_{CM}. Also, the *cis*-2HNA dipole-quadrupole term is

Table 3-2. Calculated dipole-dipole, polarizability-electric field, and charge-charge interaction energies of *cis*-2HNA. Below, *cis*-2HN is designated as 1, and NH_3 is designated as 2. The angles θ_1 and θ_2 are the angles that μ_1 and μ_2 make with the line R_{CM} (Ref. 32).

	S_0	S_1
μ_1 (D)	1.01	1.17
μ_2 (D)	1.472[a]	1.472[a]
μ_{ind} (D)	0.40 (0.41)[b]	0.50 (0.50)[b]
θ_1 (deg)	9.22	19.36
θ_2 (deg)	47.98	10.74
R_{CM} (Å)	5.251[c]	5.157[c]
Q (e)	0.09 (0.09)[b]	0.14 (0.14)[b]
d (Å)	2.77[c]	2.62[c]
$E_{\mu\mu}$ (cm^{-1})	-62.2	-113.4
$E_{\alpha\mu}$ (cm^{-1})	-20.3 (-20.8)[b]	-26.7 (-26.7)[b]
E_{CT} (cm^{-1})	-339.6	-868.8
$E_{complex,rel}$ (cm^{-1})	-422.1(-422.6)[b]	-1008.9 (-1008.9)[b]

[a]Reference 28.

[b]Including the quadrupole moment of ammonia (see Ref. 27).

[c]Reference 22.

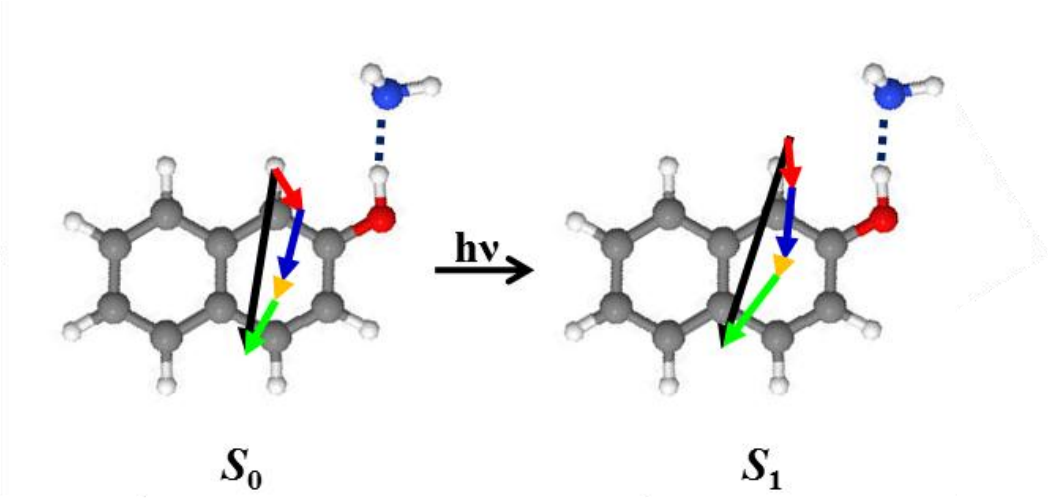

Figure 3-3. The S_0 and S_1 dipole moments of *cis*-2HNA (black). This figure illustrates the components of Eq. 3-1, where μ_{c2HN} (red), μ_{NH_3} (blue), μ_{ind} (orange), and μ_{CT} (green) add to reproduce μ_{c2HNA} (black).

significantly less than the dipole-dipole one (*cf.* Table 3-2), suggesting convergence of the multipole expansion. And, while the *ab initio* polarizabilities are only estimates, especially with such a small basis set, they successfully account for the differences between the measured and predicted dipole moments of indole-H_2O.[27] Therefore, we believe that our model, although primitive, captures the essential physics of the interaction between *cis*-2HNA and the attached ammonia molecules.

We can test our experimentally determined values of Q and Q^* in *cis*-2HNA by using them to calculate the electronic stabilization energy for the complex, relative to the bare molecule, from the relation

Equation 3-3

$$E_{\text{complex,rel}}^{S_0,S_1} = E_{\mu\mu} + E_{\alpha\mu} + E_{\text{CT}}.$$

Here, $E_{\mu\mu}$ is the interaction energy of the two dipoles separated by the distance R_{CM}, $E_{\alpha\mu}$ is the interaction energy of the polarizable *cis*-2HN with the electric field of NH_3 (at the same distance R_{CM}), and E_{CT} is the interaction energy between two point charges, separated by the previously mentioned heavy atom distance d.[32] The resulting values are listed in Table 3-2. Comparing the values of $E_{\text{complex,rel}}$ for the two states leads to an estimate of the redshift of *cis*-2HN solvated by a single ammonia molecule. The results is $\Delta E_{\text{complex,rel}}^{S_1 \leftarrow S_0} = -586$ cm^{-1}, in excellent agreement with the experimental value of -585 cm^{-1}. This agreement corroborates our derived values of Q and Q^*, and shows that CT is the dominant component of the stabilization energy, $E_{\text{complex,rel}}$ (~85%).

It is noteworthy that the measured value of charge separation in the formation of the hydrogen bond in the ground state of *cis*-2HNA, Q ~0.1e, is consistent with previous estimates

of this quantity obtained for other systems through theoretical calculations using a Mulliken population analysis[14] and by microwave spectroscopy.[17] The hydrogen bond in the ground state of *cis*-2HNA is ~10% ionic, ~15% ionic in the excited state.

For over 50 years, 2HN and a variety of other photoacids[33] have been the subject of extensive condensed phase experiments, including several solvatochromic investigations.[34] This vast body of literature has provided a wealth of information on intermolecular interactions, and how they are influenced by the absorption of light.[7] For example, use of the Förster cycle[35] led to estimates of the 2HN excited state acidity constant pK_a^* ~2.8, compared with the ground state value of pKa ~9.5, and fueled much speculation about the role of the solvent in excited state proton transfer reactions. The present results show that a single solvent molecule is capable of increasing proton transfer in the excited state by ~50%, relative to the ground state. But a much larger factor is needed to explain the large change in pK_a values of 2HN on absorption of light. Future experiments of this type will focus on the role of additional solvent molecules in producing this change, as well as CT processes in biological systems.

3.3 ACKNOWLEDGEMENTS

We would like to thank the Center for Molecular and Materials Simulations (CMMS) at the University of Pittsburgh for computing time. We also would like to acknowledge helpful discussions with D.M. Miller about the Stark program, C.-H. Kang about induced dipole moments, D.J. Fox about theoretical polarizabilities, and M.A. Ratner about charge transfer. This research has been supported by NSF (CHE-0615755 and CHE-0911117).

3.4 REFERENCES

1. B. Xu, P. Zhang, X. Li, and N. Tao, *Nano Lett.* **4**, 1105 (2004); H. Cohen, C. Nogues, R. Naaman, and D. Porath, *Proc. Natl. Acad. Sci. U.S.A.* **102**, 11589 (2005); T. Kubar, P. B. Woiczikowski, G. Cuniberti, and M. Elstner, *J. Phys. Chem. B* **112**, 7937 (2008); T. Kubar and M. Elstner, *J. Phys. Chem. B* **113**, 8788 (2008); S. S. Mallajosyula, A. Gupta, and S. K. Pati, *J. Phys. Chem. A* **113**, 3955 (2009).

2. C. J. Chang, M. C. Y. Chang, N. H. Damrauer, and D. G. Nocera, *Biochim. Biophys. Acta* **1655**, 13 (2004); C. Wittekindt, M. Schwarz, T. Friedrich, and T. Koslowski, *J. Am. Chem. Soc.* **131**, 8134 (2009).

3. E. L. Read, G. S. Engel, T. R. Calhoun, T. Mancal, T. K. Ahn, R. E. Blankenship, and G. R. Fleming, *Proc. Natl. Acad. Sci. U.S.A.* **104**, 14203 (2007); T. K. Ahn, T. J. Avenson, M. Ballottari, Y. –C. Cheng, K. K. Niyogi, R. Bassi, and G. R. Fleming, *Science* **320**, 794 (2008); E. Romero, M. Mozzo, I. H. M. van Stokkum, J. P. Dekker, R. van Grondelle, and R. Croce, *Biophys. J.* **96**, L35 (2009).

4. R. A. Marcus, *Adv. Chem. Phys.* **106**, 1 (1999).

5. N. J. Long, *Angew. Chem., Int. Ed. Engl.* **34**, 21 (1995); S. D. Cummings, L.-T. Cheng, and R. Eisenberg, *Chem. Mater.* **9** 440 (1997).

6. N. Shafizadeh, B. Soep, J. M. Mestdagh, and W. H. Breckenridge, *Int. Rev. Phys. Chem.* **28**, 359 (2009).

7. N. Mataga and T. Kubota, *Molecular Interactions and Electronic Spectra* (Marcel Dekker, New York, 1970).

8. P. Suppan, *J. Photochem. Photobiol., A* **50**, 293 (1990).

9. D. H. Levy, *Adv. Chem. Phys.* **106**, 203 (1999); S. Jiang and D. H. Levy, *J. Phys. Chem. A* **107**, 6785 (2003); C. A. Southern, D. H. Levy, J. A. Stearns, G. M. Florio, A. Longarte, and T. S. Zwier, *J. Phys. Chem. A* **108**, 4599 (2004).

10. O. Cheshnovsky and S. Leutwyler, *J. Chem. Phys.* **88**, 4127 (1988); T. Droz, R. Knochenmuss, and S. Leutwyler, *J. Chem. Phys.* **93**, 4520 (1990).

11. Y. Matsumoto, T. Ebata, N. Mikami, *J. Mol. Struct.* **552**, 257 (2000).

12. H. Wang, T. C. Steimle, C. Apetrei, and J. P. Maier, *Phys. Chem. Chem. Phys.* **11**, 2649 (2009).

13. J. R. Roscioli, E. G. Diken, M. A. Johnson, S. Horvath, and A. B. McCoy, *J. Phys. Chem. A* **110**, 4943 (2006); S. Horvath, A. B. McCoy, J. R. Roscioli, and M. A. Johnson, *J. Phys. Chem. A* **112**, 12337 (2008).

14. J. M. Herbert and M. Head-Gordon, *J. Am. Chem. Soc.* **128**, 13932 (2006).

15. M. P. de Haas and J. M. Warman, *Chem. Phys.* **73**, 35 (1982); W. Schuddeboom, S. A. Jonker, J. M. Warman, M. P. de Haas, M. J. W. Vermeulen, W. F. Jager, B. de Lange, D. L. Feringa, and R. W. Fessenden, *J. Am. Chem. Soc.* **115**, 3286 (1993).

16. A. D. Buckingham, P. W. Fowler, A. C. Legon, S. A. Peebles, and E. Steiner, *Chem. Phys. Lett.* **232**, 437 (1995); A. C. Legon, in *Structure and Bonding*, edited by P. Metrangolo and G. Resnati (Springer-Verlag, Berlin, 2008), Vol. 126, p. 17.

17. M. E. Ott and K. R. Leopold, *J. Phys. Chem. A* **103**, 1322 (1999); D. L. Fiacco, Y. Mo, S. W. Hunt, M. E. Ott, A. Roberts, and K. R. Leopold, *J. Phys. Chem. A* **105**, 484 (2001).

18. S. Sensfuss, A. Konkin, H. K. Roth, M. Al-Ibrahim, U. Zhokhavets, G. Gobsch, V. I. Krinichnyi, G. A. Nazmutdinova, and E. Klemm, *Synth. Met.* **137**, 1433 (2003).

19. M. Gu, S. Wang, J. Wu, D. Feng, and W. Xu, *Chem. Phys. Lett.* **411**, 167 (2005).

20. F. Gutmann, C. Johnson, H. Keyzer, and J. Molnar, *Charge Transfer Complexes in Biological Systems* (Marcel Dekker, New York, 1997).

21. J. R. Johnson, K. D. Jordan, D. F. Plusquellic, and D. W. Pratt, *J. Chem. Phys.* **93**, 2258 (1990).

22. D. F. Plusquellic, X.-Q. Tan, and D. W. Pratt, *J. Chem. Phys.* **96**, 8026 (1992).

23. W. A. Majewski, J. F. Pfanstiel, D. F. Plusquellic, and D. W. Pratt, in *Laser Techniques in Chemistry*, edited by A. B. Myers and T. Rizzo (Wiley, New York, 1995), p. 101.

24. T. M. Korter, D. R. Borst, C. J. Butler, and D. W. Pratt, *J. Am. Chem. Soc.* **123**, 96 (2001).

25. J. J. Olivero and R. L. Longbothum, *J. Quant. Spectrosc. Radiat. Transf.* **17**, 233 (1977).

26. M. J. Frisch, G. W. Trucks, H. B. Schlegel, G. E. Scuseria, M. A. Robb, J. R. Cheeseman, J. Montgomery, J. A., T. Vreven, K. N. Kudin, J. C. Burant, J. M. Millam, S. S. Iyengar, J. Tomasi, V. Barone, B. Mennucci, M. Cossi, G. Scalmani, N. Rega, G. A. Petersson, H. Nakatsuji, M. Hada, M. Ehara, K. Toyota, R. Fukuda, J. Hasegawa, M. Ishida, T. Nakajima, Y. Honda, O. Kitao, H. Nakai, M. Klene, X. Li, J. E. Knox, H. P. Hratchian, J. B. Cross, V. Bakken, C. Adamo, J. Jaramillo, R. Gomperts, R. E. Stratmann, O. Yazyev, A. J. Austin, R. Cammi, C. Pomelli, J. W. Ochterski, P. Y. Ayala, K. Morokuma, G. A. Voth, P. Salvador, J. J. Dannenberg, V. G. Zakrzewski, S. Dapprich, A. D. Daniels, M. C. Strain, O. Farkas, D. K. Malick, A. D. Rabuck, K. Raghavachari, J. B. Foresman, J. V. Ortiz, Q. Cui, A. G. Baboul, S. Clifford, J. Cioslowski, B. B. Stefanov, G. Liu, A. Liashenko, P. Piskorz, I. Komaromi, R. L. Martin, D. J. Fox, T. Keith, M. A. Al-Laham, C. Y. Peng, A. Nanayakkara, M. Challacombe, P. M. W. Gill, B. Johnson, W. Chen, M. W. Wong, C. Gonzalez, and J. A. Pople, GAUSSIAN 03 (Gaussian, Inc., Wallingford, CT, 2004).

27. C. Kang, T. M. Korter, and D. W. Pratt, *J. Chem. Phys.* **122**, 174301 (2005).

28. M. D. Marshall and J. S. Muenter, *J. Mol Spectrosc.* **85**, 322 (1981).

29. S. G. Kukolich, *Chem. Phys. Lett.* **5**, 401 (1970).

30. J. Kraitchman, *Am. J. Phys.* **21**, 17 (1953); H. D. Rudolph, *J. Mol. Spectrosc.* **89**, 430 (1981); W. Gordy and R. L. Cook, *Microwave Molecular Spectra*, 2nd ed. (John Wiley & Sons, New York, 1984).

31. A. J. Stone, *The Theory of Intermolecular Forces* (Clarendon, Oxford, 1996).

32. G. C. Maitland, M. Rigby, E. B. Smith, and W. A. Wakeham, *Intermolecular Forces* (Clarendon, Oxford, 1981).

33. D. Huppert, L. M. Tolbert, and S. Linares-Samaniego, *J. Phys. Chem. A* **101**, 4602 (1997); K. M. Solntsev, D. Huppert, and N. Agmon, *J. Phys. Chem. A* **102**, 9599 (1998); C. Clower, K. M. Solntsev, J. Kowalik, L. M. Tolbert, and D. Huppert, *J. Phys. Chem. A* **106**, 3114 (2002).

34. A. Weller, in *Progress in Reaction Kinetics*, edited by G. Porter (Pergamon, New York, 1961) Vol 1, p. 187; E. V. Donckt, in *Progress in Reaction Kinetics*, edited by G. Porter (Pergamon, New York, 1970), Vol. 5, p. 273.

35. T. Förster, *Naturwiss.* **36**, 186 (1949); T. Förster, *Z. Elektrochem.* **54**, 531 (1950).

36. See EPAPS supplementary material at http://dx.doi.org/10.1063/1.3259690 E-JCPSA6-131-003944 for a comparison of experimental and theoretical EDMs.

4.0 FLICKERING DIPOLES IN THE GAS PHASE. STRUCTURES, INTERNAL DYNAMICS, AND DIPOLE MOMENTS OF β-NAPHTHOL-H_2O IN ITS GROUND AND EXCITED ELECTRONIC STATES

Reprinted with permission from *Journal of Chemical Physics*.

Adam J. Fleisher, Justin W. Young, David W. Pratt, Alessandro Cembran, and Jiali Gao,

J. Chem. Phys. **134**, 114304 (2011).

AJF performed the experimental measurements, analyzed the spectra, and performed some theoretical calculations. JWY and AJF determined the barrier heights to internal rotation. AC and JG performed the energy and dipole moment decomposition theoretical calculations. AJF and DWP wrote the paper.

4.1 ABSTRACT

Described here are the rotationally resolved S_1-S_0 electronic spectra of the acid-base complex β-naphthol-H_2O in the gas phase, both in the presence and absence of an applied electric field. The data show that the complex has a *trans*-linear $O-H\cdots O$ hydrogen bond configuration involving the $-OH$ group of β-naphthol and the oxygen lone pairs of the attached water molecule in both electronic states. The measured permanent electric dipole moments of the complex are 4.00 and 4.66 D in the S_0 and S_1 states, respectively. These reveal a small amount of photoinduced charge transfer between solute and solvent, as supported by density functional theory calculations and an energy decomposition analysis. The water molecule also was found to tunnel through a barrier to internal motion nearly equal in energy to kT at room temperature. The resulting large angular jumps in solvent orientation produce "flickering dipoles" that are recognized as being important to the dynamics of bulk water.

4.2 INTRODUCTION

Gas phase studies of monosolvated water clusters have a rich history, and have profited greatly from the advancement of jet-cooled experimental techniques. One-to-one hydrogen bonded systems between fluorescent organic molecules and water report information about the preferred binding sites of solvent, intermolecular motions, and the extent to which the solute molecule is perturbed by the attachment of a single solvent molecule. Direct gas phase studies of specific solvent stabilization also aid in the analysis of condensed phase solvatochromism, as well as in the advancement of *ab initio*, density functional, and bulk solvent force field theoretical methods.

The simplest aromatic alcohol is phenol, which serves as the chromophore of the amino acid tyrosine. The phenol-H_2O complex was first observed in a supersonic expansion by Abe, Mikami, and Ito in 1982,[1] and subsequent jet-cooled studies combined with extensive theoretical analysis have provided a vast amount of information on the hydrogen bond (HB) orientation, stabilization energy, and internal dynamics within the 1:1 cluster.[2] High resolution microwave[3] and electronic[4] spectroscopy studies have determined the precise geometry of the phenol-H_2O cluster, in both the ground (S_0) and first excited (S_1) electronic states, and quantified the internal dynamics of the attached water molecule. The high resolution work revealed a tunneling motion between the equivalent minima of a symmetric double-well potential governing the complex internal dynamics of water about the phenol-H_2O HB. The barrier height to this motion was experimentally determined using a one-dimensional (1D) model to be 177 and 127 cm^{-1} in the S_0 and S_1 states, respectively.[4]

The larger aromatic alcohol β-naphthol (2-hydroxynaphthalene, 2HN) is known to form HB arrangements with water in supersonic expansions that are similar to those of phenol.[5] Unlike phenol, there are two stable conformers of 2HN, owing to a *trans* or *cis* orientation of the hydroxyl group relative to the naphthalene ring.[6] Each of these conformers can form a 1:1 complex with water, *trans*- and *cis*-2HNW, as shown below:

Scheme 4-1

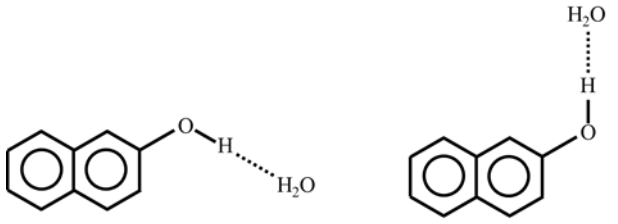

trans-2HNW *cis*-2HNW

Structures of these two 1:1 complexes have been studied theoretically[7] as well as with infrared-ultraviolet double-resonance techniques.[8,9] The permanent electric dipole moments (EDMs) of *cis*-2HN in both electronic states are known from experiment.[10] Here, we report measurements of the EDMs of *cis*-2HNW from which information about the degree of charge redistribution on complex formation is derived by comparison with the results for the isolated molecule. Being rotationally resolved, the experiments also provide detailed structural information about *cis*-2HNW, including the HB distances in both electronic states. Since the spectrum reveals a tunneling motion of the water molecule analogous to that observed in phenol-H_2O, barrier heights for the combined torsion-inversion potential also have been derived from the high resolution data. These results reveal that the attached water molecule undergoes discontinuous angular jumps in its orientation with respect to the β-naphthol molecule to which it is attached. Similar "flickering dipoles" have been proposed to occur in liquid water as a consequence of the breaking and making of HBs.

4.3 METHODS

4.3.1 Experimental

Rotationally resolved electronic spectra were recorded using a high resolution laser apparatus, consisting of a tunable continuous-wave ultraviolet (UV) laser which intersects a perpendicularly propagating cold molecular beam.[11] A modified ring dye laser operating with DCM laser dye was pumped with an argon ion laser (514.5 nm), yielding continuous fundamental visible

radiation. The fundamental radiation was frequency doubled using a BBO doubling crystal cut at Brewster's angle for 655 nm light, producing ~ 500 μW of ultraviolet power (1 MHz bandwidth) and allowing for a scan range of 2 cm^{-1} in the UV. The recorded spectra were calibrated using the absorption spectrum of iodine, resulting in an absolute frequency calibration of ± 30 MHz. Relative frequency markers from a temperature stabilized etalon were recorded throughout the scan, with a spacing of 599.5040 MHz in the UV, resulting in a relative frequency calibration of ± 0.0005 MHz.

β-Naphthol was purchased from Aldrich, heated to 370 K in a quartz source, and seeded in a backing gas of argon and water at a total pressure of ~ 380 torr. Water was introduced into the backing gas prior to the source by passing dry argon over a room temperature water trap. The gas expansion consisting of 2HN, H_2O, and Ar was skimmed 2 cm after leaving the source (240 μm diameter), resulting in a molecular beam with a rotational temperature of 6 ± 2 K. The molecular beam was crossed with the focused UV laser beam 15 cm downstream from the initial expansion, producing a Doppler component to the overall spectral line width of 25 MHz. Total fluorescence upon photon absorption was collected using spherical collection optics and focused perpendicular to both beams into a photomultiplier tube and photon counting system. Wire mesh plates separated by 1 cm were located above and below the beam intersection in order to introduce a homogeneous electric field for Stark measurements.[12] The known ground state EDM of aniline (1.329 D)[13] was used for Stark calibration. Data was collected using JBA95 acquisition software,[14] and all spectra were analyzed with the JB95 fitting program.[15]

4.3.2 Theoretical

At the University of Pittsburgh, theoretical calculations were performed using GAUSSIAN03 (G03)[16] to support the experimental data. Water was initially attached to a previously optimized (MP2/6-31G**) ground state structure of *cis*-2HN. Then, the M05-2X hybrid density functional[17] was used to optimize the ground state geometry of *cis*-2HNW (aug-cc-pVDZ basis set[18]), while a configuration interaction singles (CIS)[19] optimization was employed, beginning with the optimized ground state cluster structure, to estimate the first excited state cluster geometry with the same basis set. Two starting hydrogen bond orientations, one along the C_2 symmetry axis of H_2O, and another using a single lone pair of the oxygen atom, resulted in the same optimized ground state geometry shown in Fig. 4-1. The internal motion of water relative to 2HN was explored at the Hartree-Fock (HF) level of theory with the 6-31+G* basis set[20] using the quadratic synchronous transit (QST)[21] method available in G03.

At the University of Minnesota, full geometry optimizations were independently performed with G03 with the addition of the Minnesota density functional module 4.1.[16] The density functional M06-2X[22] was used together with the 6-31+G* basis set. For selected structures, further single point calculations on the M06-2X/6-31+G* structure were performed at the following levels; M06-2X/MG3,[23] MP2/6-31+G*, MP2/MG3, and MP2/aug-cc-pVDZ. For the most stable of the clusters, a minimization at the M06-2X/MG3 level was also carried out to test the effect of a large basis set on the cluster geometry, which was determined to be negligible. Additionally, for the isolated ammonia molecule MP2/aug-cc-pVTZ and aug-cc-pVQZ calculations confirmed that the theoretical EDM is already converged at the smaller aug-cc-pVDZ level.

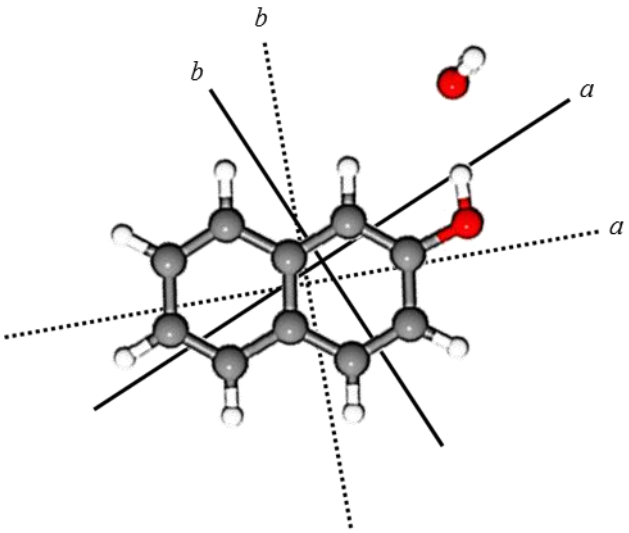

Figure 4-1. Ground state structure of *cis*-2HNW (M05-2X/aug-cc-pVDZ, see Table 4-1 for rotational constants). The in-plane inertial axes of *cis*-2HNW are shown as solid lines. The corresponding inertial axes of *cis*-2HN are shown as dashed lines.

Also, energy decomposition was performed with the block-localized density functional theory (BLDFT) method using the Xiamen valence bond (XMVB) program[24] and a modified version of GAMESS.[25] We used a version of the B3LYP implementation that employs the VWN1 functional rather than the VWN5 functional in the standard B3LYP model.[26] The effect of increasing basis set size was tested by using 6-31+G* and aug-cc-pVDZ basis sets. The geometries used for energy and dipole decomposition were those optimized with G03 at the M06-2X/6-31+G* level.

4.4 RESULTS AND INTERPRETATION

4.4.1 Rotationally resolved electronic spectrum

Fluorescence from *cis*-2HNW was collected by selectively exciting its known electronic origin band at 30532 cm^{-1}, identified by previous REMPI experiments.[27] The high resolution electronic spectrum of the *cis*-2HNW origin band (red shifted by 371 cm^{-1} from the origin band of the bare molecule) is shown in Fig. 4-2. The spectrum is dense, covering ~ 2 cm^{-1}; there are more than 1000 transitions lying within this bandwidth. Partly, this congestion is caused by the presence of two overlapping subbands in the spectrum, produced by a tunneling motion of the attached water molecule. We analyze each of these subbands separately here. Later, we will compare the results of the two fits in order to extract information about the water motion.

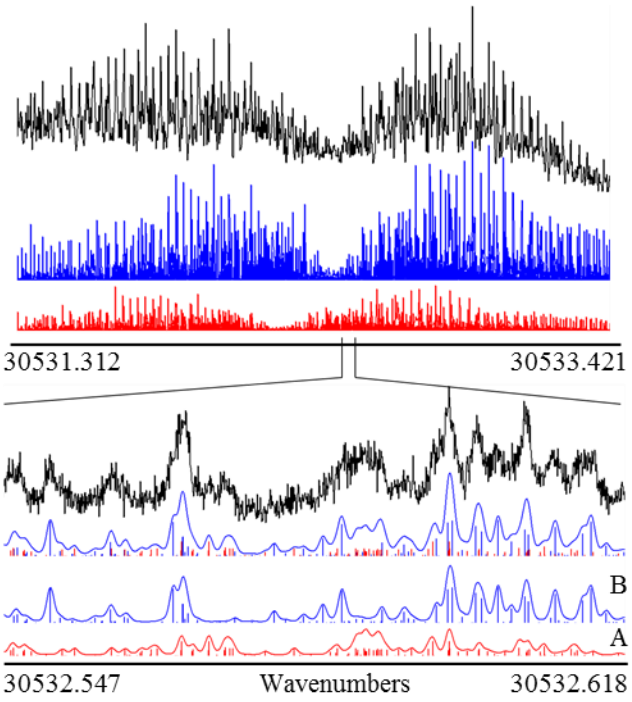

Figure 4-2. The rotationally resolved spectrum of *cis*-2HNW. The A ($\sigma = 0$) subtorsional band is shown in red (relative intensity of 1), while the B ($\sigma = 1$) subtorsional band simulation is shown in blue (relative intensity of 3). At full rotational resolution, the fit of the combined simulation to experiment is excellent.

The spectrum shown in Fig. 4-2 has no central Q branch. Hence, it was simulated using *b*-type selection rules and a rigid-rotor Hamiltonian for each electronic state,

Equation 4-1

$$\widehat{H}_r = A\hat{P}_a^2 + B\hat{P}_b^2 + C\hat{P}_c^2.$$

Here, $\hat{P}_g$ $(g = a, b, c)$ are the projections of the rotational angular momentum on the inertial axes, and *A*, *B*, and *C* are the rotational constants ($A = h/8\pi^2 I_a$, *etc.*). Preliminary values of these constants were taken from similar molecular systems and then varied in a least-squares fashion using JB95[15] to obtain a best fit (see Fig. 4-2 and Table 4-1). Equation 4-1 was adequate for transitions involving low *J* states (< 25). Higher *J* transition fits were improved by the addition of Watson's distortion terms (A-reduction),[28] but these did not change the measured "rigid rotor" constants by more than one standard deviation. A rotational temperature of 6.0 ± 2.0 K was derived from the fit; analysis of the observed Voigt profiles of single rovibronic transitions gave Gaussian and Lorentzian contributions of 25 and 5 MHz to the linewidths (τ_f = 35 ns).

Several pieces of information may be derived from the data listed in Table 4-1. The first is the location of the water molecule in the complex, which can be determined from a comparison of its inertial constants with those of bare *cis*-2HN,[6] using Kraitchman's equations.[29] From this analysis, the center of mass (COM) of water was determined to be 5.15 Å from the COM of *cis*-2HN in S_0, and 5.11 Å in S_1. Four possible point mass locations result; see Table 4-2 and Fig. 4-2. From there, it is evident that the water COM lies in (or nearly in) the plane of *cis*-

Table 4-1. Inertial parameters of *cis*-2HNW. The theoretical constants were calculated using M05-2X/aug-cc-pVDZ in S_0 and CIS/aug-cc-pVDZ in S_1.

	Measured constants		Rigid-body constants[a]	Theoretical constants
	σ = 0 (A)	σ = 1 (B)		
S_0				
A'' (MHz)	1725.9(1)	1724.9(1)	1725.4	1725.3
B'' (MHz)	548.1(1)	548.1(1)	548.1	554.3
C'' (MHz)	416.6(1)	416.8(1)	416.7	420.4
ΔI'' (uÅ^2)	-1.781	-2.609	-2.19	-2.53
S_1				
A' (MHz)	1687.4(1)	1686.3(1)	1686.9	1685.3
B' (MHz)	553.4(1)	553.4(1)	553.4	544.1
C' (MHz)	417.3(1)	417.5(1)	417.4	412.1
ΔI' (uÅ^2)	-1.741	-2.648	-2.18	-2.36
Origin (cm^{-1})	30532.245(1)	30532.434(1)	30532.340(1)	
# lines	141	458		
OMC (MHz)	4.10	5.03		
$\Delta E_{AB} = (E_{B'} - E_{A'}) - (E_{B''} - E_{A''})$	5673(30) MHz			

[a]Determined by averaging the measured values of σ = 0 and σ = 1 (columns 2 and 3).

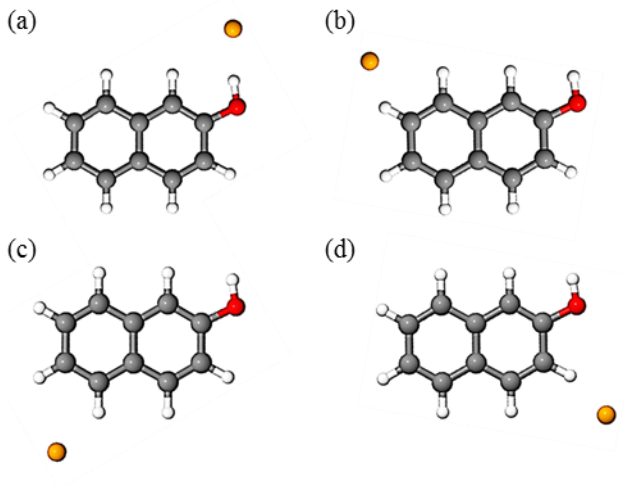

Figure 4-3. Possible locations of the water COM from a Kraitchman's analysis in the ground state of *cis*-2HNW. Water is shown in orange as a point mass. These locations were determined using inertial parameters of *cis*-2HN (Ref. 6) and *cis*-2HNW from this rotationally resolved work.

Table 4-2. Absolute position of water treated as a point mass of 18 atomic mass units (u). The inertial frames of *cis*-2HN (dashed axes) and *cis*-2HNW (solid axes) are shown in Fig. 4-1. All values are in Angstroms (Å).

	cis-2HN frame	*cis*-2HNW frame
S_0		
$\|a''\|$	3.77(2)	4.24(2)
$\|b''\|$	3.49(2)	1.70(2)
$\|c''\|$	0.38(2)	0.14(2)
r''	5.15(2)	4.58(2)
S_1		
$\|a'\|$	3.68(2)	4.18(2)
$\|b'\|$	3.49(2)	1.72(2)
$\|c'\|$	0.36(2)	0.13(2)
r'	5.11(2)	4.52(2)

2HN in both electronic states. The location shown in Fig. 4-3(a) is most likely, since it allows for water to act as a HB acceptor, and the –OH group of *cis*-2HN to act as a HB donor.

The second piece of information is the orientation of the water molecule in the complex. In a perfectly planar, vibrationless system, the measured inertial defect ($\Delta I = I_c - I_b - I_a$) would be zero. In Table 4-1, the ΔI value of each origin band, in S_0 and S_1, is small, but not zero [$\Delta I'' = -2.19$ (S_0) and $\Delta I' = -2.18$ uÅ^2 (S_1)]. If the oxygen of water lies in the *cis*-2HN plane, and the two hydrogen atoms of water lie in a plane perpendicular to this, the inertial defect of the complex would be $\Delta I_{calc} = -2.32$ uÅ^2, nearly matching the inertial defect we observe. We therefore conclude that, as in phenol-H_2O, the *ab* plane of water is nearly perpendicular to the *ab* plane of *cis*-2HN in the *cis*-2HNW complex.

The third piece of information is the HB orientation. Two possible orientations were considered; a bifurcated HB with water, and a HB with only a single lone pair of electrons from water. Geometry optimizations using M05-2X hybrid DFT and the 6-31+G* basis set were done, beginning with each of the two mentioned HB orientations. They both converged to the structure shown in Fig. 4-1, in which the $O - H \cdots OH_2$ HB is of the *trans*-linear type, with a single lone pair of electrons on water accepting the 2HN hydrogen. This structure was further optimized using M05-2X with the aug-cc-pVDZ basis set, and these theoretical rotational constants are reported in Table 4-1. Agreement with experiment is excellent.

4.4.2 Water dynamics

In all of the above, we have used the "rigid-body" rotational constants listed in Table 4-1, and defined in the footnote thereto. But, as is apparent on re-examination of the data in this table, the inertial parameters obtained from the fit of the two subbands are not quite the same. The origin

of these differences is a coupling between the overall rotation of the complex and the internal motion of the attached water, expressed in the following "torsion" and "torsion-rotation" Hamiltonians of a planar molecule as

Equation 4-2

$$\widehat{H}_t = F\hat{\rho}^2 + \frac{V_2}{2}(1 - \cos 2\phi),$$

Equation 4-3

$$\widehat{H}_{tr} = FW_{v\sigma}^{(1)}\left(\hat{\rho}_a\hat{P}_a + \hat{\rho}_b\hat{P}_b\right) + FW_{v\sigma}^{(2)}\left(\hat{\rho}_a\hat{P}_a + \hat{\rho}_b\hat{P}_b\right)^2.$$

In what follows, we show that unique information about the water dynamics can be obtained from an analysis of these small perturbations.

In Eq. 4-3, σ is the index that labels the "torsional" states of the attached water molecule; σ = 0, 1, 2, … *etc*. These are distinguishable by their nuclear spin statistical weights; the A subband (σ = 0) has a statistical weight of 1, and the B subband (σ = 1) has a statistical weight of 3. For σ = 0 and σ = 1, the first-order term in $\widehat{H}_{tr}$ is zero, and the combination of $\widehat{H}_r$ and the second-order term of $\widehat{H}_{tr}$ results in the effective Hamiltonian shown in Eq. 4-4.

Equation 4-4

$$\widehat{H}_{r,\text{eff}} = A_{\text{eff}}\widehat{P}_a^2 + B_{\text{eff}}\widehat{P}_b^2 + C_{\text{eff}}\widehat{P}_c^2.$$

Here, the effective rotational constants are related to the "rigid-body" rotational constants of the complex (*A*, *B*, *C*) *via* Eq. 4-5,

Equation 4-5

$$A_{\text{eff}} = A + FW_{v\sigma}^{(2)}\hat{\rho}_a^2, \text{ etc.,}$$

Here, F is the internal rotor constant, and $W_{v\sigma}^{(2)}$ is the second-order perturbation coefficient arising from the interaction of the angular momentum of the internal rotor ($\hat{\rho}_a$) with the angular momentum of the entire complex ($\hat{P}_a$). The cross terms that result from $\left(\hat{\rho}_a\hat{P}_a + \hat{\rho}_b\hat{P}_b\right)^2$ are considered small and neglected.

The differences in the rotational constants of the A and B subbands are defined as ΔA_{eff}, *etc.* Using Table 4-1, we see that $\Delta A''_{eff}$ = -1.0 ± 0.1 MHz, and $\Delta A'_{eff}$ = -1.1 ± 0.1 MHz. Since the two ΔA_{eff}'s are the largest of the differences in the rotational constants of the A and B subbands, we conclude that the internal motion occurs about an axis that is parallel (or nearly parallel) to *a* in both states. The differences ΔB_{eff} and ΔC_{eff} are small (all ≤ 0.2 MHz, and equal within experimental error for both electronic states). Parenthetically, we note that the ΔC_{eff} values are positive in both electronic states, opposite in sign to the ΔA_{eff} and ΔB_{eff} values. Since Eq. 4-5 is cyclic in A_{eff}, B_{eff}, and C_{eff}, all of the differences in effective rotational constants between the subbands should have the same sign. The observation that they do not indicates the assumption of simple two-fold motion about *a* is not completely correct.[4] We will return to this point later.

In the high barrier limit, the unperturbed values of A should be the same for both subtorsional levels σ = 0 and σ = 1. Thus, the $W_{v\sigma}^{(2)}$ perturbation coefficients of the two levels (and the magnitudes of the barriers) in both electronic states may be determined from the observed difference in the experimental values ΔA_{eff} if the values of F and $\hat{\rho}_a$ are known. For

the ground state, we chose to fix F'' to the value for an isolated water molecule, rotating about its *b*-axis and making an angle $\alpha'' = 18.5°$ (M05-2X/aug-cc-pVDZ) with the *a*-axis of the complex, $F'' = 437.0$ GHz. The hydrogen bond has $\alpha'' = 63.5°$, and has a much larger projection onto *b* than *a*. Therefore, the choice of the C_2 axis of water for the 1D torsional axis is more consistent with experiment. Then, using the method of Herschbach[30] and available data tables,[31] the $W_{\nu\sigma}^{(2)}$ perturbation coefficients were varied until the experimentally observed ΔA_{eff} was reproduced, yielding the barrier height $V_2'' = 203$ cm^{-1} for the ground state.

A slightly different procedure was followed for S_1 since F and $\hat{\rho}_a$ were not known for this state. By varying the angle α' in the excited state, we can require that the calculated difference in the subtorsional band splitting ΔE_{AB} match the experimentally observed value of 5673 MHz (0.189 cm^{-1}). The variable α' was stepped by 0.1° from 0° to 90°. At each of these 900 points, a new value of the excited state $\Delta W_{\nu\sigma}^{(2)}$ was generated, along with new values of F' and ρ_a'. This procedure enabled 900 independent interpolations of the effective barrier height in S_1, s' ($s = V_2/F$). From s', V_2' was also calculated. From the 900 V_2' values, the torsional levels in both electronic states were calculated using the matrix elements of the torsional Hamiltonian (Eq. 4-2; *cf.* section 4.2 of Ref. 31) from which the ΔE_{AB} value was determined. Fig. 4-4 depicts ΔE_{AB} as a function of α'. Immediately evident is the crossing of $\Delta E_{AB}(\alpha')$ with the experimental value of 0.189 cm^{-1}. This occurs at $\alpha' = 30.6°$, when $F' = 436.8$ GHz. Through the use of tabulated effective barrier heights, along with knowledge of the internal rotor constant, we calculate an S_1 barrier height of $V_2' = 180$ cm^{-1}. The results of these calculations for both states are summarized in Table 4-3.

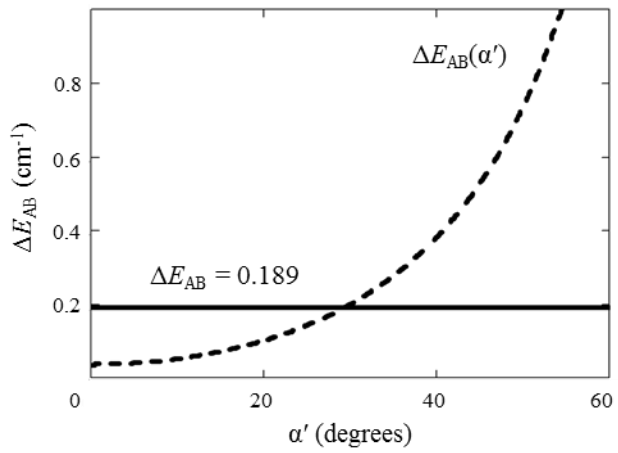

Figure 4-4. Difference in A-B subband splittings between S_1 and S_0 as a function of the S_1 internal motion axis angle, α′. Shown as a solid line is the measured splitting from the rotationally resolved spectrum of 0.189 cm^{-1} (5673 MHz). The crossing occurs at α′ = 30.6°, a change of +12.1° following excitation.

Table 4-3. Second-order torsion-rotation perturbation coefficients $W_{v\sigma}^{(2)}$, internal motion axis angles (α), effective barrier heights (*s*), barrier heights (V_2), and internal rotor constants (*F*) of *cis*-2HNW in each electronic state.

Parameter	S_0	S_1
$W_{00}^{(2)}$	0.080	0.122
$W_{01}^{(2)}$	-0.080	-0.122
α (°)	18.5[a]	30.6
s	13.9	12.3
V_2 (cm^{-1})	203	180
F (cm^{-1})	14.576	14.568

[a]From theory (M05-2X/aug-cc-pVDZ).

4.4.3 Permanent electric dipole moments

Figure 4-5 shows portions of the high resolution spectrum of *cis*-2HNW recorded at different electric field strengths ranging from 0 to 1184 V/cm. Immediately apparent is the additional splitting and/or broadening of the individual rovibronic transitions that is produced by the applied electric field, owing to a lifting of the $2J + 1$ spatial degeneracy of the total angular momentum *J*. These field-induced Stark effects were analyzed according to

Equation 4-6

$$\widehat{H}_{\text{stark}} = -\vec{\mu} \cdot \vec{E} = -E_Z \sum_{g=a,b,c} (\mu_g \lambda_{Zg}),$$

where E_z is the applied electric field strength, μ_g are the components of the permanent electric dipole moments of *cis-2*HNW in the S_0 and S_1 states, and the λ_{Zg} are the necessary direction cosines. In our application of Eq. 4-6, each subband was fit to the same values of μ_g; these are listed in Table 4-4. The best-fit magnitudes of μ are 4.00 D in S_0 and 4.66 D in S_1; thus, $|\mu|$ increases by ~ 16% upon excitation of *cis-2*HNW by light. The angle between μ and the *b*-axis of *cis-2*HNW changes from 51 to 61°.

4.5 DISCUSSION

The advantage of using a 1D model to describe the motion of the water molecule relative to *cis*-2HN is the ease with which barrier heights can be derived from experimental data. However, the true potential energy surface (PES) governing this motion is multi-dimensional, with a coupling

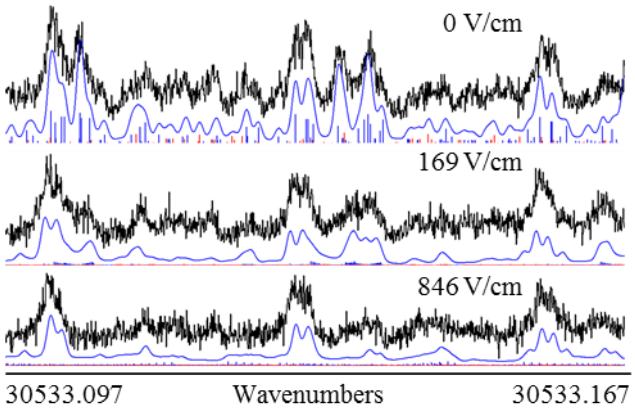

Figure 4-5. Stark spectra of *cis*-2HNW at full rotational resolution. Each simulation is a sum of A and B sub-band contributions. All simulations were done using the inertial parameters in Table 4-1 and the dipole moments in Table 4-4.

Table 4-4. Absolute permanent electric dipole moments of 2HN and 2HN acid-base complexes. The EDMs are shown as projections onto the inertial axes of each molecule or complex. Experimental uncertainty is shown in parenthesis, and is in the last digit. All values are in Debye (D).

	trans-2HN[a,b]	*cis*-2HN[c]	*cis*-2HNA[c]	*cis*-2HNW[a]
S_0				
$\|\mu_a\|$	0.384(2)	0.344(3)	2.56(2)	3.11(5)
$\|\mu_b\|$	1.310(8)	0.951(8)	2.93(4)	2.51(5)
μ	1.36(1)	1.011(9)	3.89(4)	4.00(5)
S_1				
$\|\mu_a\|$	1.028(2)	0.159(3)	3.76(2)	4.09(5)
$\|\mu_b\|$	1.01(1)	1.160(8)	3.21(3)	2.23(5)
μ	1.44(1)	1.17(1)	4.94(4)	4.66(6)

[a]This work.
[b]See supplementary material for previously unpublished data (Ref. 48).
[c]Ref. 10.

between torsion about the HB and a low frequency intermolecular wagging mode making the largest contributions. A combination of the two modes is required to successfully exchange the hydrogen atoms of water, as depicted in Fig. 4-6. The water PES also governs the motion of the water dipole with respect to *cis-2*HN, the time-averaged orientation of which influences the measured S_0 and S_1 permanent dipole moments of the complex. With this in mind, we begin this section with a complete structural analysis from experiment, followed by a comparison of the 1D model with other multidimensional models, and close with a discussion of the contribution of water motion to the measured permanent electric dipole moments. In the final section, theoretical energy and dipole decompositions provide valuable insight into the nature of the HB in the ground electronic state.

4.5.1 S_0 and S_1 structures of *cis*-2HNW

Decreases in rotational constants upon excitation in aromatic systems are often due to increases in bond lengths between ring carbons, owing to the promotion of an electron into an anti-bonding π^* orbital. Table 4-5 clearly shows this to be the case for naphthalene[32] and *cis*-2HN,[6] as all changes in rotational constants are negative. However, in both the NH_3 and H_2O complexes of *cis*-2HN, the ΔA values are smaller in magnitude than those of bare *cis*-2HN, indicative of HB contraction upon excitation. This contraction is enough to actually reverse the sign of ΔB in the monosolvated complexes. Table 4-2 quantifies the above observation. The absolute *a* position of water changes a small but significant -0.09 Å. (The accuracy of each absolute coordinate is limited by the rotational constants to a standard deviation of ± 0.02 Å.) However, we see that Δb= 0.00 Å, indicating that the movement along *b* is less than 0.02 Å. The change in distance *r* between the COM of *cis*-2HN and H_2O is -0.04 Å (5.15 Å in S_0, 5.11 Å in S_1).

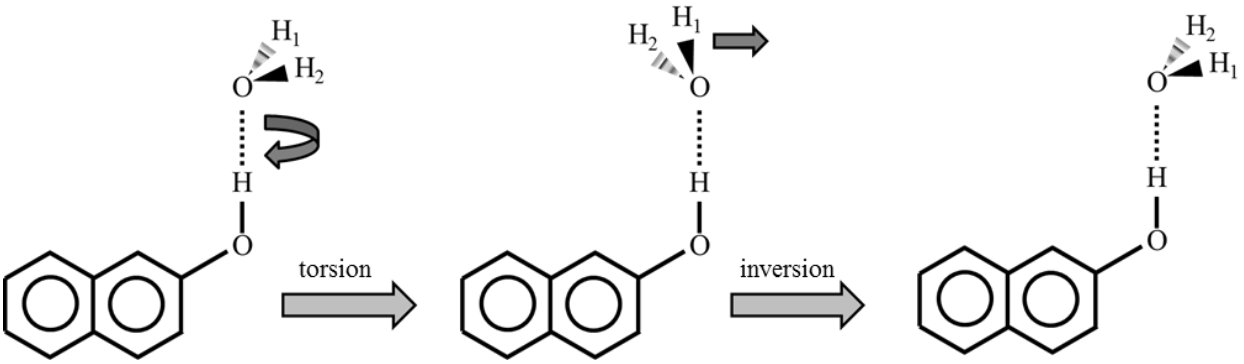

Figure 4-6. Illustration of coupled torsion-inversion intermolecular motion in *cis*-2HNW which results in an exchange of H_1 and H_2.

Table 4-5. Change in rotational constants following excitation to S_1 in naphthalene ring systems. The values of *cis*-2HNW were derived using the structural constants listed in Table 4-1.

	Naphthalene[a]	*cis*-2HN[b]	*cis*-2HNA[c]	*cis*-2HNW
ΔA (MHz)	-77.5	-80.2	-43.9	-38.5
ΔB (MHz)	-18.8	-2.9	+8.8	+5.3
ΔC (MHz)	-15.9	-5.8	+2.7	+0.7

[a]Parent molecule, Ref. 32.

[b]Bare *cis*-2-naphthol, Ref. 6.

[c]Ammonia complex of *cis*-2HN, Ref. 36.

It is more chemically relevant to discuss the light-induced change in HB distance between *cis*-2HN and H_2O. By comparison with the previously reported position of the hydroxyl hydrogen (S_0: $a_H = 3.44$, $b_H = 1.56$ Å; S_1: $a_H = 3.36$, $b_H = 1.60$ Å),[6] we estimate the $O-H\cdots OH_2$ distance to be 1.96 Å in S_0 and 1.92 Å in S_1. This reduction in HB length of 0.04 Å is similar to that predicted by high level *ab initio* calculations (0.07 Å in *cis*-2HNW).[7] The increase in the O–H bond length in bare 2HN and the decrease in the heavy atom separation in the $O-H\cdots OH_2$ HB upon excitation is consistent with the observed behavior of other photoacids in condensed phase environments.[33]

Table 4-2 also reveals a subtle yet important piece of information. The out-of-plane coordinate |*c*| of the water molecule is not zero in either electronic state. The experimental values are c = 0.38 Å in S_0 and c = 0.36 Å in S_1. Schütz *et al.*[27] have calculated the transition state geometry for water motion in the 2HNW ground state using *ab initio* methods. Their calculation predicts a transition state in which the O atom of water lies ~ 0.4 Å above the 2HN plane, with the water hydrogens rotated at a torsional angle of ϕ = 95° (*cf.* Fig. 4 of Ref. 27). This optimized transition state is associated with a coupled internal water motion, involving rotation about the $O-H\cdots OH_2$ hydrogen bond and the lowest energy intermolecular wag mode (β_1).[27] Non-zero values of |*c*| also were observed in the indole-H_2O complex.[34] Thus, it appears that these motions also influence the structure of both complexes in the zero-point vibrational levels of their two electronic states. Comparatively, our QST pathway predicts a nearly planar transition state.

The *ab initio* work of Schütz *et al.*[27] theorized a ground state barrier height of 247 cm^{-1}, 218 cm^{-1} when corrected for zero-point vibrational energy (ZPE). This calculated value, which takes into account anharmonic coupling between torsional motion and the wag mode, is in good agreement with our experimental value of 203 cm^{-1}. The derived barrier heights from the high

resolution spectrum of phenol-water,[4] using the 1D analysis, are $V_2'' = 177$ and $V_2' = 127$ cm^{-1}. Jacoby and Schmitt[35] have suggested that the decrease in V_2 upon excitation observed in phenol-H_2O arises from the loss of the second $C-H\cdots OH_2$ HB. This hypothesis appears consistent with the data presented here on *cis*-2HNW ($V_2' = 180$ cm^{-1}), as well as a subtle photoinduced change in α (α'' = 18.5, α' = 30.6°) that may result from a less favorable secondary interaction between H_2O and the naphthalene ring. The optimization in Fig. 4-1 also suggests the existence of a second, weak HB between the second oxygen lone pair and the aromatic hydrogen attached to position 1 of the naphthalene ring. The two HB lengths in Fig. 4-1 are predicted by theory to be 1.89 Å and 2.74 Å, respectively

Jacoby and Schmitt[35] have developed a program (called HTORFIT) in which "best fit" values of F and V_n for 1:1 complexes are determined using all available vibrationally and rotationally resolved experimental data. From a global fit of all experimental data, they find that $V_2'' = 175.4(13)$ cm^{-1} and $V_2' = 109.1(2)$ cm^{-1} for phenol-H_2O. A significant reduction in F upon excitation was reported, from F'' = 14.813(118) cm^{-1} to F' = 13.415(25) cm^{-1}, attributed to the movement of a neutral hydrogen atom from phenol towards H_2O upon excitation. To the best of our knowledge, no vibrationally resolved experiment has been able to identify transitions of purely torsional origin in the *cis*-2HNW spectrum (a single tentative assignment was made for *trans*-2HNW in Ref. 33), thus making a global analysis impossible in this case. Using the V_2 and F values from this work, we have predicted the energies for purely torsional transitions in *cis*-2HNW, relative to the electronic origin; these are collected in Table 4-6.

We find little change in F upon excitation for *cis*-2HNW (F'' = 14.576 and F' = 14.568 cm^{-1}), consistent with the findings from the *trans*-1HN-NH_3 (*trans*-1HNA) and *trans*-2HNA complexes studied using HTORFIT,[35] as well as *cis*-1HNA and *cis*-2HNA studied by high

resolution spectroscopy.[36] This shows that the axis of motion relative to water does not change when the photon is absorbed. A significant decrease in *F* was observed in phenol-NH_3 and -H_2O complexes, interpreted as due to the translocation of a neutral hydrogen radical from phenol to its HB partner upon excitation. This explains the measured decrease in the fluorescence lifetime of the phenol-H_2O complex compared to the bare chromophore, something not observed in *cis*-2HNW. A charge transfer model seems more appropriate in this case. The loss of fractional electronic charge from a non-bonding orbital of the attached water would not greatly affect the measured *F*, unlike the translocation of neutral hydrogen and placement of a full electron into an unoccupied partner orbital.

Table 4-6. Predicted energies of S_1 torsional levels relative to the electronic origin ($S_1 \leftarrow S_0$) of *cis*-2HNW. Transitions are listed using $|v',\sigma'\rangle \leftarrow |v'',\sigma''\rangle$ notation.

Transition	Predicted Relative Energy
$\|2,0\rangle \leftarrow \|0,0\rangle$	+ 130 cm^{-1}
$\|2,1\rangle \leftarrow \|0,1\rangle$	+ 175 cm^{-1}
$\|4,0\rangle \leftarrow \|0,0\rangle$	+ 279 cm^{-1}
$\|4,1\rangle \leftarrow \|0,1\rangle$	+ 407 cm^{-1}

4.5.2 Permanent electric dipole moments

In the condensed phase, aromatic alcohols like β-naphthol exhibit a red shifted fluorescence due to the donation of a proton to the bulk. The electronic origin band of the S_1-S_0 transition of *cis*-2HNW also is red shifted relative to the corresponding origin of the bare molecule by 371 cm^{-1}. Through the measurement of permanent state-specific gas phase EDMs, we aim to understand

the motion of charge within a single HB along the acid-base reaction coordinate, void of bulk solvent influences. The total dipole moment of these complexes is a mix of electronic contributions from the monomer units, induced moments, and charge transfer, whose decomposition is theoretically challenging.

We have previously introduced a simple static vector model to interpret the composition of complex dipole moments.[10,37] The static vector model builds on the predictive success of vector addition models in covalently bound, disubstituted, benzene rings.[38] In the *cis*-2HNA complex, it was necessary to include four terms in the model; acid (2HN), base (NH_3), induced (ind), and charge transfer (CT) components, according to the following (vector) equation:

Equation 4-7

$$\vec{\mu}_{c2\mathrm{HNA}} = \vec{\mu}_{c2\mathrm{HN}} + \vec{\mu}_{\mathrm{NH_3}} + \vec{\mu}_{\mathrm{ind}} + \vec{\mu}_{\mathrm{CT}}.$$

Comparison of the measured (and calculated) values of these quantities led to the conclusion that a significant amount of charge is transferred from NH_3 to 2HN in both electronic states, Q = 0.09 e in S_0 and Q^* = 0.14 e in S_1. The increase in electron transfer upon excitation by light, while small (~ 0.05 e), is sufficient to quantitatively account for the redshift of the spectrum of the complex relative to the bare molecule, ~ 585 cm^{-1} in this case, thus validating the vector addition model.

A similar model should also apply to *cis*-2HNW. However, there is an interesting complication in this case. The axis about which the H_2O is moving in *cis*-2HNW is not the hydrogen bond axis, as it is in *cis*-2HNA. Thus, the relative dipole orientation changes during

the motion, necessitating a dynamic rather than static vector model. A 1D treatment of our experimental data, using the model of Harmony,[39]

Equation 4-8

$$\nu_t = 2\,(E_0^1 - E_0^0)/h,$$

suggests a tunneling time of $\tau'' = 37$ psec in the ground state, and $\tau' = 25$ psec in the excited state. Flickering dipoles produced on this timescale by the large angular jumps in water orientation should be of interest in THz measurements of bulk water dynamics.[40] Since these times are less than those associated with overall molecular rotation, a time-averaged distribution of the water dipole orientation results.

As noted, the barrier to water motion in *cis*-2HNW is near 200 cm^{-1} in both electronic states. Thus, at temperatures less than this, the water molecule tunnels through the barrier separating the two equivalent HB configurations, leading to a time-varying electric field produced by the reorienting water dipole. The flickering dipoles that result are analogous to those produced by HB switching in liquid water,[41] although the PES governing the latter motion is very different. In what follows, the time-varying dipole field generated by the moving water molecule in *cis*-2HNW is analyzed in order to assess its contribution to the measured dipole of the complex in both electronic states.

The theoretical pathway of water motion in the ground S_0 electronic state of the complex has been calculated using the QST method available in G03. Nine structures along the optimized path resulting in an exchange of water hydrogen atoms were calculated at the HF level, using the

6-31+G* basis set. The energies of these structures were plotted *versus* an effective motion coordinate, and fit to an expansion of torsional potential functions according to the equation

Equation 4-9

$$V(\phi) = \sum_n \frac{V_n}{2}(1 - \cos n\phi) + C.$$

A satisfactory fit (standard deviation < 1 cm^{-1}) of the QST energies was found using the following coefficients; V_2 = 239, V_4 = -27, V_6 = -9, V_8 = 6, and V_{10} = 2 cm^{-1}. The addition of higher order potential terms (V_4, V_6, *etc*.) widens the potential wells, rendering the calculated barrier easier to cross than a simple V_2 potential. Torsional wavefunctions $\psi(\phi)$, which provide information on the probability of the rotor being at a given point along the potential, were then constructed from the theoretical potential surface using a basis set of 50 free rotor wavefunctions. (The sum of the coefficients squared in this linear combination was normalized to one.) Finally, the expectation value of the dipole moment of water in the 2HN plane, as governed by the potential surface for internal motion, was then calculated using Eq. 4-10:

Equation 4-10

$$\langle \mu_{H_2O} \rangle = \int_0^{2\pi} \psi^*(\phi)\mu(\phi)\psi(\phi)d\phi.$$

In this way, we account for the fact that the motion of the water molecule is controlled by the potential, which in turn influences the time-averaged value of its dipole moment.

Figure 4-7(a) shows the value of the projection of the water dipole moment on the naphthol plane, with ϕ = 0 being defined as the equilibrium configuration. This projection

varies by ~ 0.2 D over the course of its motion. Figure 4-7(b) shows the expectation value of the in-plane water dipole at 22.5° intervals in ϕ, weighted according to the relative probability of different possible water orientations dictated by the potential in Eq. 4-9. This curve reflects the shape of the potential governing the motion of the water molecule. Thus, contributions to the expectation value are largest in energetically favored orientations of the dipole, and smallest in unfavored orientations. Notice that the curve in Fig. 4-7(b) does not reach a smooth minimum under the barrier. Instead, there is an increase in the contribution to the dipole moment within the barrier, owing to inversion of the water lone pairs.[42] The expectation value of the water dipole over the entire internal motion is 1.78 D, and completely contained in the *ab* plane of naphthol. [The sum of all "X" values in Fig. 4-7(b) also is 1.78 D.] This type of precession was not observed in *cis*-2HNA, as the dipole of NH_3 coincides with the internal rotation axis. This makes the path of internal motion and its PES interesting for two reasons, as experimental data on the structures and EDMs of the complex are now available.

Replacing the water dipole vector in Eq. 4-7 with the calculated $\langle \mu_{H_2O} \rangle$ from Eq. 4-10 should provide an estimate of the red shift of 2HN fluorescence in the presence of a single water molecule. However, the projection of $\vec{\mu}_{CT}$ onto the HB axis is small in the S_1 state (Fig. 4-8), resulting in $Q^* < Q$, which leads to a predicted blue shift of 46 cm^{-1} (see supplementary material in Appendix C), markedly different than the experimentally observed red shift of 371 cm^{-1}. The orientation of $\vec{\mu}_{CT}$ in the excited state of *cis*-2HNW is instead angled more towards the naphthalene ring. In contrast, the orientation of $\vec{\mu}_{CT}$ in *cis*-2HNA is directed along the HB axis. This change in orientation may be due to the charge-donating molecular orbital of H_2O having a better overlap (both energetically and spatially) with a more delocalized charge-accepting orbital

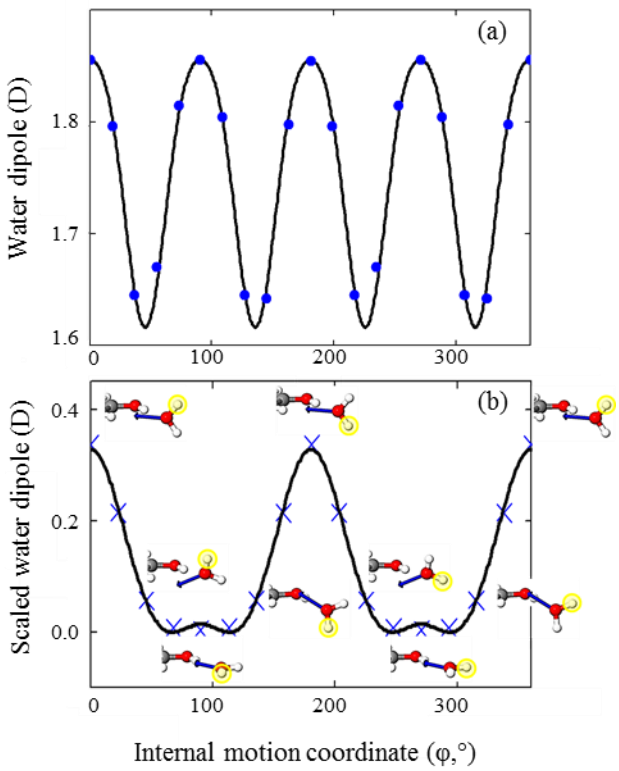

Figure 4-7. (a) Dipole moment function of water calculated using the quadratic synchronous transit (QST) method. Blue dots are the 2HN-plane dipole projections of water from point structures. The black trace is a fit of these blue points to an expansion of torsion functions, with the following coefficients; V_4 = -0.239, V_8 = 0.0340, and C = 1.855. (b) Dipole moment function scaled by the probability of water taking on a given orientation as calculated using the QST method and a basis set of free rotor wavefunctions. The black trace is a fit to the data points using the following coefficients: V_2 = 0.157, V_4 = 0.058, V_8 = 0.00146, and C = -0.104. An image of the water dipole precession during internal motion is shown every 45°.

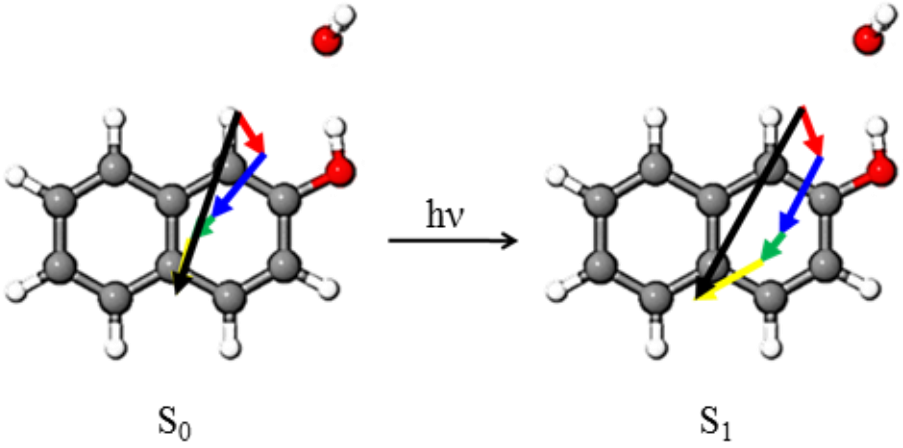

Figure 4-8. The S_0 and S_1 dipole moments of *cis*-2HNW. This figure illustrates the components of Eq. 4-7, where μ_{c2HN} (red), $\langle\mu_{H_2O}\rangle$ (blue), μ_{ind} (green), and μ_{CT} (yellow) add to reproduce μ_{c2HNW} (black).

of 2HN. Although an experimental value of Q^* for *cis*-2HNW is absent, we can still comment on the trends in the dipole moments of 2HN complexes. In the ground state, $|\vec{\mu}_{c2\mathrm{HNW}}| > |\vec{\mu}_{c2\mathrm{HNA}}|$ (4.00 D *vs.* 3.89 D, see Table 4-4). This difference arises from the difference in HB partner dipole moments, which leads to larger electrostatic and induced dipole terms (the quadrupole moment of H_2O also is larger than that of NH_3) for 2HNW than were found in 2HNA, accounting for the difference in magnitude of the ground state dipoles.

Clear differences in the S_1 EDMs of the complexes indicate that the more basic NH_3 induces more charge transfer upon electronic excitation than H_2O. In the S_1 state, $|\vec{\mu}_{c2\mathrm{HNW}}| < |\vec{\mu}_{c2\mathrm{HNA}}|$. Our experimental evidence suggests that NH_3 does a better job of stabilizing the excited state charge transfer reaction than H_2O, leading to an increase in the photoacidic behavior of β-naphthol in the gas phase.

4.5.3 Energy and dipole decomposition analysis

Vector models are only an approximation of the true electronic behavior of acid-base complexes in the gas phase. They rely heavily on the convergence of the molecular multipole expansions at close distances, *ab initio* molecular polarizabilities, and on the treatment of CT as localized in the HB. For this reason, a high-level theoretical treatment of the acid-base interaction in the electronic ground state has been made *via* a block-localized wavefunction energy and dipole decomposition analysis (BLW-ED),[43] which can be performed both using wave functional theory (WFT) and density functional theory (DFT).[44,45] The BLW-ED method has been applied to a variety of systems,[43-45] including Lewis acid-base complexes.[46] The energy decomposition was performed with the BLDFT method using the XMVB program[24] and a modified version of

GAMESS.[25,45] These calculations, while not yet accounting for the flickering electric field arising from water internal motion, do vastly improve upon the other issues mentioned above. The dipole moment decomposition of *cis*-2HNA and *cis*-2HNW is discussed below.

Table 4-7 shows the interaction energy components performed at the B3LYP level for *cis*-2HNA and *cis*-2HNW:

Equation 4-11

$$\Delta E_{\text{int}} = \Delta E_r + \Delta E_{\text{stat}} + \Delta E_{\text{pol}} + \Delta E_{\text{CT}}.$$

Here, the total interaction energy ΔE_{int} is decomposed into the four terms on the right-hand side of the equation, which are described as follows.[43-45] ΔE_r is the energy penalty due to the change in monomer geometries in the complex with respect to their isolated relaxed geometry. The remaining three energy terms are determined using the monomer geometries in the complex. First, we constructed a block-localized configuration for the molecular complex **AB** in which Kohn-Sham orbitals are strictly localized within each individual monomer fragment, and the block-localized determinantal wave function is written as $\Psi^{o}_{\text{BLDFT}} = \hat{A}\{\Phi^{o}_{\text{A}}\Phi^{o}_{\text{B}}\}$, where Φ^{o}_{A} and Φ^{o}_{B} are successive products of the optimized Kohn-Sham orbitals for the isolated monomers **A** and **B**, and $\hat{A}$ is an antisymmetrization operator. The static electrostatic interaction energy, ΔE_{stat}, is the sum of the Coulomb and exchange repulsion energies, and is determined as the energy difference between the block-localized complex configuration and the sum of the monomers:

Table 4-7. Block-localized wavefunction energy decomposition. All values are in wavenumbers (cm^{-1}).

	B3LYP/6-31+G*		B3LYP/aug-cc-pVDZ	
	cis-2HNA	*cis*-2HNW	*cis*-2HNA	*cis*-2HNW
ΔE_r	+410	+310	+410	+300
ΔE_{stat}	-750	-980	+270	-190
ΔE_{pol}	-1000	-600	-1290	-730
ΔE_{CT}	-1300	-620	-1760	-1010
ΔE_{int}	-2640	-1890	-2370	-1630

Equation 4-12

$$\Delta E_{\text{stat}} = E[\rho^{\text{o}}_{\text{BLDFT}}(AB)] - \{E_{\text{DFT}}[\rho^{\text{o}}(A)] + E_{\text{DFT}}[\rho^{\text{o}}(B)]\}.$$

Here, $\rho^{\text{o}}_{\text{BLDFT}}(\text{AB})$, $\rho^{o}(\text{A})$, and $\rho^{o}(\text{B})$ are the electron densities for the species specified in parentheses, and the superscript "o" indicates that the corresponding Kohn-Sham orbitals in the corresponding wave functions, $\Psi^{\text{o}}_{\text{BLDFT}}$, $\Psi^{o}(\text{A}) = \hat{A}\{\Phi^{\text{o}}_{\text{A}}\}$, and $\Psi^{o}(\text{B}) = \hat{A}\{\Phi^{\text{o}}_{\text{B}}\}$ are optimized for the isolated monomers. ΔE_{stat} corresponds to the energy change produced by bringing two infinitely separated monomers into contact at the complex geometry, but keeping their electron densities unchanged. Thus, neither polarization nor CT is included in ΔE_{stat}.

Next, we allowed the charge densities of the monomer blocks in $\Psi^{\text{o}}_{\text{BLDFT}}$ to be mutually polarized by the electric field of the other fragment. The change in interaction energy in this process is the polarization contribution:

Equation 4-13

$$\Delta E_{\text{pol}} = E[\rho_{\text{BLDFT}}(AB)] - E[\rho^{\text{o}}_{\text{BLDFT}}(AB)],$$

where $\rho_{\text{BLDFT}}(\text{AB})$ is obtained from the variationally optimized block-localized Kohn-Sham determinant $\Psi_{\text{BLDFT}} = \hat{A}\{\Phi_{\text{A}}\Phi_{\text{B}}\}$. Finally, we expanded the molecular orbitals from the monomer block-localization into the complex space such that the Kohn-Sham orbitals are fully delocalized, and in the process, we introduced the basis-set superposition error (BSSE) correction, which is also due to the expansion of the basis space. The basis set expansion accounts for charge

migration from a dominantly one-monomer region into the other, and the energy change in this process is the CT component in the total interaction energy:

Equation 4-14

$$\Delta E_{\mathrm{CT}} = E[\rho_{\mathrm{DFT}}(AB)] - E[\rho_{\mathrm{BLDFT}}(AB)],$$

where the electron density $\rho_{\mathrm{DFT}}(\mathrm{AB})$ is computed using standard DFT with the fully delocalized determinant function $\Psi_{\mathrm{DFT}}(\mathrm{AB}) = \hat{A}\{\Phi_{\mathrm{AB}}\}$. In Eq. 4-12 – 4-14, we have used the subscripts "BLDFT" and "DFT" to indicate that the electron density of the complex is either block-localized or delocalized, respectively.

The major contribution to the interaction energy is due to CT between the two fragments, followed by polarization energy, while electrostatic and geometry distortions provide smaller contributions. In both *cis*-2HNA and *cis*-2HNW, ΔE_{CT} makes the largest contribution to ΔE_{int}, revealing that CT is the greatest stabilizing force upon complex formation in the ground state S_0. However, the more basic NH_3 yields a ΔE_{CT} nearly twice as large as that of H_2O, indicating that ammonia is a better HB acceptor with more significant covalent character than water. In both calculations using different basis sets, H_2O results in a more negative ΔE_{stat}, a reflection of the larger intrinsic dipole moment of water than ammonia (1.855 *vs.* 1.427 D). On the other hand, NH_3 appears to be more polarizable, and induces almost double the polarization energy ΔE_{pol} than H_2O, using both basis sets. Overall, NH_3 is able to form a more stable complex with *cis*-2HN than H_2O, owing to almost double the stabilization from polarization and CT than is observed in the *cis*-2HNW complex. The differences between NH_3 and H_2O polarization and CT can be also visually appreciated from Fig. 4-9, where it is apparent that the 2HNA system shows

larger changes in electron density than 2HNW. These differences are clearly of a localized nature in the ground electronic state.

The ability to strictly block-localize and variationally optimize the Kohn-Sham orbitals in BLDFT calculations allows us to decompose the total dipole moment of the complex into specific components corresponding to the physical processes outlined in the energy decomposition analysis. The computational results are listed in Table 4-8. In the first two rows, the "o" subscript means that the dipole moments were computed at the geometries of the individually optimized fragments (geometries optimized at the M06-2X/6-31+G* level), while the following two rows report the change in the dipoles of the isolated fragments in the geometry that they assume in the complex. In Table 4-8, μ_{stat} is the dipole moment for the complex with the block-localized Kohn-Sham determinantal function computed using the orbitals of the isolated fragments at infinite separation. The charge density $\rho_{\mathrm{BLDFT}}(\mathrm{AB})$ yields $\Delta\mu_{pol}$, which is the polarization contribution to the total dipole moment of the complex after the block-localized orbitals are allowed to relax in the presence of the other subgroups. Finally, $\Delta\mu_{CT}$ is the change in dipole moment of the complex in going from the block-localized state into the fully delocalized complex configuration. Each total $\mu_{complex}$ reported in Table 4-8 compares favorably with the corresponding experimentally measured value in Table 4-4.

Table 4-8 shows that the main contribution to the total dipole moment comes from μ_{stat}, which is about 60% of the total dipole moment of each complex and is already present before any relaxation of the block-localized orbitals takes place. Although charge reorganization does not take place in the $\Psi^{\mathrm{o}}_{\mathrm{BLDFT}} = \hat{A}\left\{\Phi^{\mathrm{o}}_{\mathrm{A}}\Phi^{\mathrm{o}}_{\mathrm{B}}\right\}$ determinant, exchange polarization due to the Pauli

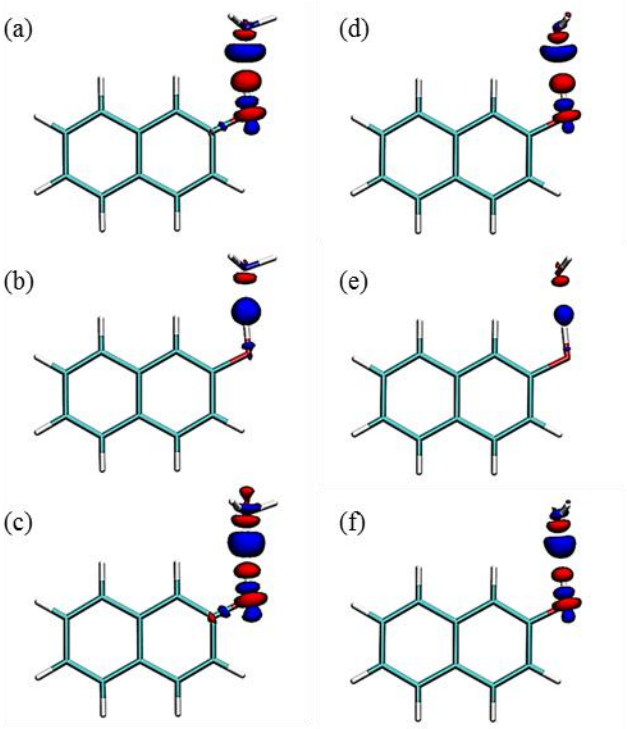

Figure 4-9. B3LYP/aug-cc-pVDZ electron density difference contours of 2HNA (a)-(c) and 2HNW (d)-(f). The polarization effect is shown in (a) and (d), the charge transfer in (b) and (e), while (c) and (f) show the combined effect. The same isodensity value (0.003) is used for all the plots, and the colors blue and red represent gains and losses in electron density, respectively.

Table 4-8. Block-localized wavefunction dipole decomposition. All values are in Debye (D).

	B3LYP/6-31+G*		B3LYP/aug-cc-pVDZ	
	cis-2HNA	*cis*-2HNW	*cis*-2HNA	*cis*-2HNW
$\mu_{2HN,o}$	1.11	1.11	1.00	1.00
$\mu_{solvent,o}$	1.83	2.24	1.47	1.84
$\Delta\mu_{2HN}$	0.02	0.01	0.04	0.01
$\Delta\mu_{solvent}$	0.02	-0.01	0.02	-0.01
μ_{stat}	2.92	3.00	2.51	2.61
$\Delta\mu_{pol}$	1.05	1.15	1.23	1.21
$\Delta\mu_{CT}$	0.29	0.10	0.35	0.23
$\mu_{complex}$	4.26	4.25	4.09	4.05

principle is accounted for. It is interesting to note that μ_{stat} is roughly the sum of the dipole moments of the individual monomers in *cis*-2HNA, along with a slight variation due to geometric distortion to form the complex. However, a non-negligible exchange polarization effect of -0.23 D using the aug-cc-pVDZ basis is found in the *cis*-2HNW complex. Another substantial contribution arises from the polarization of the block-localized orbitals, while CT accounts only for a small amount of the total dipole moment. A remarkable finding is that while CT effects show greater energy contributions than polarization to complex formation, the internal charge reorganization mutually induced by the presence of the other interacting monomer has a greater impact on the computed molecular dipole. Generally, following the μ_{stat} and $\Delta\mu_{pol}$ terms, the *cis*-2HNW dipole is larger than that of *cis*-2HNA, consistent with the larger dipole moment of H_2O. The CT component is larger in *cis*-2HNA, producing total theoretical dipole moments that are nearly identical for both complexes. The theoretical block-localized decomposition supports the hypothesis that CT is of greater importance in *cis*-2HNA than in *cis*-2HNW, analogous to previous studies of phenol-NH_3 and –H_2O.[47]

Table 4-8 reveals that $\Delta\mu_{CT}$ is by far the smallest component of the total complex dipole in both *cis*-2HNA and *cis*-2HNW. In both complexes, the order of dipole moment magnitude is $\mu_{stat} > \Delta\mu_{pol} > \Delta\mu_{CT}$. The major contribution of μ_{stat} in both complexes, along with the major contribution of ΔE_{CT} mentioned above, paints a picture of localized CT. Simultaneously solving the classical equations for energy and dipole moment arising from two point charges Q separated by a distance d results in Q = 0.10 electrons over d = 0.70 Å for *cis*-2HNA, and Q = 0.07 electrons over d = 0.64 Å for *cis*-2HNW (aug-cc-pVDZ results).

4.6 CONCLUSION

High resolution electronic spectra of β-naphthol and 1:1 β-naphthol acid-base complexes have been thoroughly explored, in the presence and absence of an external electric field. We show that in bare 2HN, the EDM reorientation upon photoexcitation indicates a loss of electron density from oxygen, rendering the hydroxyl hydrogen more acidic in the excited S_1 state [see the supplementary material[48] in Appendix C and Ref. 10]. Matsumoto, Ebata, and Mikami[9] have reported a red shift of ν_{OH} in S_1 of β-naphthol-H_2O which is greater than that observed in the ground S_0 state, consistent with a weakening of the O-H bond in *cis*-2HN following excitation. The EDMs reported here when the basic water is hydrogen bonded to this acidic hydrogen are large, and the inclusion of charge transfer in the dipole decomposition is necessary. Experimental determinations of charge transfer can be quantified if the water internal motion is taken into account. DFT energy and dipole decomposition using a block-localized wavefunction approach support the hypothesis of localized charge transfer in these systems. We conclude that, as in *cis*-2HNA, charge transfer is a local phenomenon involving the acid and the base, and that H_2O is less efficient than NH_3 at promoting the photoacidic behavior of 2HN. This is in part a consequence of the large amplitude motion of H_2O, which was not observed in *cis*-2HNA. In the gas phase, as in liquid water, large angular jumps associated with water HB dynamics produce "flickering dipoles", a non-uniform evolution of the water dipole in time.

Unanswered questions about hydrogen bonded systems of 2HN still remain. Recently, theoretical work has elegantly explained the strange R2PI spectra of doubly-hydrated 2HN and phenol.[7,49] High resolution spectra of the sharp features observed in these experiments would provide the structure in S_0 and S_1 of these three-bodied clusters, as well as their associated electronic properties. Since these structures are expected to involve π hydrogen bonds, the

energetics of which have recently have been quantified using the high resolution technique,[50] new information on weak and strong solvation effects could be measured. The movement of charge towards the *ortho* carbon in 2HN reported here is evidence that π hydrogen bonding at this site is stronger in S_1, explaining the greater relative stability of the non-cyclic doubly-hydrated structures already proposed.[7]

4.7 ACKNOWLEDGEMENTS

We acknowledge the help of Philip J. Morgan during the *trans*-2HN experiments, David F. Plusquellic for JB95 fitting program updates, and the National Science Foundation (NSF) for funding (CHE-0911117). A.J.F. also acknowledges support from the Andrew Mellon Predoctoral Fellowship Program at the University of Pittsburgh.

4.8 REFERENCES

1. H. Abe, N. Mikami, and M. Ito, *J. Phys. Chem.* **86**, 1768 (1982).

2. K. Fuke and K. Kaya, *Chem. Phys. Lett.* **94**, 97 (1983); A. Oikawa, H. Abe, N. Mikami, and M. Ito, *J. Phys. Chem.* **87**, 5083 (1983); R. J. Lipert and S. D. Colson, *J. Phys. Chem.* **93**, 135 (1989); M. Schütz, T. Bürgi, S. Leutwyler, and T. Fischer, *J. Chem. Phys.* **98**, 3763 (1993); T. Ebata, N. Mizuochi, T. Watanabe, and N. Mikami, *J. Phys. Chem.* **100**, 546 (1996); T. Watanabe, T. Ebata, S. Tanabe, and N. Mikami, *J. Chem. Phys.* **105**, 407 (1996).

3. M. Gerhards, M. Schmitt, K. Kleinermanns, and W. Stahl, *J. Chem. Phys.* **104**, 967 (1996).

4. G. Berden, W. L. Meerts, M. Schmitt, and K. Kleinermanns, *J. Chem. Phys.* **104**, 972 (1996).

5. A. Oikawa, H. Abe, N. Mikami, and M. Ito, *J. Phys. Chem.* **88**, 5180 (1984).

6. J. R. Johnson, K. D. Jordan, D. F. Plusquellic, and D. W. Pratt, *J. Chem. Phys.* **93**, 2258 (1990).

7. D. Schemmel and M. Schütz, *J. Chem. Phys.* **129**, 034301 (2008).

8. Y. Matsumoto, T. Ebata, and N. Mikami, *J. Chem. Phys.* **109**, 6303 (1998).

9. Y. Matsumoto, T. Ebata, and N. Mikami, *J. Phys. Chem. A* **105**, 5727 (2001).

10. A. J. Fleisher, P. J. Morgan, and D. W. Pratt, *J. Chem. Phys.* **131**, 211101 (2009).

11. W. A. Majewski, J. F. Pfanstiel, D. F. Plusquellic, and D. W. Pratt, in *Laser Techniques in Chemistry*, edited by A. B. Myers and T. Rizzo (Wiley, New York, 1995), p. 101.

12. T. M. Korter, D. R. Borst, C. J. Butler, and D. W. Pratt, *J. Am. Chem. Soc.* **123**, 96 (2001).

13. D. G. Lister, J. K. Tyler, J. H. Høg, and W. Larsen, *J. Mol. Struct.* **23**, 253 (1974).

14. D. F. Plusquellic, Ph.D. Thesis, University of Pittsburgh, 1992.

15. D. F. Plusquellic, R. D. Suenram, B. Mate, J. O. Jensen, and A. C. Samuels, *J. Chem. Phys.* **115**, 3057 (2001).

16. M. J. Frisch, G. W. Trucks, H. B. Schlegel, G. E. Scuseria, M. A. Robb, J. R. Cheeseman, J. Montgomery, J. A., T. Vreven, K. N. Kudin, J. C. Burant, J. M. Millam, S. S. Iyengar, J. Tomasi, V. Barone, B. Mennucci, M. Cossi, G. Scalmani, N. Rega, G. A. Petersson, H. Nakatsuji, M. Hada, M. Ehara, K. Toyota, R. Fukuda, J. Hasegawa, M. Ishida, T. Nakajima, Y. Honda, O. Kitao, H. Nakai, M. Klene, X. Li, J. E. Knox, H. P. Hratchian, J. B. Cross, V. Bakken, C. Adamo, J. Jaramillo, R. Gomperts, R. E. Stratmann, O. Yazyev, A. J. Austin, R. Cammi, C. Pomelli, J. W. Ochterski, P. Y. Ayala, K. Morokuma, G. A. Voth, P. Salvador, J. J. Dannenberg, V. G. Zakrzewski, S. Dapprich, A. D. Daniels, M. C. Strain, O. Farkas, D. K. Malick, A. D. Rabuck, K. Raghavachari, J. B. Foresman, J. V. Ortiz, Q. Cui, A. G. Baboul, S. Clifford, J. Cioslowski, B. B. Stefanov, G. Liu, A. Liashenko, P. Piskorz, I. Komaromi, R. L. Martin, D. J. Fox, T. Keith, M. A. Al-Laham, C. Y. Peng, A. Nanayakkara, M. Challacombe, P. M. W. Gill, B. Johnson, W. Chen, M. W. Wong, C. Gonzalez, and J. A. Pople, GAUSSIAN 03 (Gaussian, Inc., Wallingford, CT, 2004).

17. Y. Zhao, N. E. Schultz, and D. G. Truhlar, *J. Chem. Theory Comput.* **2**, 364 (2006).

18. T. H. Dunning, Jr., *J. Chem. Phys.* **90**, 1007 (1989).

19. J. B. Foresman, M. Head-Gordon, J. A. Pople, and M. J. Frisch, *J. Phys. Chem.* **96**, 135 (1992).

20. M. M. Francl, W. J. Pietro, W. J. Hehre, J. S. Binkley, M. S. Gordon, D. J. DeFrees, and J. A. Pople, *J. Chem. Phys.* **77**, 3654 (1982).

21. P. Y. Ayala and H. B. Schlegel, *J. Chem. Phys.* **107**, 375 (1997).

22. Y. Zhao and D. G. Truhlar, *Theor. Chem. Acc.* **120**, 215 (2008).

23. L. A. Curtiss, P. C. Redfern, K. Raghavachari, V. Rassolov, and J. A. Pople, *J. Chem. Phys.* **110**, 4703 (1999).

24. L. Song, Y. Mo, Q. Zhang, and W. Wu, *J. Comput. Chem.* **26**, 514 (2005).

25. M. W. Schmidt, K. K. Baldridge, J. A. Boatz, S. T. Elbert, M. S. Gordon, J. H. Jensen, S. Koseki, N. Matsunaga, K. A. Nguyen, and et al., *J. Comput. Chem.* **14**, 1347 (1993).

26. S. H. Vosko, L. Wilk, and M. Nusair, *Can. J. Phys.* **58**, 1200 (1980); C. Lee, W. Yang, and R. G. Parr, *Phys. Rev. B: Condens. Matter.* **37**, 785 (1988); A. D. Becke, *J. Chem. Phys.* **98**, 1372 (1993); P. J. Stephens, F. J. Devlin, C. F. Chabalowski, and M. J. Frisch, *J. Phys. Chem.* **98**, 11623 (1994).

27. M. Schütz, T. Bürgi, S. Leutwyler, and T. Fischer, *J. Chem. Phys.* **99**, 1469 (1993).

28. J. K. G. Watson, in *Vibrational Spectra and Structure*, edited by J. R. Durig (Elsevier Scientific Publishing Company, New York, 1977), Vol. 6, p. 1.

29. J. Kraitchman, *Am. J. Phys.* **21**, 17 (1953).

30. D. R. Herschbach, *J. Chem. Phys.* **31**, 91 (1959).

31. *Tables Relating to Mathieu Functions*. (Columbia University Press, New York, 1951).

32. D.-L. Joo, R. Takahashi, J. O'Reilly, H. Kato, and M. Baba, *J. Mol. Spectrosc.* **215**, 155 (2002).

33. E. Pines, D. Pines, Y.-Z. Ma, and G. R. Fleming, *Chem. Phys. Chem.* **5**, 1315 (2004).

34. T. M. Korter, D. W. Pratt, and J. Küpper, *J. Phys. Chem. A* **102**, 7211 (1998).

35. C. Jacoby and M. Schmitt, *Chem. Phys. Chem.* **5**, 1686 (2004).

36. S. J. Humphrey and D. W. Pratt, *J. Chem. Phys.* **104**, 8332 (1996); D. F. Plusquellic, X.-Q. Tan, and D. W. Pratt, *J. Chem. Phys.* **96**, 8026 (1992).

37. C. Kang, T. M. Korter, and D. W. Pratt, *J. Chem. Phys.* **122**, 174301 (2005).

38. D. R. Borst, T. M. Korter, and D. W. Pratt, *Chem. Phys. Lett.* **350**, 485 (2001); J. A. Reese, T. V. Nguyen, T. M. Korter, and D. W. Pratt, *J. Am. Chem. Soc.* **126**, 11387 (2004).

39. M. D. Harmony, *Chem. Soc. Rev.* **1**, 211 (1972).

40. B. Born, S. J. Kim, S. Ebbinghaus, M. Gruebele, and M. Havenith, *Faraday Discuss.* **141**, 161 (2009); M. Heyden, J. Sun, S. Funkner, G. Mathias, H. Forbert, M. Havenith, and D. Marx, *Proc. Natl. Acad. Sci. U.S.A.* **107**, 12068 (2010).

41. D. Laage and J. T. Hynes, *Science* **311**, 832 (2006).

42. V. Hanninen, T. Salmi, and L. Halonen, *J. Phys. Chem. A* **113**, 7133 (2009).

43. Y. Mo, J. Gao, and S. D. Peyerimhoff, *J. Chem. Phys.* **112**, 5530 (2000).

44. Y. Mo, L. Song, and Y. Lin, *J. Phys. Chem. A* **111**, 8291 (2007).

45. A. Cembran, L. Song, Y. Mo, and J. Gao, *J. Chem. Theory Comput.* **5**, 2702 (2009).

46. Y. Mo and J. Gao, *J. Phys. Chem. A* **105**, 6530 (2001); C. S. Brauer, M. B. Craddock, J. Kilian, E. M. Grumstrup, M. C. Orilall, Y. Mo, J. Gao, and K. R. Leopold, *J. Phys. Chem. A* **110**, 10025 (2006).

47. G. Gregoire, C. Dedonder-Lardeux, C. Jouvet, S. Martrenchard, A. Peremans, and D. Solgadi, *J. Phys. Chem. A* **104**, 9087 (2000).

48. See supplementary material at http://dx.doi.org/10.1063/1.3562373 for previously unpublished *trans*-2HN data as well as vector model energy decomposition data.

49. D. Schemmel and M. Schütz, *J. Chem. Phys.* **127**, 174304 (2007).

50. D. M. Miller, J. W. Young, P. J. Morgan, and D. W. Pratt, *J. Chem. Phys.* **133**, 124312 (2010).

5.0 HIGH RESOLUTION ELECTRONIC SPECTROSCOPY STUDIES OF *META*-AMINOBENZOIC ACID IN THE GAS PHASE REVEAL THE ORIGINS OF ITS SOLVATOCHROMIC BEHAVIOUR

Reprinted with permission from *Chem. Phys. Chem.*

Adam J. Fleisher, Philip J. Morgan, and David W. Pratt, *Chem. Phys. Chem.* **12**, 1808 (2011).

AJF and PJM performed the experimental measurements and analyzed the field free spectra. AJF analyzed the Stark spectra and performed theoretical calculations. AJF and DWP wrote the paper.

5.1 ABSTRACT

A theoretical and experimental investigation of *meta*-aminobenzoic acid (MABA) in the gas phase is presented, with the goal of understanding counter-intuitive observations on the solvatochromism of this "push-pull" molecule. The adiabatic excitation energies, transition moments, and excited state structures are examined using the complete active space self-consistent field approach (CASSCF and CASPT2), which shows the first excited electronic state of MABA to be of greater charge transfer character than was found in the *para* isomer (PABA). The rotationally resolved electronic spectrum of MABA reveals the existence of two rotamers, owing to asymmetry in the carboxylic acid functional group. Stark measurements in a molecular beam show the change in permanent dipole moment upon excitation to be $\Delta\mu \approx 3.5$ D for both rotamers, more than three times larger than that found in PABA. The excited state measurements reported here, along with supporting data from theory, clearly demonstrate how the *meta*-directing effects of asymmetric substitution in aniline derivatives can drive charge transfer pathways in the isolated molecule.

5.2 INTRODUCTION

Aminobenzoic acid (ABA) can exist in three isomeric forms, with an electron donating functional group ($-NH_2$) located either *ortho*, *meta*, or *para* relative to an electron accepting group (–COOH). This family of "push-pull" compounds is the focus of several applications, including the design of innovative pharmaceuticals,[1,2] the study of bioactive nanoparticles,[3] and the development of novel electronic devices and polymeric materials.[4,5] In a more general sense,

the properties of a wide variety of benzoic acid derivatives are influenced by the relative location and inductive capabilities of different functional groups. Hammett sigma constants (σ_H)[6] have long provided a measure of the inductive properties of these groups. The σ_H constant is unique to specific functional group position, allowing for a direct comparison of *meta* effects on benzoic acid (-0.16 for $-NH_2$) with *para* effects (-0.66) in the condensed phase. The more negative σ_H, the less acidic the carboxylic acid group of benzoic acid becomes. When these molecules are introduced into the gas phase, much can be learned about their structure and electron distributions, void of bulk solvent influences.

In the gas phase, two rotamers of *meta*-ABA (MABA) have been identified using a hole burning multiphoton ionization technique.[7] They differ by a 180° rotation of carboxylic acid about its bond with the aniline ring, leading to the stable *cis* and *trans* rotamers shown in Scheme 5-1.

Scheme 5-1

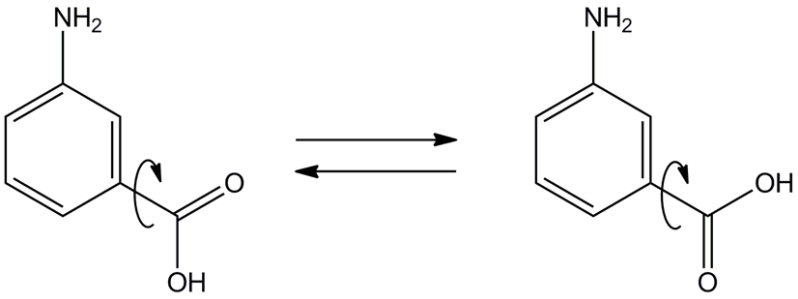

cis-MABA *trans*-MABA

Only a single rotamer of *para*-ABA (PABA) exists in the gas phase, and its structure and electronic distribution have been determined experimentally in both the ground (S_0) and first excited (S_1) electronic states.[8] The different ABA isomers are postulated to have varying degrees

of charge transfer (CT) character in both electronic states in the condensed phase.[9-13] Here, we aim to compare the "electron donor" strength of $–NH_2$ with the "electron acceptor" strength of –COOH as a function of their relative position. Our tool is high resolution S_1-S_0 electronic spectroscopy both in the absence and presence of an applied electric field. We thus explore the origins of these effects by determining how the structures and electronic distributions of both rotamers are modified by the absorption of light.

To the best of our knowledge, the excited state properties of MABA have been studied theoretically at only the configuration interaction singles (CIS) level.[11] Since high resolution spectroscopy can unambiguously assign the excitation energy and inertial parameters of each rotamer, we have employed the complete active space self-consistent field method (CASSCF), corrected for dynamic electron correlation (CASPT2), to better model the subtle differences in rotamer $S_1 \leftarrow S_0$ excitations. With this multi-configurational technique, we also aim to explore the perturbation of molecular orbitals that can arise from systematic changes in molecular symmetry.

5.3 EXPERIMENTAL SECTION

5.3.1 Theory

All calculations were performed with GAUSSIAN 03[14] at the University of Pittsburgh Center for Molecular and Materials Simulations (CMMS). An initial set of molecular orbitals was generated at the HF/3-21G level for each molecule, and an active space of six benzene-like π orbitals was chosen for CASSCF calculations. Beginning with the 3-21G basis set, more atomic orbitals,

polarization, and diffuse functions were added step-wise until the ABA geometries under investigation were fully optimized for S_0 using a split-valence correlation-consistent basis set with additional polarization and diffuse functions (aug-cc-pVDZ). Then, the S_1 geometries were optimized (CASSCF/aug-cc-pVDZ), beginning with the optimized S_0 geometries. Corrections to the optimized geometries for dynamic electron correlation using MP2 was done to improve the reported theoretical excitation energies (CASPT2).

In addition to the CAS calculations, HF, MP2, B3LYP and M05-2X theories were used to model the S_0 structure and dipole moments. In S_1, CIS structures and dipole moments were optimized beginning with the HF S_0 geometry. Again, all calculations were performed with the aug-cc-pVDZ basis set.

5.3.2 Experiment

The vibrationally resolved experiment was performed using a pulsed supersonic jet laser spectrometer.[15] MABA purchased from Aldrich was mixed with an excess of diatomaceous earth (Celite 545) from Fisher Scientific to minimize decomposition inside the high temperature source. The mixture was heated to ~ 180 °C and seeded in dry helium gas at a total pressure of 2 ktorr. The sample gas was introduced into a vacuum chamber (10^{-5} torr) through the 1 mm diameter pinhole of a pulsed General Valve (series 9) nozzle operating at 10 Hz. The supersonic expansion was crossed at a right angle 2 cm downstream with the pulsed output of a frequency doubled dye laser (Quanta Ray PDL-1), also operating at a repetition rate of 10 Hz. The laser system consisted of the second harmonic output of a Nd^{3+}:YAG laser (Quanta Ray DCR-1A), which pumped a dye laser using DCM laser dye purchased from Exciton. The output of the dye laser was frequency doubled using a potassium dihydrogen phosphate (KD*P) crystal and

directed through the jet spectrometer. The resulting fluorescence excitation signal was collected by a photomultiplier tube (PMT) mounted perpendicular to the jet expansion and laser beam, processed by a boxcar integrator (Stanford Research Systems), and recorded digitally with QUICK DATA ACQUISITION software (version 1.0.5). The laser power was measured throughout the experiment and also processed by the boxcar integrator, ensuring power normalization of the vibrationally resolved spectrum.

The rotationally resolved experiments were performed with a continuous molecular beam laser spectrometer.[16] MABA was heated to ~ 200 °C inside a quartz source and seeded in a backing gas of dry argon at a total pressure of 300 torr. The sample gas was expanded through a 240 μm pinhole into a vacuum chamber (10^{-6} torr) and skimmed 2 cm downstream. Following the 1 mm diameter skimmer, the molecular beam entered a second vacuum chamber (10^{-7} torr), where it was crossed 13 cm after skimming with a perpendicularly propagating continuous wave laser beam. This high resolution system consists of a modified ring dye laser (Spectra Physics) containing DCM laser dye pumped by the 514 nm line of an argon ion laser. The fundamental output was frequency doubled with a Wavetrain frequency doubler (Spectra Physics) using a lithium borate (LBO) crystal cut at Brewster's angle for 655 nm light, resulting in a UV light beam of 1 MHz bandwidth with typical output power of ~ 500 μW. Total fluorescence was collected with spherical optics and focused into a PMT (EMI 9813 QB) located perpendicular to both beams. The fluorescence excitation signal was recorded along with the absorption spectrum of iodine for absolute frequency calibration. The frequency markers of a temperature stabilized etalon (FSR = 299.7520 MHz in the fundamental) were also recorded and used for relative frequency calibration. Stark optics were used in the electric field experiments, and were calibrated using the known dipole moments of aniline.[17]

5.4 RESULTS AND DISCUSSION

5.4.1 Theoretical S_0 structures and dipole moments

Ground state structures of each rotamer were optimized using five levels of theory; HF, CASSCF, MP2, B3LYP and M05-2X. All optimizations reported here were performed with the aug-cc-pVDZ basis set. The theoretical rotational constants listed in Table 5-1 will act as the structural benchmark with which experimentally determined constants can be compared. The dipole moment projections onto the inertial axes predicted by theory are also summarized in Table 5-1. For *cis*-MABA, the total ground state dipole ranges from 2.3 to 2.6 D. The *trans*-MABA rotamer has a larger total dipole in S_0, ranging from 3.0 to 3.7 D. At the CASSCF level, *cis*-MABA is more stable in S_0 than *trans*-MABA by 77 cm^{-1}, 52 cm^{-1} using CASPT2.

5.4.2 Theoretical S_1 structures and dipole moments

Excited state structures of each rotamer were optimized using two levels of theory, CIS and CASSCF, in order to explore adiabatic excitation properties. Rotational constants and dipole moments from these optimizations are also listed in Table 5-1. *Trans*-MABA also is predicted to have the larger permanent electric dipole in the S_1 electronic state. At the CASSCF level, *cis*-MABA is predicted to be more stable than *trans*-MABA in the excited state by 61 cm^{-1}, 12 cm^{-1} using CASPT2.

Table 5-1. Theoretical rotational constants (MHz), inertial defects (uÅ^2), and dipole moments (Debye) of MABA.

	S_0					S_1	
	HF	CASSCF	MP2	B3LYP	M05-2X	CIS	CASSCF
				cis-MABA			
A	2715.8	2694.3	2632.3	2663.9	2685.7	2715.4	2656.2
B	951.9	944.9	935.6	939.9	949.6	943.2	926.3
C	705.3	700.1	690.8	695.1	701.9	700.0	687.1
ΔI	-0.493	-0.556	-0.518	-0.392	-0.402	0.000	-0.331
μ_a	1.81	1.48	1.94	2.25	2.13	5.00	2.49
μ_b	1.26	1.46	0.87	0.88	0.96	0.26	1.34
μ_c	1.04	1.10	0.99	0.86	0.91	0.00	0.84
μ	2.44	2.35	2.34	2.57	2.51	5.01	2.95
				trans-MABA			
A	2665.6	2643.4	2587.6	2616.7	2638.9	2674.6	2612.4
B	962.2	955.5	945.6	949.9	959.4	952.0	935.2
C	707.4	702.3	693.0	697.3	704.0	702.1	689.0
ΔI	-0.491	-0.547	-0.513	-0.395	-0.407	0.000	-0.345
μ_a	2.66	2.36	2.63	2.99	2.89	5.74	3.32
μ_b	1.75	1.56	1.62	1.84	1.83	3.02	1.83
μ_c	1.04	1.10	1.00	0.87	0.92	0.00	0.84
μ	3.35	3.04	3.25	3.62	3.54	6.48	3.88

5.4.3 Experimental rotational constants, transition moments, and dipole moments

The vibrationally resolved fluorescence excitation spectrum (FES) of MABA is shown in Figure 5-1. The spectrum features two MABA origin transitions, labeled "I" and "II". They are separated by 26 cm^{-1}, nearly identical to the separation previously measured by REMPI.[7] Also, water present in the diatomaceous earth apparently allowed for the formation of 1:1 and 1:2 water complexes, labeled "W_1" (30357 and 30364 cm^{-1}) and "W_2" (30407 and 30410 cm^{-1}), respectively. These bands have also been previously reported,[18] and their frequencies are in good agreement with those reported there. However, it is interesting to note that the separations of the complex bands are significantly different from 26 cm^{-1}.

Rotationally resolved experiments were conducted on each bare MABA origin in Figure 5-1. Initially, rotational constants estimated from *ab initio* geometry optimizations were used to simulate each spectrum, and then the inertial parameters were iteratively adjusted and fit to experiment in a least-squares fashion using the JB95 fitting program.[19] The rotationally resolved spectra of Bands I and II are shown in Figures 5-2 and 5-3, respectively. The fit simulations are in excellent agreement with experiment, and the fitting parameters are listed in Table 5-2.

MABA is confirmed to be nearly planar in both electronic states, as evidenced by the small, negative inertial defects ($\Delta I = I_c - I_a - I_b$) reported in Table 5-2. Therefore, the differences in rotational constants between the two rotamers (within a single electronic state) are a consequence of changes in some in-plane atomic positions. Focusing on the ground state, the *A* constant of rotamer I is larger than that of II, meaning that some atomic positions in I are closer to the *a*-axis than they are in structure II. Conversely, the *B* constant of rotamer I is smaller than that of II, indicative of a structure with atoms located further from the *b*-axis. We hypothesize

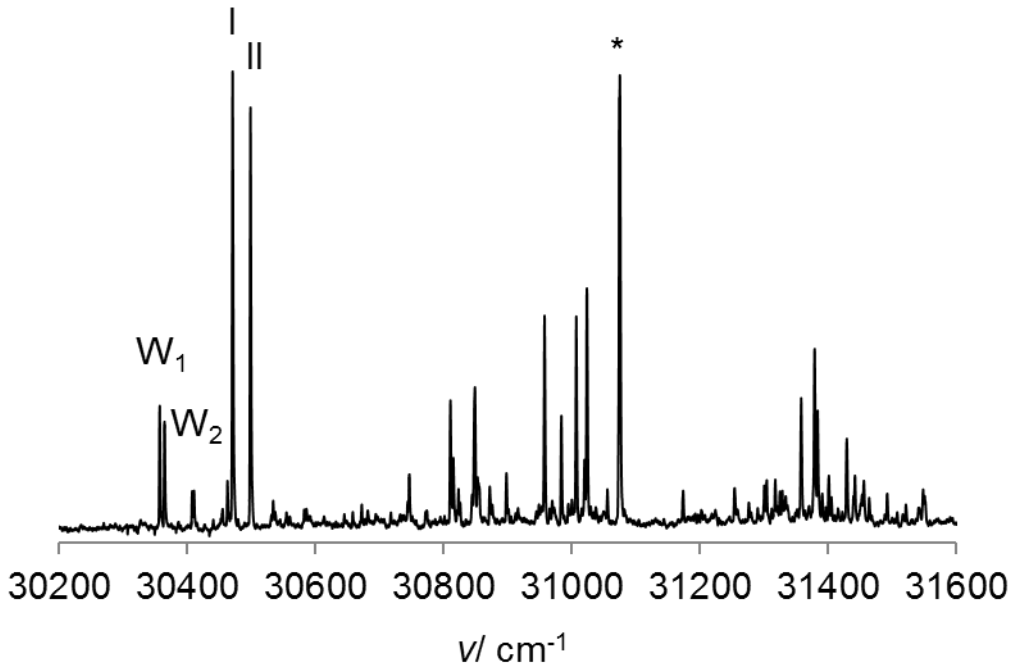

Figure 5-1. Vibrationally resolved fluorescence excitation spectrum (FES) of MABA. The spectrum closely resembles the combined REMPI spectra of MABA (I and II), MABA-H_2O (W_1), and MABA-$(H_2O)_2$ (W_2) previously reported.[6,17] The transition marked with an asterisk (*) is the electronic origin of pyrimidine, a contaminant in the spectrometer.

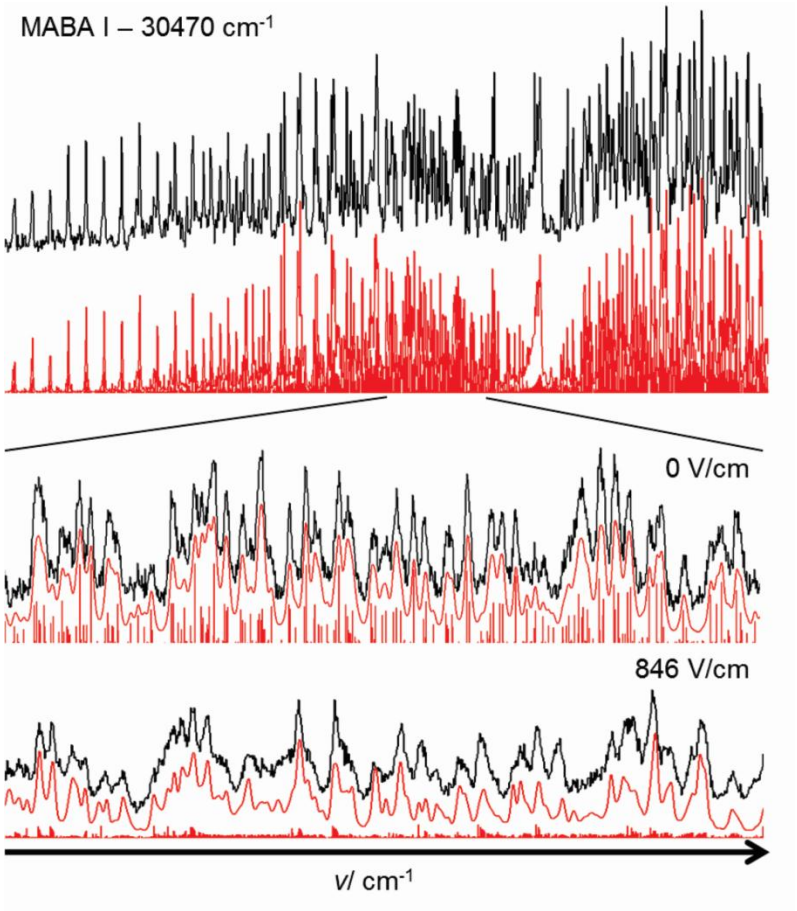

Figure 5-2. Rotationally resolved FES of MABA I. The experimental spectrum is in black, and the fit simulation is in red. The top panel spans a frequency range of 2.61 cm^{-1}, whereas the middle and bottom panels span only 0.32 cm^{-1}. The Stark effect is shown in the bottom panel.

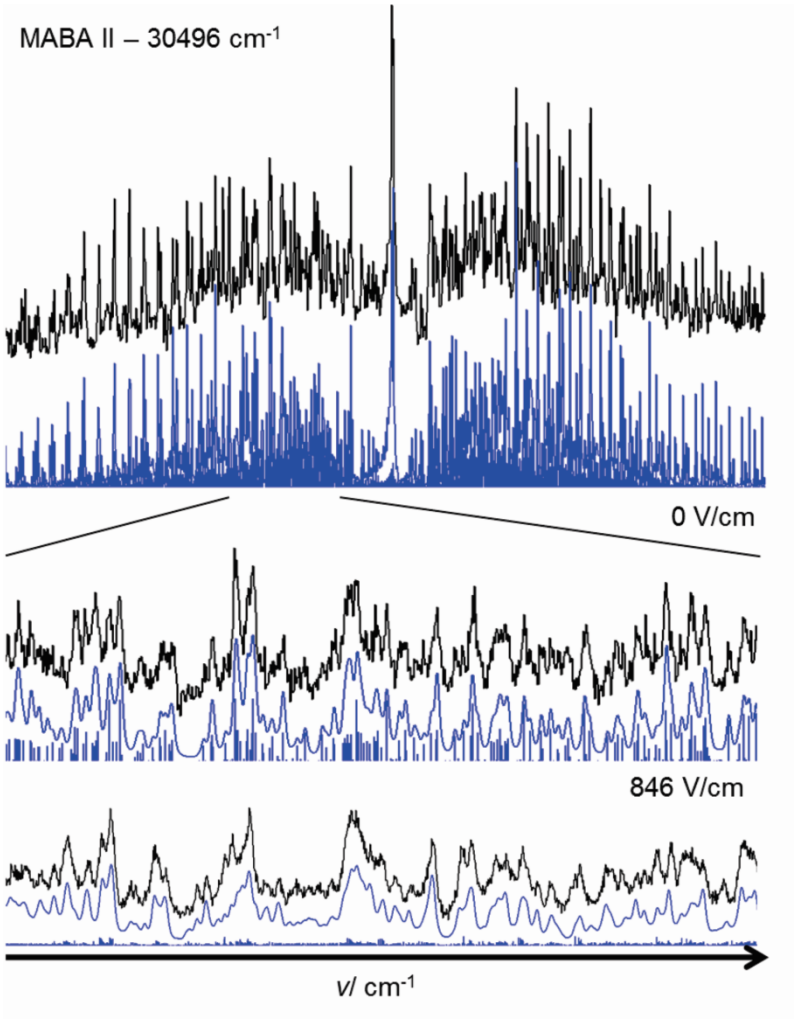

Figure 5-3. Rotationally resolved FES of MABA II. The experimental spectrum is shown in black, and the fit simulation is in blue. The top panel spans a frequency range of 2.88 cm^{-1}, whereas the middle and bottom panels span only 0.32 cm^{-1}. The Stark effect is shown in the bottom panel.

Table 5-2. Experimentally determined inertial parameters of MABA. Each rotational constant has a standard deviation of 0.1 MHz. S_0 and S_1 rotational constants were varied, along with the origin, to produce the final fits to experiment shown in Figures 5-2 and 5-3.

	I	II
S_0		
A (MHz)	2677.5	2629.4
B (MHz)	947.2	957.5
C (MHz)	700.4	702.6
ΔI (uÅ^2)	-0.750(6)	-0.76(2)
κ	-0.750	-0.735
S_1		
A (MHz)	2671.6	2631.5
B (MHz)	936.3	944.9
C (MHz)	693.7	695.6
ΔI (uÅ^2)	-0.377(7)	-0.39(2)
κ	-0.755	-0.742
Origin (MHz)	913472913(30)	914258121(30)
TM (*a*/*b*/*c*)	16/84/0	22/78/0
fit lines	380	245
OMC (MHz)	1.2	3.1
fit lines / parameter	54.3	35.0

that the –COOH orientation in rotamer I must place more of the functional group mass in close proximity to the *a*-axis, and further from the *b*-axis than in rotamer II.

Both I and II exhibit mixed *a*/*b* type selection rules, as evidenced by the presence of P, Q, and R branches in the high resolution spectra. As refinements to the inertial parameters were made, it became possible to fit each rotamer to a unique *a*/*b* hybrid band type, also listed in Table 5-2. The rotamers have nearly identical hybrid band types (I, 16/84; II, 22/78), meaning that the symmetries of the molecular orbitals involved in the excitation are the same for each rotamer. The slight difference in band type is a result of each rotamer having differently oriented principal inertial axes. The final adjustment made to each simulation was the inclusion of a Voigt line profile through the combination of Doppler (Gaussian) and lifetime (Lorentzian) broadenings. For each rotamer, the Doppler component was fixed to 30 MHz, close to the limiting Doppler resolution of the molecular beam spectrometer. The Lorentzian contributions that then best fit the experiment were 65 and 50 MHz, respectively. Each component to the total line width has an uncertainly of ± 5 MHz, rendering the excited state fluorescence lifetimes of each rotamer effectively identical. The fluorescence lifetime of MABA determined from the averaged Lorentzian line width is ~ 3 ns.

Rotationally resolved experiments in the presence of a static electric field were also performed on each rotamer. The spatial degeneracy of the total angular momentum of the molecule is lifted by the application of an electric field, resulting in splitting and frequency shifting of rotational energy levels in each electronic state. This is evident in the bottom panels of Figures 5-2 and 5-3, where the Stark spectra of I and II are shown at full resolution. Keeping all inertial parameters determined from the zero-field experiments constant, the electric dipole

moment in each electronic state was iteratively fit in a least-squares fashion.[20] The projections of these values onto the inertial axes of each rotamer are listed in Table 5-3.

In the ground state, the dipole moment of I is smaller in magnitude (μ = 2.2 D) than the dipole moment of II (μ = 3.2 D). We postulate that the larger dipole is a consequence of the larger spatial separation of the $-NH_2$ group and the carbonyl functionality of the –COOH group. Following photoexcitation to S_1, the dipole moment of each MABA rotamer increases by ~ 3.5 D. The nearly identical increase in dipole moment is evidence for the same S_1 state being reached, independent of rotamer configuration. In contrast (see Table 5-3), the dipole moment of the single *para*-aminobenzoic acid (PABA) rotamer increases by only $\Delta\mu$ = 1.1 D,[8] significantly smaller than the $\Delta\mu$ values in MABA.

Clearly, the gas phase electronic properties of the ABAs are highly correlated with the relative location of each functional group. The *meta* derivative, with its functional groups closer in space than the *para* derivative, has a larger change in dipole upon excitation to S_1. This counter-intuitive observation, also seen in the same "push-pull" system almost 50 years ago,[21] will be explained in the following section.

5.4.4 Conformational assignment

As is apparent from our fits of the high resolution spectra, the species responsible for Bands I and II exhibit different rotational constants, making it possible to determine their structures. In both electronic states, the *A* constant of Band I is larger than it is in Band II; however, the *B* constant is smaller for Band I than for Band II. Comparing these results to theory (Table 5-1), we therefore assign Band I at 30470 cm^{-1} as the *cis*-MABA origin and Band II at 30496 cm^{-1} as the

Table 5-3. Measured permanent electric dipole moments of ABAs. In all cases, μ_c was measured as equal to zero. Standard deviations are shown in parentheses.

	MABA I	MABA II	PABA[a]
S_0			
μ_a (D)	2.1(1)	2.7(1)	3.12(8)
μ_b (D)	0.7(2)	1.7(1)	1.2(2)
μ (D)	2.2(1)	3.2(1)	3.3(2)
S_1			
μ_a (D)	5.7(1)	6.1(1)	4.21(8)
μ_b (D)	0.0(2)	2.9(1)	1.3(2)
μ (D)	5.7(1)	6.8(1)	4.4(1)
$\Delta\mu$ (D)[b]	3.7	3.6	1.1

[a]Data from Ref. 8.
[b]Determined from a vector subtraction of the S_1 and S_0 dipoles.

trans-MABA origin. This is the opposite of the previously proposed assignment using relative CIS excitation energies.[7]

Table 5-4 lists the theoretical excitation energies of the two rotamers of MABA along with other related properties of the S_1-S_0 transition. The excitation energies calculated using the mutli-configurational CASSCF approach compare more favorably with experiment than the CIS energies. A CASPT2 correction was done on the S_0 and S_1 CASSCF optimized structures, further improving the theoretical excitation energies relative to experiment. The average excitation energy of MABA is ~ 3.78 eV from experiment, whereas the average theoretical values are 4.61 eV for CIS, and 4.44 eV for CASSCF (3.99 eV with CASPT2). In Table 5-4, the *trans* origin band of MABA is predicted to lie to the red of the corresponding band of *cis*-MABA.

We predict a red shift of *trans*-MABA relative to *cis*-MABA of 243 cm^{-1} using CIS optimizations (with no a zero-point energy correction), very similar to the value of 240 cm^{-1} previously reported.[6] However, the higher level CASSCF S_1 adiabatic excitation energies predict a much smaller red shift (16 cm^{-1}, 40 cm^{-1} with CASPT2). A difference of 40 cm^{-1}, equivalent to ~ 0.005 eV, is too small to make a reliable origin assignment. Using structural constants to better differentiate between I and II, we conclude that *trans*-MABA is blue shifted relative to *cis*-MABA by 26 cm^{-1}.

A comparison of theoretical permanent dipole moments to those determined experimentally will corroborate the above rotamer assignments. Band I has a smaller total dipole in S_0 (2.2 D) than Band II (3.2 D), consistent with its assignment as *cis*-MABA. In S_1, Band I again has a smaller total dipole moment, again consistent with the *cis*-MABA data in Table 5-1. Particularly clear is the difference in excited state μ_b between I and II. In Table 5-3, μ_b = 0.0(2) D for Band I in S_1, considerably smaller than μ_b = 2.9(1) D for Band II. This striking difference in

Table 5-4. Theoretical properties of the MABA S_1-S_0 electronic excitation. E is the CASSCF adiabatic excitation energy, and E_{PT2} is the CASPT2 corrected energy. The percentage of reference, single, double, and triple excitation configurations is shown, followed by the natural orbital population of each MO in the active space. SLCs are the single excitations with the largest CI coefficients.

	cis-MABA		*trans*-MABA	
	CAS S_0	CAS S_1	CAS S_0	CAS S_1
E (cm^{-1})[a]		35857		35841 (-16)[b]
E_{PT2} (cm^{-1})		32169		32129 (-40)[b]
Ref (%)[c]	88.7	0.0	88.7	0.0
S (%)[c]	0.0	79.7	0.0	79.7
D (%)[c]	9.7	15.3	9.7	15.2
T (%)[c]	0.0	2.0	0.0	2.3
π_1 (a_{2u})	2.0	1.9	2.0	1.9
π_2 (e_{1g})	1.9	1.6	1.9	1.6
π_3 (e_{1g})	1.9	1.2	1.9	1.2
π_4 (e_{2u})	0.1	0.4	0.1	0.4
π_5 (e_{2u})	0.1	0.8	0.1	0.8
π_6 (b_{2g})	0.0	0.1	0.0	0.1
SLCs (%)[d]		$\pi_3 \rightarrow \pi_5$ (61)		$\pi_3 \rightarrow \pi_5$ (61)
		$\pi_2 \rightarrow \pi_4$ (19)		$\pi_2 \rightarrow \pi_4$ (19)

[a]The excitation energies predicted by CIS theory are 37334 and 37091 (-243) cm^{-1} for *cis* and *trans*-MABA, respectively. The corresponding electronic transition moments are 28/72/0 and 35/65/0 (*a*/*b*/*c*, %).

[b]The excitation energy of *trans*-MABA relative to *cis*-MABA is shown in parentheses.

[c]Electronic configurations with coefficients less than 0.05 were not included.

[d]CASSCF(12,10) optimizations with an extended active space, including π orbitals localized on the two functional groups, were done on *cis*-MABA. The same SLCs were found as in the CASSCF(6,6) work, and the TM orientation shown in Figure 5-5 was confirmed.

S_1 electronic distribution between I and II is supported by theory, and confirms the band assignments as *cis* and *trans*-MABA, respectively. Each rotamer is shown in its respective principal axis system in Figure 5-4, along with their measured dipole moments.

5.4.5 Evaluation of theory

In Table 5-5, the theoretical rotational constants and dipole moments are compared to experiment using the root mean square deviation formula in Equation 5-1.

Equation 5-1

$$\delta_{rms} = \sqrt{\frac{\sum_{g=a,b,c} \left(x_g^{ex} - x_g^{th} \right)^2}{n}}$$

Here, x_g^{ex} are the experimental rotational constants or dipole moments, x_g^{th} are the theoretical rotational constants or dipole moments, and n is the total number of data points compared (3 for the rotational constants, and 2 for the dipole moments). The smaller δ_{rms}, the better that level of theory compares to experiment.

The CASSCF approach predicts the S_0 rotational constants better than either HF or MP2, for each rotamer. The M05-2X density functional predicts the most accurate ground state structure, with $\delta_{rms} < 6$ MHz. In S_1, the δ_{rms} reported for CIS rotational constants is comparable to the HF approach for S_0. However, the CASSCF method predicts better S_1 rotational constants than CIS, with a low $\delta_{rms} < 13$ MHz. Even for this small system, the improved treatment of

Table 5-5. Root mean square deviations of theoretical rotational constants (*A*, *B*, *C*) and dipole moments (μ_a, μ_b) as compared to experiment.[a] Band I is assigned as *cis*-MABA, and Band II is assigned as *trans*-MABA.

	S_0					S_1	
	HF	CASSCF	MP2	B3LYP	M05-2X	CIS	CASSCF
cis-MABA							
δ_{rms} (MHz)	22.5	9.8	27.5	9.4	5.0	25.9	11.3
δ_{rms} (D)	0.4	0.7	0.2	0.2	0.2	0.5	2.5
trans-MABA							
δ_{rms} (MHz)	21.3	8.1	25.7	9.1	5.7	25.5	12.9
δ_{rms} (D)	< 0.0	0.3	0.1	< 0.0	0.2	0.3	2.1

[a]This comparison is only approximate, since the experimentally determined data are for the vibrationally averaged structure (r_0), and the theoretical data are for an equilibrium structure (r_e). However, the δ_{rms} values clearly indicate that the correct rotamer assignments have been made.

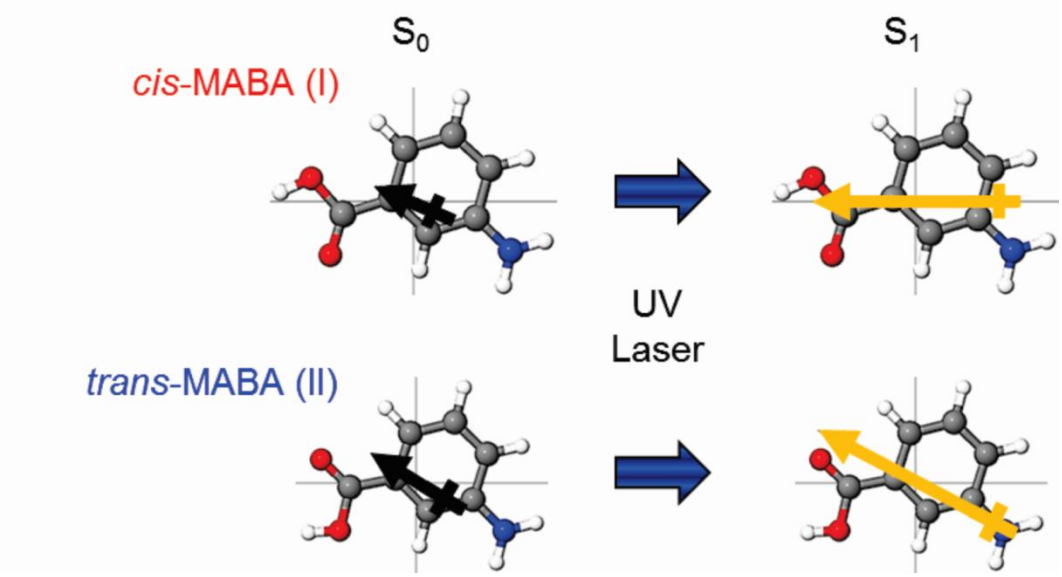

Figure 5-4. Assigned structures and dipole moments of the MABA rotamers.

dispersion interactions provided by M05-2X, and the multi-configurational nature of the CASSCF approach, offer valuable theoretical advantages for structural studies

The dipole moment root mean square deviations do not include a comparison of μ_c. In the rotationally resolved spectra of aniline[17,22] and of aniline derivatives,[8,23,24] it is well known that a fast motion along the $-NH_2$ inversion coordinate occurs in both S_0 and S_1, rendering μ_c effectively zero for each vibrationally averaged structure. We believe the same fast inversion is responsible for the measured μ_c = 0.0(2) D reported here. Therefore, we do not include the predicted μ_c values in determining δ_{rms}. The S_0 dipole moments are best predicted by the B3LYP and MP2 methods, although all of the δ_{rms} values are small compared to the respective total dipole moments. The HF theory predicts smaller deviations from experimental S_0 dipole moments than the CIS theory does with respect to the S_1 values.

5.4.6 Connections with ABA solvatochromism

The ABAs were among the first organic molecules to be studied using solvatochromic techniques.[21] In such experiments, one measures shifts in the maximum absorption ($\tilde{\nu}_{abs}$) and fluorescence ($\tilde{\nu}_{fluor}$) energies as a function of solvent polarity, and interprets the slopes of these resulting plots in terms of differences in the ground and excited state dipole moments. Applying this method to the ABAs, Mataga found that the slope of the MABA plot was greater than the corresponding slope of the PABA plot.[21] The simple yet counter-intuitive explanation of such an observation is that the $\Delta\mu$ upon excitation is greater for MABA than for PABA. If the "push-pull" CT nature of the substituents in ABA did not depend on their relative positions, $\Delta\mu$ should increase as the $-NH_2$ and –COOH groups are further apart. However, if the change in dipole

upon excitation is strongly dependent on relative substituent position, excited states of varying CT character could be responsible for the observed solvatochromic shifts.

Mataga suggested that a failure of PABA to reach the lowest energy local solvent configuration within the excited state fluorescence lifetime of the molecule was responsible for these curious condensed phase observations.[27] In the gas phase, the fluorescence lifetime of PABA is 5 ns (3 ns for MABA), long enough that solvent reorganization following excitation to a Franck-Condon S_1 state should be achieved. Alternatively, the assumption that long range interactions between the solute dipole and the solvent reaction field dominate the solvent dependent $\tilde{\nu}_{abs}$ and $\tilde{\nu}_{fluor}$ spectral shifts may fail for the aminobenzoic acids.

This breakdown is more pronounced in MABA than in PABA, as evidenced by recent solvatochromism studies of these compounds.[11-13] Inclusion of hydrogen bonding (HB) solvents in the Lippert-Mataga solvatochromic shift analysis is not valid,[27] as the molecular orbital overlap and electron exchange between solvent and solute can no longer be reasonably ignored. Therefore, the S_1 dipole moment estimates of Stalin *et al.*[11-13] include very local HB polarization and CT effects. As made clear by Mataga,[21] however, the qualitative comparison of $\Delta\mu$ between aminobenzoic acids when only non-HB solvents are taken into account yields the ordering $\Delta\mu_{MABA} > \Delta\mu_{PABA}$, the same ordering observed here in the gas phase. Also, Figure 6 of Ref. 21 clearly shows a much larger inclination of $\Delta\nu$ vs. $F(D, n)$ for MABA than PABA, when HB solvents are included.

Clear differences in the electronic structure of the ABA excited states are captured using the CASSCF approach. Shown in Figure 5-5 are the active space molecular orbitals (MOs) resulting from CASSCF S_1 geometry optimizations of MABA and PABA. The MOs chosen are polarized versions of the three occupied and three unoccupied Hückel orbitals of benzene (a_{2u},

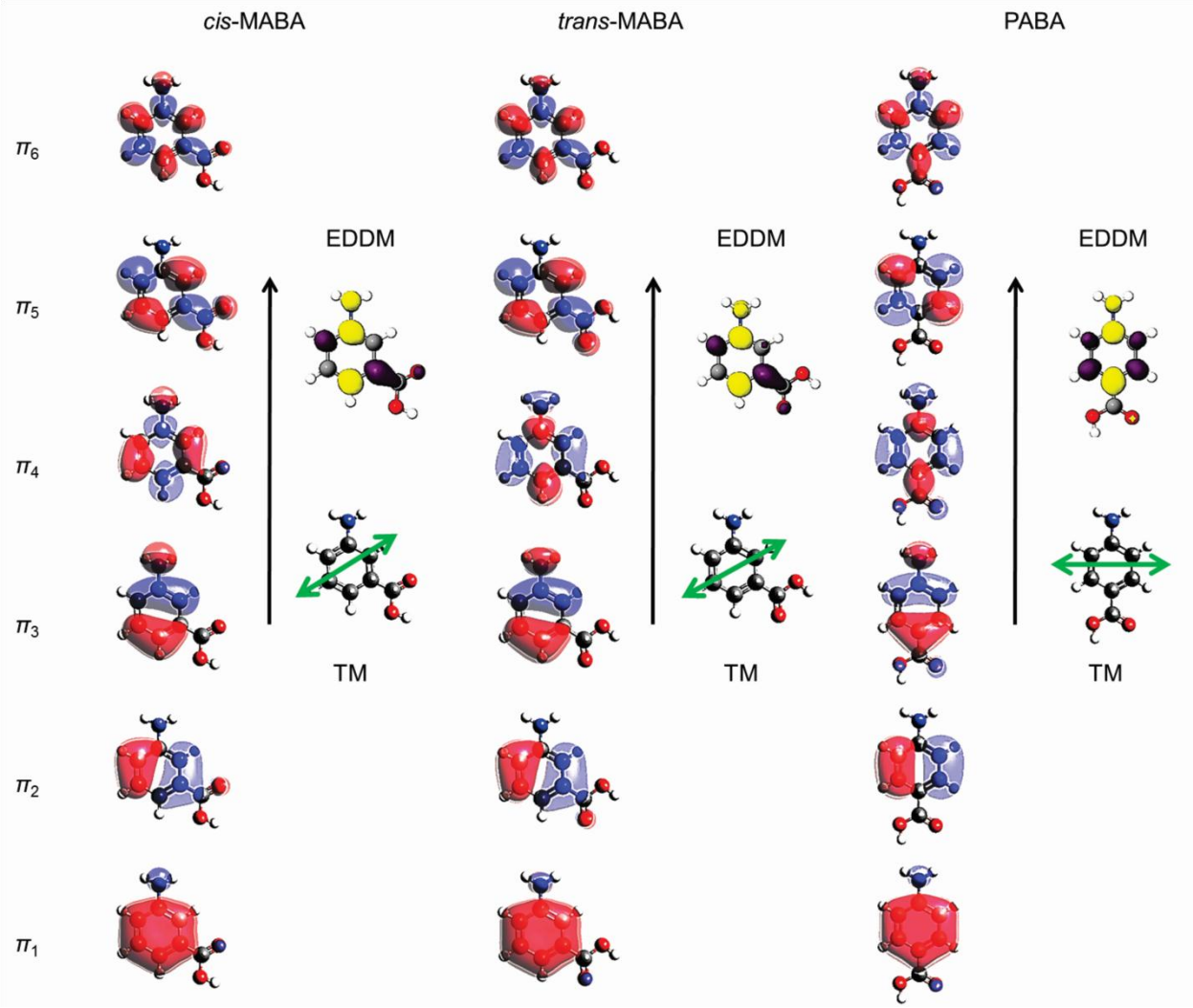

Figure 5-5. Molecular orbitals and excitation properties of MABA and PABA from the S_1 CASSCF optimized geometries of each isomer. The red and blue (opposite parity) MOs were created in AVOGADRO[25] using an isosurface value of 0.02. Electron density difference maps (EDDMs) were calculated as $(\pi_5)^2 - (\pi_3)^2$ with G03 and rendered in JMOL[26] using an isosurface value of 0.004. Areas of electron density gain upon excitation (black arrow) are shown in purple, and areas of electron density loss are shown in yellow. The electronic transition moment (TM) as estimated from the $(\pi_5 \otimes \pi_3)$ direct product is displayed below each EDDM as a green double-headed arrow.

e_{1g}, e_{2u}, and b_{2g} symmetries in the D_{6h} point group). Table 5-4 shows that, in S_0, the three lowest energy MOs in the active space ($\pi_1 - \pi_3$) are (almost) entirely occupied.

For PABA and aniline, the lowest energy excited state predicted by CIS calculations is the L_a state (*a*-type transition moment), contrary to experiment.[8] The CASSCF method used here correctly predicts S_1 to be the L_b origin for PABA, with the *b*-type transition moment (TM) shown in Figure 5-5. However, when the symmetry of the disubstituted benzene is broken by *meta* substitution, the L_b state takes on more CT character, and the orientation of the inertial axes along with distortions to the MOs by the polarizing functional groups results in the experimentally observed *a*/*b* hybrid TM for MABA.

Our experimental results support the solvatochromism findings discussed above, but point to an alternative explanation of the condensed phase data. In MABA, S_1 is also the L_b state, but one of greater CT character than the L_b state of PABA. The differences in nodal patterns can be understood visually through the electron density difference maps of MABA and PABA presented in Figure 5-5. In both rotamers of MABA, the carbonyl oxygen gains electron density (purple) upon excitation. This is coupled with a large gain in density at the –COOH bond with the aniline ring. In PABA, the –COOH carbonyl oxygen actually donates electron density (yellow) to the ring upon excitation.

The underlying difference in the locally excited states reached by MABA and PABA is the *meta* orientation of each substituent, which promotes the coupled electron donor and electron acceptor behavior of $–NH_2$ and –COOH, as illustrated in Scheme 5-2 below. The partial charges (shown in circles) derived from all possible resonance structures of aniline and benzoic acid mutually reinforce each other, promoting CT from $–NH_2$ to –COOH in the *meta* isomer. This is not the case in PABA as the two effects cancel, therefore suppressing the "push-pull" nature of

that molecule. The dipole ordering in S_1 of $\mu_{MABA} > \mu_{PABA}$ is supported by the slopes of each solvatochromism plot when HB solvents are removed.

When HB solvents are included, the increase in solvatochromic slope is greater for MABA than for PABA. The CT S_1 of MABA should be further stabilized by HB, increasing charge separation beyond that observed in the gas phase. The HB effect on PABA is less pronounced, since S_1 is comprised of a more local excitation (LE). Tuning from LE to CT within these L_b excited states when the substituents of aminobenzoic acid are moved from a *para* to a *meta* position appears to also be true in the condensed phase.

Scheme 5-2

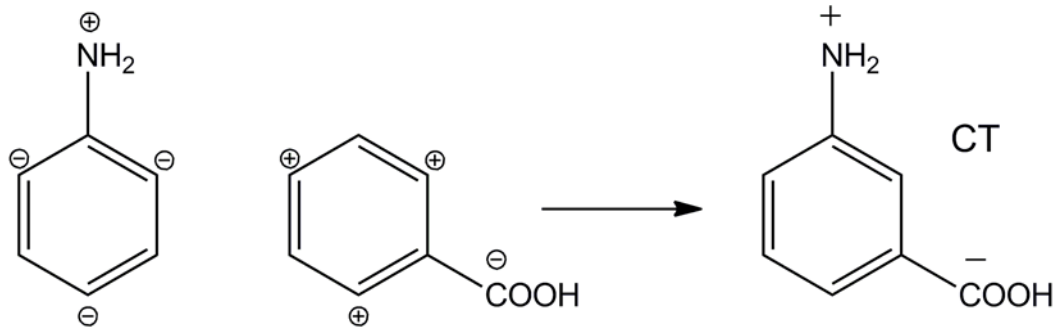

5.5 CONCLUSIONS

The average dipole moment of MABA in S_0 is μ = 2.7 D, compared to μ = 3.3 D for PABA in the same electronic state. Clearly, there is (on average) more charge separation in S_0 between the donor and acceptor groups in PABA than in MABA, meaning that *para* substitution induces a larger negative charge on benzoic acid than substitution in the *meta* position does. These S_0 gas

phase observations agree with the condensed phase trend in acidity of amino substituted benzoic acids as measured by σ_H.

However, upon excitation to S_1, the molecular orbitals of PABA are changed by *meta* substitution. This excited state polarization results in a locally excited L_b state in PABA with suppressed CT character, which leads to MABA having the larger S_1 permanent dipole of the two isomers. Consequently, MABA experiences an increase in permanent dipole upon excitation three times that observed in PABA. Within the MABA family, the *trans* rotamer has a nearly identical dipole orientation in S_0 and S_1, whereas the *cis* dipole orientation changes upon excitation (see Figure 5-4). This subtle difference between the rotamers can only be detected when information about the individual dipole moment projections onto the internal inertial axes is available. Thus, if it were possible to perform solvatochromic experiments on the separate isomers, *trans*-MABA would exhibit the larger shift.

In the disubstituted benzene ring systems studied here, it is the excited state electronic properties that are the most different between *para* and *meta* isomers. Taking advantage of these distinguishing characteristics in S_1 could aid in the development of gas phase molecular separation, orientation, and alignment techniques.

5.6 ACKNOWLEDGEMENTS

We gratefully acknowledge the support of Diane Miller throughout this project, and the help of Richard Christie from the University of Pittsburgh CMMS. We thank the NSF (CHE-0911117) and the Andrew Mellon Predoctoral Fellowship Program (AJF) for funding.

5.7 REFERENCES

1. P. Chand, Y. S. Babu, S. Bantia, N. Chu, L. B. Cole, P. L. Kotian, W. G. Laver, J. A. Montgomery, V. P. Pathak, S. L. Petty, D. P. Shrout, D. A. Walsh, and G. M. Walsh *J. Med. Chem.* **40**, 4030 (1997).

2. A. Kluczyk, T. Popek, T. Kiyota, P. de Macedo, P. Stefanowicz, C. Lazar, and Y. Konishi *Curr. Med. Chem.* **9**, 1871 (2002).

3. D. A. Perry, J. S. Cordova, L. G. Smith, H.-J. Son, E. M. Schiefer, E. Dervishi, F. Watanabe, and A. S. Biris *J. Phys. Chem. C*. **113**, 18304 (2009).

4. P. S. Rao and D. N. Sathyanarayana *Polymer*. **43**, 5051 (2002).

5. C. Goh, S. R. Scully, and M. D. McGehee *J. Appl. Phys.* **101**, 114503 (2007).

6. C. Hansch and A. Leo, *Substituent Constants for Correlation Analysis in Chemistry and Biology*, (Wiley, New York, 1979).

7. Y. He, C. Wu, and W. Kong *J. Chem. Phys.* **121**, 8321 (2004).

8. D. M. Mitchell, P. J. Morgan, and D. W. Pratt *J. Phys. Chem. A*. **112**, 12597 (2008).

9. T. Yoshida and S. Sawada *Bull. Chem. Soc. Jpn.* **49**, 3319 (1976).

10. M. Takara and A. S. Ito *J. Fluoresc.* **15**, 171 (2005).

11. T. Stalin and N. Rajendiran *Chem. Phys.* **322**, 311 (2006).

12. T. Stalin and N. Rajendiran *J. Photochem. Photobiol. A*. **182**, 137 (2006).

13. T. Stalin, B. Shanthi, P. V. Rani and N. Rajendiran *J. Inclusion Phenom. Macrocyclic Chem.* **55**, 21 (2006).

14. M. J. Frisch, G. W. Trucks, H. B. Schlegel, G. E. Scuseria, M. A. Robb, J. R. Cheeseman, J. Montgomery, J. A., T. Vreven, K. N. Kudin, J. C. Burant, J. M. Millam, S. S. Iyengar, J. Tomasi, V. Barone, B. Mennucci, M. Cossi, G. Scalmani, N. Rega, G. A. Petersson, H. Nakatsuji, M. Hada, M. Ehara, K. Toyota, R. Fukuda, J. Hasegawa, M. Ishida, T. Nakajima, Y. Honda, O. Kitao, H. Nakai, M. Klene, X. Li, J. E. Knox, H. P. Hratchian, J. B. Cross, V. Bakken, C. Adamo, J. Jaramillo, R. Gomperts, R. E. Stratmann, O. Yazyev, A. J. Austin, R. Cammi, C. Pomelli, J. W. Ochterski, P. Y. Ayala, K. Morokuma, G. A. Voth, P. Salvador, J. J. Dannenberg, V. G. Zakrzewski, S. Dapprich, A. D. Daniels, M. C. Strain, O. Farkas, D. K. Malick, A. D. Rabuck, K. Raghavachari, J. B. Foresman, J. V. Ortiz, Q. Cui, A. G. Baboul, S. Clifford, J. Cioslowski, B. B. Stefanov, G. Liu, A. Liashenko, P. Piskorz, I. Komaromi, R. L. Martin, D. J. Fox, T. Keith, M. A. Al-Laham, C. Y. Peng, A. Nanayakkara, M. Challacombe, P. M. W. Gill, B. Johnson, W. Chen, M.

W. Wong, C. Gonzalez, J. A. Pople GAUSSIAN 03, Revision C.02 (Gaussian, Inc. Wallingford, CT 2004).

15. J. R. Johnson, K. D. Jordan, D. F. Plusquellic, D. W. Pratt *J. Chem. Phys.* **93**, 2258 (1990).

16. W. A. Majewski, J. F. Pfanstiel, D. F. Plusquellic, and D. W. Pratt in *Laser Techniques in Chemistry,* edited by A. B. Myers and T. Rizzo, (Wiley, New York, 1995), p.101.

17. T. M. Korter, D. R. Borst, C. J. Butler, and D. W. Pratt *J. Am. Chem. Soc.* **123**, 96 (2001).

18. Y. He, C. Wu, and W. Kong *J. Phys. Chem. A*. **109**, 748 (2005).

19. D. F. Plusquellic, Ph.D. Thesis, University of Pittsburgh, 1992.

20. D. F. Plusquellic, R. D. Suenram, B. Mate, J. O. Jensen, and A. C. Samuels *J. Chem. Phys.* **115**, 3057 (2001).

21. N. Mataga *Bull. Chem. Soc. Jpn.* **36**, 654 (1963).

22. D. G. Lister, J. K. Tyler, J. H. Høg, and W. Larsen *J. Mol. Struct.* **23**, 253 (1974).

23. D. R. Borst, T. M. Korter, and D. W. Pratt *Chem. Phys. Lett.* **350**, 485 (2001).

24. C. L. Clements, J. W. Young, and D. W. Pratt *J. Phys. Chem. A*. **114**, 12005 (2010).

25. Avogadro: an open-source molecular builder and visualization tool. Version 1.0.0 http://avogadro.openmolecules.net/.

26. Jmol: an open-source Java viewer for chemical structures in 3D. Version 11.6.21 http://www.jmol.org/.

27. N. Mataga and T. Kubota, *Molecular Interactions and Electronic Spectra*, (Marcel Dekker, New York, 1970).

6.0 HIGH RESOLUTION ELECTRONIC SPECTROSCOPY OF THE DOORWAY STATES TO INTRAMOLECULAR CHARGE TRANSFER. GAS PHASE DIPOLE MOMENTS OF BENCHMARK AMINOBENZONITRILE DERIVATIVES.

Adam J. Fleisher, Ryan G. Bird, Daniel P. Zaleski, Brooks H. Pate, and David W. Pratt

AJF performed all high resolution electronic spectroscopy experiments, with the aid of the individuals listed in acknowledgements. RGB performed microwave spectroscopy experiments on PBN and fit the Stark microwave spectrum of DMABN. DPZ and BHP recorded the Stark microwave spectrum of DMABN at the University of Virginia. AJF and DWP wrote the paper.

6.1 ABSTRACT

Reported here are several of the ground, first, and second excited state structures and dipole moments of three benchmark intramolecular charge transfer (ICT) systems, 4-(1*H*-pyrrol-1-yl)benzonitrile (PBN), 4,4′-dimethylaminobenzonitrile (DMABN), and 4-(1-pyrrolidinyl)benzonitrile (PYRBN) as measured by rotationally resolved electronic spectroscopy in the gas phase. The related molecules 1-phenylpyrrole (PP) and 4-aminobenzonitrile (ABN) also are discussed. We find that the S_1 electronic state is of B symmetry for all five molecules in the gas phase. In PBN, a second excited state (S_2) of A symmetry is found only 400 cm^{-1} above the lowest frequency electronic transition observed in the vibrationally resolved fluorescence excitation spectrum. The change in dipole moment upon excitation to the A state is measured to be $\Delta\mu \approx 3.0$ D, significantly smaller than the value predicted by theory, and also smaller that observed for the 'anomalous' ICT band of PBN in solution. The B state (S_1) dipole moment of DMABN is 8.7 D, slightly smaller than that attributed to 'normal' LE fluorescence in solution. In contrast, the B state (S_1) dipole moment of PYRBN is large, with a value of 10.5 D. We also find the unsaturated donor molecules (PP, PBN) to be twisted in their ground states and to become more planar upon excitation, even in the A state (S_2), whereas the saturated donor molecules (DMABN, PYRBN), initially planar, potentially become more twisted in their excited states. It thus appears that whether or not a PICT or TICT model is appropriate to the ICT dynamics depends on the geometry of the ground state, at least when the properties of locally excited states are compared.

6.2 INTRODUCTION

In the gas phase, charge transfer requires communication between multiple potential energy surfaces on many time scales, the dynamics of which are inherently imprinted onto a neutral molecule in several detectable ways; *via* structural perturbations, changes in the energy ordering and overlapping of electronic states, and substantial increases in permanent electric dipole moments. In the isolated environment of a molecular beam, these surfaces are undisturbed by specific hydrogen bonding, van der Waals interactions, and bulk solvent electric fields that plague condensed phase determinations of structure and electronic distribution. The precise geometries of the excited states responsible for solvent-dependent dual fluorescence in many chromophores are unknown, and therefore the theories describing the nature of this phenomenon remain open for debate. To experimentally measure the excited state structures of representative dual fluorescent chromophores, we have employed high resolution electronic spectroscopy in the gas phase, a technique also capable of measuring the dipole moments of isolated molecules. Studies of this type on molecules of this size can be directly compared to high level theoretical predictions to ensure accuracy before the introduction of computationally expensive solvent models.

The specific donor-acceptor molecules under investigation here are 1-phenylpyrrole (PP), 4-(1*H*-pyrrol-1-yl)benzonitrile (PBN), 4-aminobenzonitrile (ABN), 4,4′-dimethylaminobenzonitrile (DMABN), and 4-(1-pyrrolidinyl)benzonitrile (PYRBN); see Scheme 6-1. With the exception of ABN,[1] each of these molecules exhibits dual emission upon electronic excitation in polar (sometimes even nonpolar) solvents, and their solvatochromic and thermochromic shifts in the condensed phase have been thoroughly explored by many authors.[2-9] The dual fluorescence of DMABN was initially attributed to emission from two excited

electronic singlet states, S_1 and S_2, one at shorter wavelength of B symmetry and another at longer wavelength of A symmetry (^1L_b and ^1L_a states, respectively).[2,10] Grabowski and coworkers later hypothesized, based on polarization experiments, that these two electronic states differed by a geometric distortion between donor and acceptor, referring to them as either the locally excited (LE) state or the twisted intramolecular charge transfer (TICT) state.[3,11] Evidence for the TICT state has been extensively reviewed by several authors,[12,13] most recently by Grabowski *et al*.[14] While not concerned directly with the molecular orbital symmetry of the excited states involved, the TICT model evokes the principle of minimum overlap to describe ICT states; a 90° twist of the donor relative to the acceptor occurs, which leads to electronic decoupling between donor and acceptor upon ICT, preventing the return of charge to the donor.

Scheme 6-1

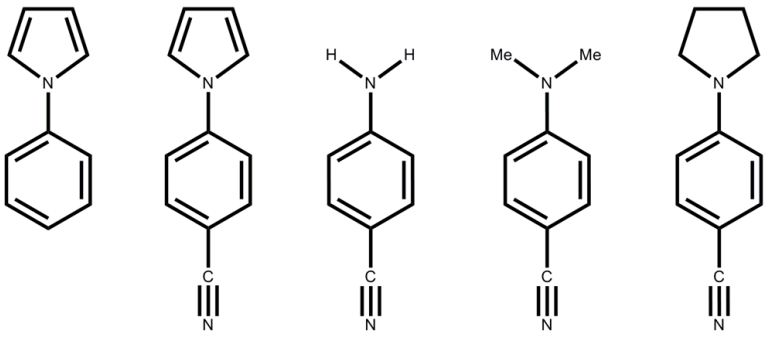

PP **PBN** **ABN** **DMABN** **PYRBN**

Zachariasse and coworkers have shown that a decrease in the energy gap between S_1 and S_2 allows access to important vibronic couplings between the two states, leading to efficient dual fluorescence upon excitation to S_1 in polar solvents.[15] In this vibronic coupling scheme, a planarization of the nitrogen-containing donor upon excitation is an important coordinate for

ICT, which leads to the existence of a planar ICT excited state. This is known as the PICT model. Recent work in the condensed phase community has focused on the photophysical properties of structurally hindered model compounds.[14,16-20] In these cases, analogs of many compounds, including PP, PBN, and DMABN, were synthesized with the twist degree of freedom removed, fixing the twist angle to either 0° or 90° by chemically linking the donor and acceptor moieties.

Previously, all five molecules have been studied in the collision-free environments of supersonic jets and beams, sometimes with rotational resolution, and occasionally in the presence of an applied electric field.[21-37] Additionally, the potential energy surfaces that govern charge transfer processes in many molecules of this type have been the subject of numerous theoretical investigations.[38-48] In this report, we describe high resolution microwave and UV experiments on PBN, DMABN, and PYRBN which provide new insights into the behavior of different donor-acceptor systems when they are excited by light. The determined data include the electronic structures of their ground and excited states, their geometries, and their permanent electric dipole moments; these data show that the S_1 state of each molecule is the ^1L_b state. In the case of PBN, we identify the S_2 state as ^1L_a, which is found only 400 cm^{-1} above the ^1L_b origin. Through a comparison of structural changes and charge reorganization that occur upon excitation, we report here clear differences in two classes of ICT compounds; those with unsaturated donors are less polar and become nearly planar in S_1 and S_2, while those with saturated donors are more polar and can become twisted even in S_1.

6.3 METHODS

High resolution electronic spectra of PBN, DMABN, and PYRBN were independently recorded in a cold molecular beam environment using an ultraviolet laser. The laser system, comprised of an Ar^+-pumped ring dye laser and external frequency doubling cavity, has been described elsewhere.[49-52] For PBN, rhodamine 590 (R6G) laser dye was used to create fundamental visible laser radiation, which was frequency doubled to the UV with a BBO crystal. The PBN experiments were recorded using an average laser power of 300 μW. For DMABN and PYRBN, mixtures of DCM and Kiton Red laser dyes were used to create the fundamental radiation. Again, a BBO crystal was used for frequency doubling, creating average output powers of 250 μW and 60 μW in the UV for DMABN and PYRBN, respectively. All experiments required a laser scan speed of 2000 s/cm^{-1} over a range of 4 cm^{-1} to obtain an acceptable signal-to-noise ratio. For DMABN, it was also necessary to record an additional 0.5 cm^{-1} section of several Stark spectra at the slower scan speed of 8000 s/cm^{-1}. Along with the fluorescence excitation spectrum (FES), the absorption spectrum of I_2 and frequency markers from a temperature stabilized etalon were recorded for absolute and relative frequency calibration using JBA95 acquisition software.[53] Both field-free and Stark spectra were analyzed manually using JB95 simulation software.[54]

Each sample required different source conditions to successfully seed a stream of argon backing gas. PBN was heated to 145 °C in a quartz source, and then expanded at a total backing pressure of 320 torr through a 200 μm pinhole into a vacuum chamber (10^{-5} torr). This supersonic expansion was skimmed while entering a second vacuum chamber (10^{-7} torr), creating the molecular beam. The collisionless molecular beam was crossed at a right angle by the UV laser, and total fluorescence following excitation was recorded by a PMT and photon

counting system mounted perpendicular to both the laser and molecular beam. Spherical mirrors and wire mesh Stark plates mounted above and below the intersecting beams were used to collect fluorescence and, when desired, create a homogenous electric field. In the PYRBN experiments, the sample was heated to 175 °C and expanded in argon at a total backing pressure of 455 torr. Both PBN and PYRBN were purchased from Maybridge (Thermo Fisher Scientific) and used without further purification. DMABN, purchased from Aldrich, was heated to 200 °C, and expanded in argon at a total backing pressure of 380 torr.

Microwave spectra of PBN were collected using the chirped-pulse Fourier transform microwave (CP-FTMW) spectrometer described previously.[55] PBN was heated to 120 °C and expanded through a pulsed nozzle at 10 Hz along with 1 ktorr of He backing gas. The entire spectrum was recorded from 6.5 – 17 GHz in 450 MHz segments, each of which was measured by collecting a 10 μs FID and signal averaging for up to 5000 shots. The segments were then patched together, and 120 μ_a-type transitions were assigned and analyzed using JB95 software.

The microwave Stark spectrum of DMABN was collected using a CP-FTMW spectrometer[56] containing a Stark cage.[57] DMABN was heated to 130 °C and expanded through 3 pulsed nozzles at 7 Hz with 760 torr Ne backing gas. The spectrum was recorded from 6.5 – 18.5 GHz at an applied electric field of 23.7 V/cm and signal averaged over 3.5×10^5 nozzle pulses. Individual line assignments were made in the QSTARK program,[58,59] and then simulated for visual comparison with experiment using JB95 software.

Theoretical work in support of the experiments was performed using GAUSSIAN 03 (Revision C.02) software[60] at the University of Pittsburgh Center for Simulation and Modeling (SAM). Ground state geometries were optimized using the M05-2X hybrid density functional with the 6-31+G* basis set. Dipole moments were then calculated using MP2/aug-cc-pVTZ on

the previously optimized geometries. For comparison with calculations available in the literature, complete active space self-consistent field (CASSCF) point calculations of PYRBN with an active space of 12 electrons and 10 orbitals (all π and π*) were done using the D95V basis set.[61] Only the relevant results of the CASSCF calculations are presented here, and further details are available in Appendix D.

6.4 RESULTS

6.4.1 4-(1*H*-Pyrrol-1-yl)benzonitrile (PBN)

Figure 6-1 shows the low resolution FES of PBN entrained in a supersonic jet previously observed by Belau *et al.*[33] It exhibits weakly fluorescent S_1-S_0 transitions, similar to the jet cooled spectrum of PP.[30,33] However, at energies only 400 cm^{-1} above the lowest frequency PBN band, a substantial increase in fluorescence is observed. This has been attributed to the influence of a second excited state (S_2) with greater fluorescence quantum yield than S_1.[33] To determine whether or not this explanation is correct, high resolution spectra were recorded of bands marked 1, 2, and 3 in Fig. 6-1, and these are shown in Figs. 6-2 through 6-4.

Band 1 is the lowest frequency electronic transition observed in the low resolution spectrum. Its relatively low fluorescence intensity was confirmed in our experiments. At high resolution, band 1 is actually comprised of two weak subbands of equal intensity, as seen in Fig. 6-2, labeled Band 1 red (lower frequency) and Band 1 blue (higher frequency) from this point forward. (As will be discussed later, the existence of two subbands in this spectrum provides evidence for a tunneling motion between two equivalent minima along the twisting coordinate of

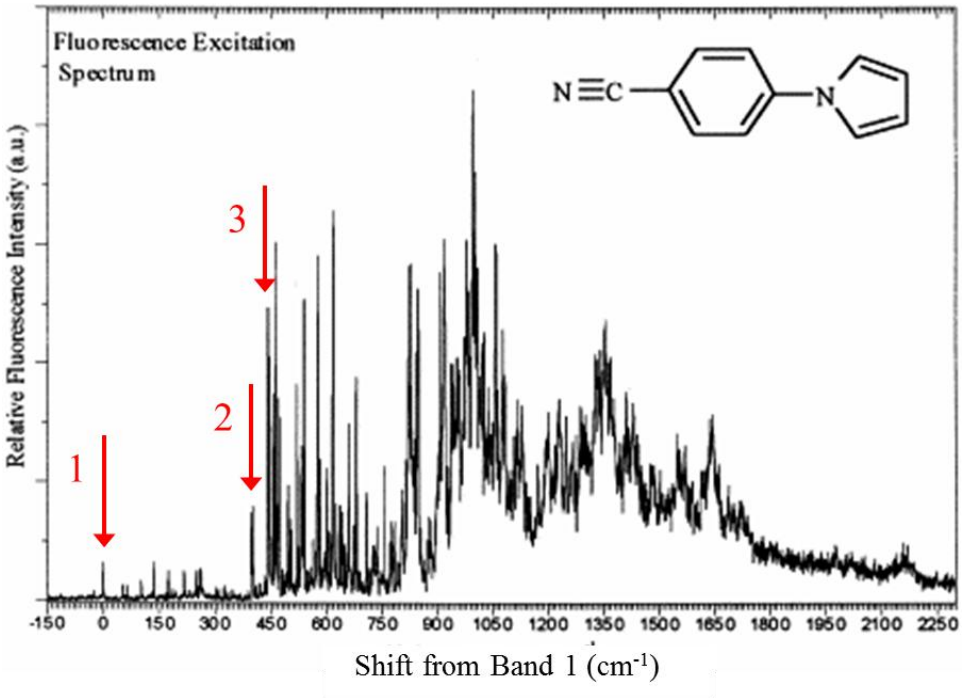

Figure 6-1. Vibrationally resolved fluorescence excitation spectrum (FES) of PBN. The red arrows labeled 1, 2, and 3 identify the bands studied using high resolution FES. Reprinted with permission from *Chemical Physics Letters* (Ref. 33). Copyright 2002 *Elsevier.*

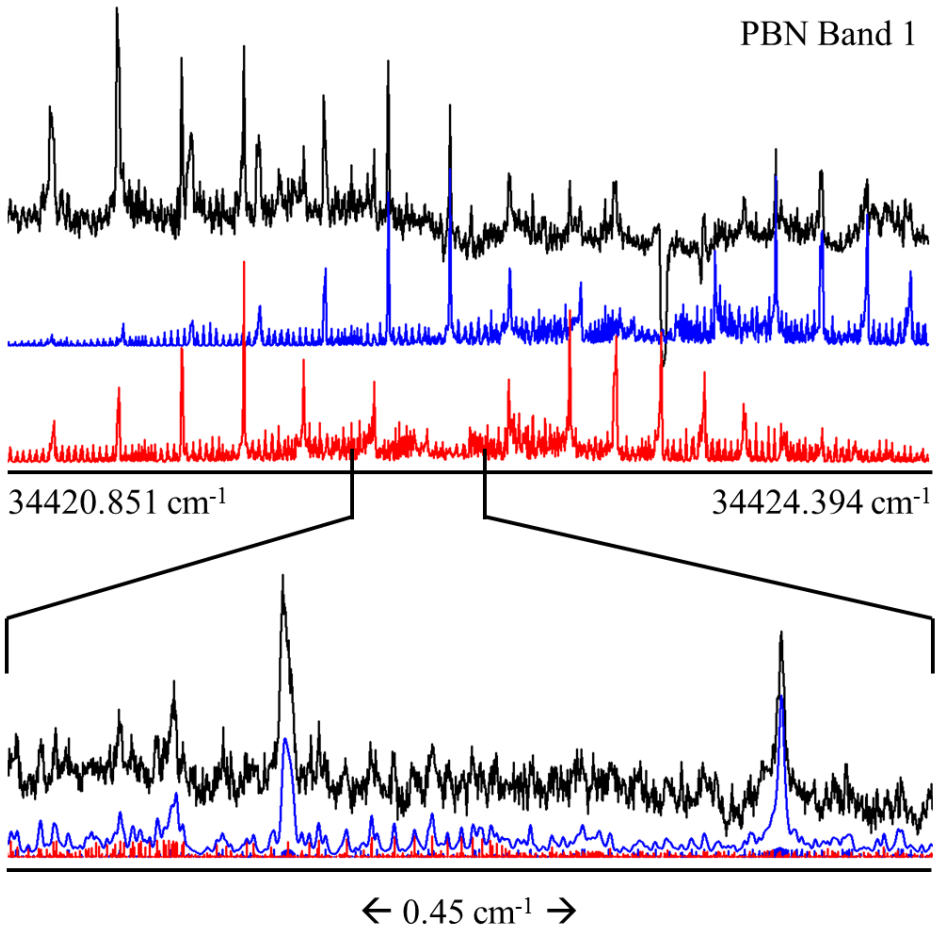

Figure 6-2. Rotationally resolved FES of PBN Band 1. The experimental trace shown in black was fit to two simulations, shown below in red and blue.

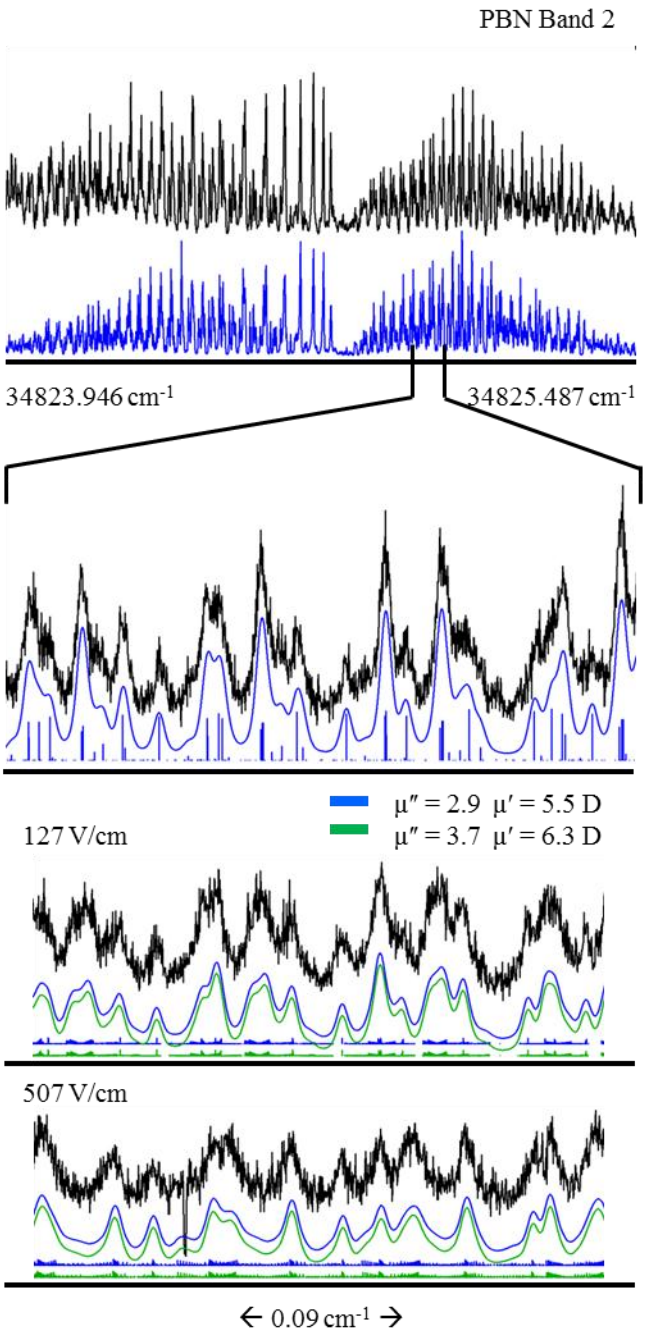

Figure 6-3. Rotationally resolved FES of PBN Band 2. The experimental trace shown in black was fit to a single simulation, shown in blue. The bottom two panels show the effects of an applied electric field on the high resolution spectrum. The blue and green simulations of the Stark spectra appear identical, therefore illustrating the difficulty encountered when trying to independently determine the EDM in each electronic state.

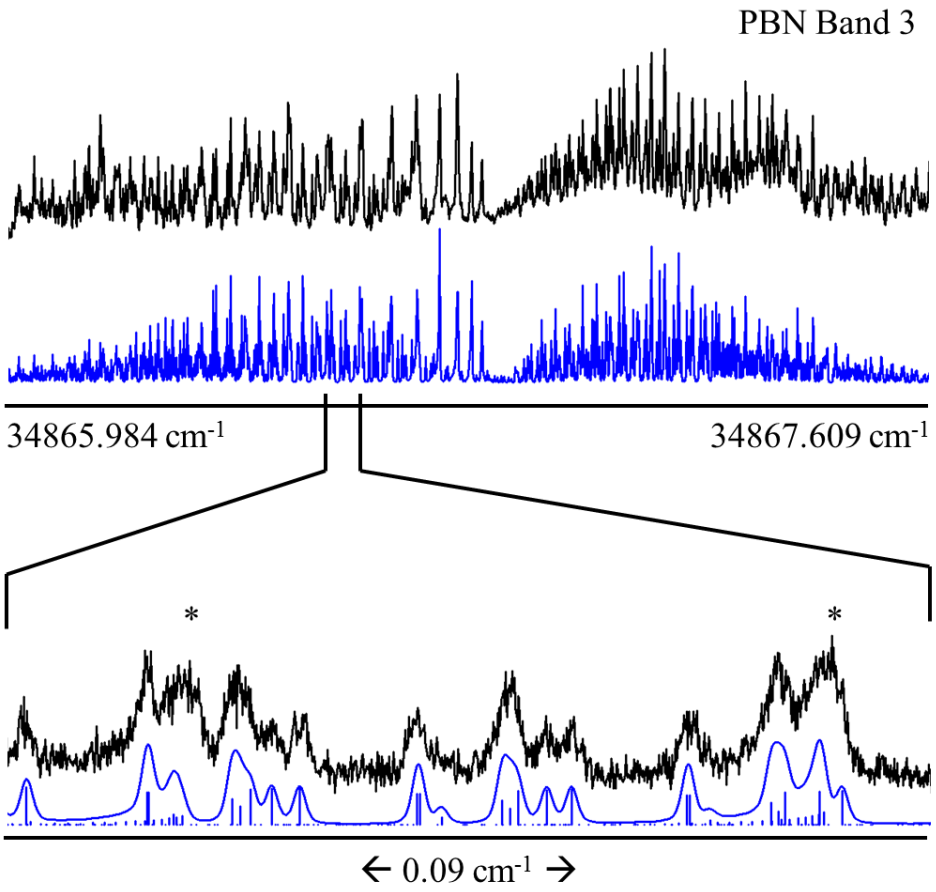

Figure 6-4. Rotationally resolved FES of PBN Band 3. The two asterisks identify areas of unassigned intensity found in the experimental spectrum (black trace) that are not accounted for by the simulation (blue trace). The presence of a second electronic band is suspected, as more of these "missing peaks" appear throughout the spectrum of PBN Band 3.

Table 6-1. Experimental inertial parameters derived from the microwave and UV spectra of PBN. Columns with the headings "Band 1", *etc*. contain the excited electronic state parameters of each respective transition studied in Fig. 6-1.

	S_0	Band 1 red	Band 1 blue	Band 2	Band 3
A (MHz)	3492.2(2)	3376.2(1)	3375.9(1)	3388.1(1)	3387.7(1)
B (MHz)	382.6028(4)	384.4(1)	384.5(1)	384.5(1)	384.5(1)
C (MHz)	349.9721(4)	346.8(1)	346.8(1)	346.9(1)	346.3(1)
ΔI (u$Å^2$)	-21.559	-7.04(8)	-6.90(9)	-6.70(1)	-4.50(1)
κ	-0.979	-0.975	-0.975	-0.975	-0.974
assigned lines	120	47	43	137	254
OMC (MHz)	0.032	6.2	7.1	3.8	6.3
origin (cm^{-1})		34422.559(1)	34423.352(1)	34824.753(1)	34866.829(1)
TM (*a*/*b*/*c*; %)		0/84/16	0/84/16	100/0/0	100/0/0
FWHM (L/G; MHz)		30/35	30/35	30/35	30/30

PBN.) In contrast, the rotationally resolved FES of PBN at +400 (Band 2) and +422 cm^{-1} (Band 3) consist of only single strong bands, as shown for Band 2 in Fig. 6-3. These data were analyzed using the following procedure. First, anticipating that the near-prolate symmetric top nature of PBN would limit the accuracy of the *a*-type electronic spectral analysis, ground state rotational constants of PBN were determined from a fit to Watson's A-reduced Hamiltonian[62] of an independently measured microwave spectrum (see Appendix D). Next, excited state rotational constants of PBN were determined from fits to rigid-rotor Hamiltonians of the observed rotational structure in each of the spectra in Figs. 6-2 through 6-4 using the program JB95. In these fits, ground state constants were kept fixed to their microwave values, and excited state constants were varied in a least-squares fashion to minimize differences between observed and calculated frequencies. More than 40 resolved transitions were fit in the electronic spectra of Band 1, and more than 130 rotational transitions were fit in the electronic spectra of Bands 2 and 3. The combined microwave and high resolution FES data for all observed PBN bands are summarized in Table 6-1.

To aid in the determination of molecular structure from the measured inertial parameters, the S_0 geometry of PBN was optimized using M05-2X density functional theory and the 6-31+G* basis set. The rotational constants of the optimized structure (A = 3508.2, B = 383.3, and C = 351.7 MHz) are in good agreement with the microwave values listed in Table 6-1. Notably, this structure has a large negative inertial defect, ΔI = -21.559 u$Å^2$, which decreases substantially in magnitude when PBN is excited by light, to values of ~ -7 u$Å^2$ in Bands 1 and 2 and ~ -5 u$Å^2$ in Band 3. Figure 6-5 shows a plot of ΔI *vs.* ϕ as calculated by DFT (see Appendix D for details). This plot reveals that ground state PBN is twisted about the bond connecting the two rings by an equilibrium angle of 32°, and that the corresponding twist angles in the excited state(s) are 14° in

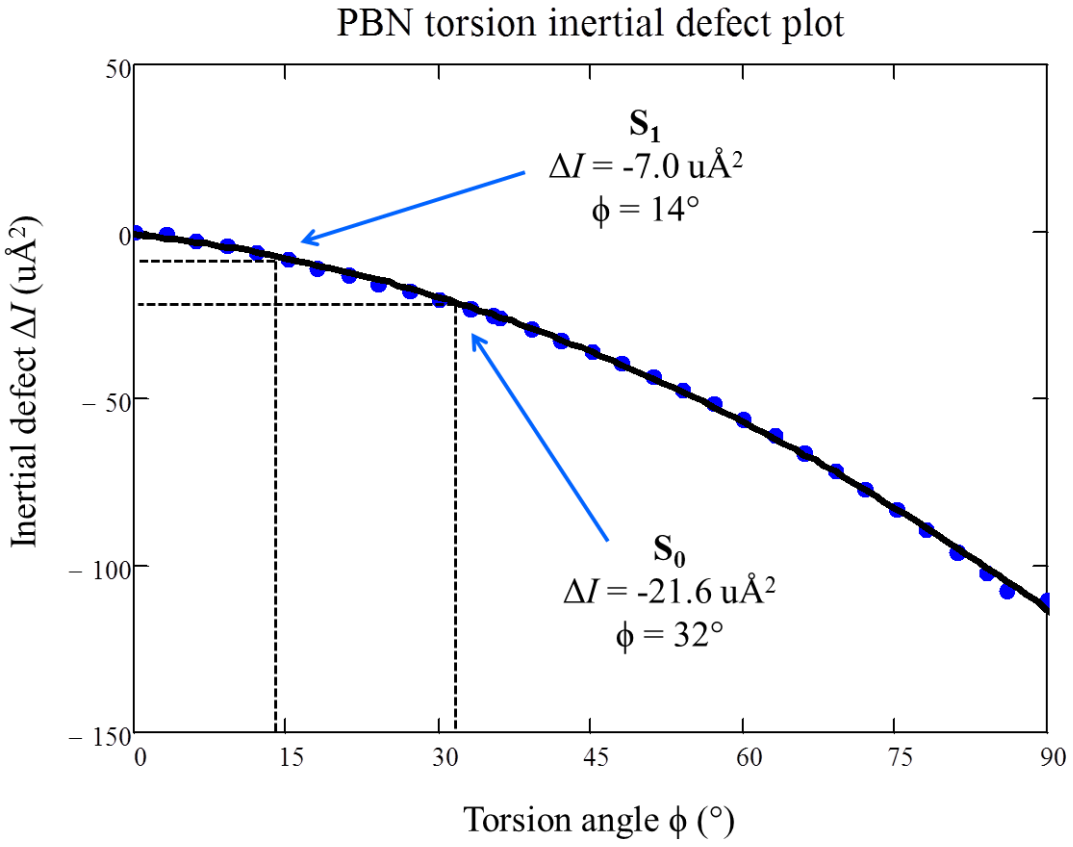

Figure 6-5. Plot of ΔI *vs.* ϕ as calculated from the ground state torsional PES shown in Fig. D-4 (blue data points). These data points were fit to a 2nd order polynomial (black curve), and used to determine ϕ for all PBN electronic states. The S_0 and S_1 extrapolations are shown in the figure.

Band 1, 13° in Band 2, and 9° in Band 3. The theoretical barrier to ring planarity at $\phi = 0°$ is $V''(0) = 469$ cm^{-1}, whereas the barrier to ring perpendicularity at $\phi = 90°$ is $V''(90) = 1003$ cm^{-1}. We believe that the splitting found in Band 1 is a consequence of hindered internal rotation about the bond connecting the two unsaturated rings in the excited S_1 state, resulting from a decrease in one or both of the barrier heights mentioned above.

The second significant result on PBN is the detection of the origin of the S_2 state. Recall that PBN exhibits increased fluorescence intensity at about 400 cm^{-1} above Band 1, in the vicinity of Bands 2 and 3. We find that the electronic transition moment (ETM) in (both subbands of) Band 1 lies close to the *b* inertial axis, since this band is a hybrid band with 84% *b* character and 16% *c* character; see Table 6-1. In contrast, Bands 2 and 3 are 100% *a*-type; the ETMs of these bands are parallel to the *a* inertial axis, the long axis of PBN. The observation of this change in the ETM with increasing excitation energy confirms the proposal of Belau *et al.*[33] that a second electronic state is responsible for the increased fluorescence intensity at ~ 400 cm^{-1} above the origin of the S_1 state. We therefore assign Band 1 as an excitation to the ^1L_b state, and Bands 2 and 3 as excitations to the ^1L_a state. The ^1L_a electronic state is often considered to be the state responsible for charge transfer in polar solvents. The existence of *c*-type transitions in Band 1 is a result of the benzene ring lying out of the *ab* inertial plane by a vibrationally averaged angle τ of approximately 23° ± 3° (where $\tan\tau = \sqrt{c/b}$), similar to that observed previously in the case of PP.[37]

Given the difference in the electronic nature of the ^1L_a and ^1L_b states, it was of interest to measure the difference in their permanent electric dipole moments (EDMs) using an external electric field. The experimental Stark spectra of both Bands 2 and 3 were recorded over a range of 42 to 507 V/cm and fit with several effectively identical simulations, as seen for the case of

Band 2 in Fig. 6-3. A high linear correlation was observed between the ETMs of the two electronic states, owing to the fact that only *a*-type rovibronic transitions were observed. An analysis of this correlation (see Appendix D) shows that by fixing the ground state value of the EDM to the theoretical value of 3.43 D, the best excited state values are $\mu'(^1L_a)$ = 6.02(10) D for band 2, and $\mu'(^1L_a)$ = 6.33(10) D for Band 3. Unfortunately, owing to the low fluorescence intensity, the excited state value for Band 1 could not be measured; the calculated value for the ^1L_b state is 2.8 D.[44]

6.4.2 4,4′-Dimethylaminobenzonitrile (DMABN)

Similar experiments were performed on DMABN. In this case a different strategy was used for their analysis because the rotationally resolved electronic spectra are extremely congested, owing to multiple overlapping torsional subbands that result from methyl group torsional motions.[36] Thus, CP-FTMW experiments were first performed to study the microwave spectrum of DMABN in the gas phase; the results of these measurements, which include a substitution structure by detection of all ^{13}C and ^{15}N isotopologues in natural abundance, are reported elsewhere.[63] Next, the microwave spectrum of DMABN was recorded again in the presence of an electric field, generated using the parallel-plate configuration of a Stark cage; see Appendix D for a typical example and a listing of all line assignments. A fit of 78 rotational transitions by linear least squares yields a value of μ'' = 6.426(30) D for the ground state EDM of DMABN in the gas phase. Then, the rotationally resolved electronic spectrum of Band 5 in the S_1-S_0 transition of DMABN[36] was recorded at applied electric fields ranging from 42 to 846 V/cm. Figure 6-6 shows a typical example, the entire spectrum recorded over ~ 3.4 cm^{-1} at an applied electric field of 507 V/cm. As is apparent, the assignment of individual rotational transitions was

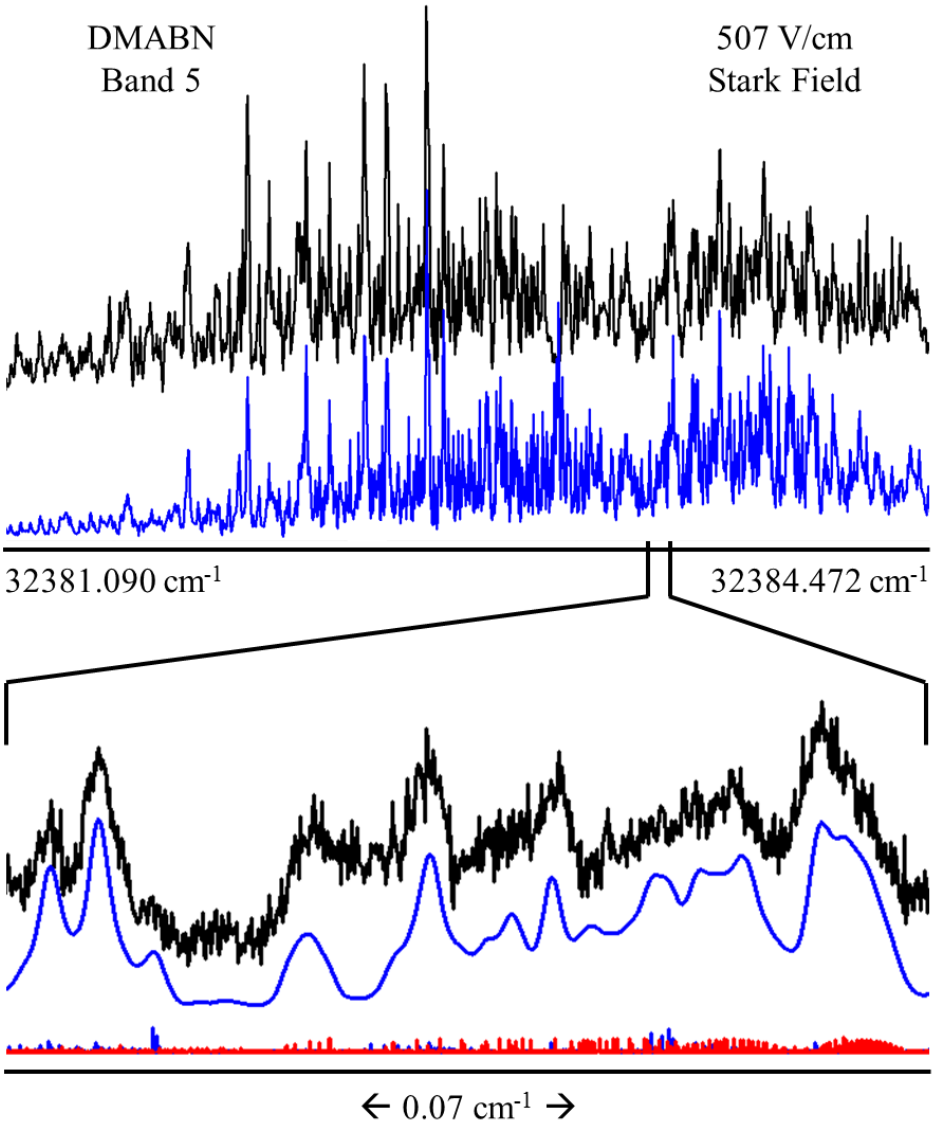

Figure 6-6. Rotationally resolved FES of DMABN (Band 5) recorded at an applied electric field of 507 V/cm. The experimental trace is shown in black, and the combined simulation of both *A* (blue sticks) and *G* (red sticks) subbands is shown in blue.

nearly impossible in this spectrum, owing to the extreme congestion. However, a few moderately well resolved lines could be followed within the *A* subband of this spectrum (blue sticks in Fig. 6), leading to the assignment of 29 transitions. While holding μ″ fixed to its ground state value of 6.426 D, a least squares fit of these transitions to experiment produced a value of μ′ = 8.719(20) D for the electronically excited state, with an OMC = 12.4 MHz (well below the experimental line width of about 55 MHz). The same EDMs were then used to simulate the *G* subband (red sticks), and a convolution of the *A* and *G* subbands which includes line width contributions from Gaussian (30 MHz) and Lorentzian (35 MHz) broadening is shown for comparison with the experimental trace (black). As in the earlier experiments,[36] the *E* subband that must also be present in these spectra was not included in the simulations.

6.4.3 4-(1-Pyrrolidinyl)benzonitrile (PYRBN)

The low resolution FES of PYRBN is fundamentally different from those observed for the phenylpyrroles.[26,27] The lowest frequency band in PYRBN (the S_1-S_0 origin) is the most intense transition in the entire spectrum, and the strong low frequency vibrational progressions that appear in the corresponding spectra of the phenylpyrroles are absent. Clearly, the energy separation of the S_1 and S_2 states, and perhaps their identities as well, must be very different in PYRBN.

High resolution FES of PYRBN were recorded to explore this issue. Figure 6-7 shows the entire recorded spectrum of the origin band at ~ 312 nm which spans approximately 3 cm^{-1}. Exactly 200 rotational transitions in the resolved spectrum were assigned using pure *b*-type selection rules, and fit in a linear least squares fashion to the experiment. Table 6-2 reports the

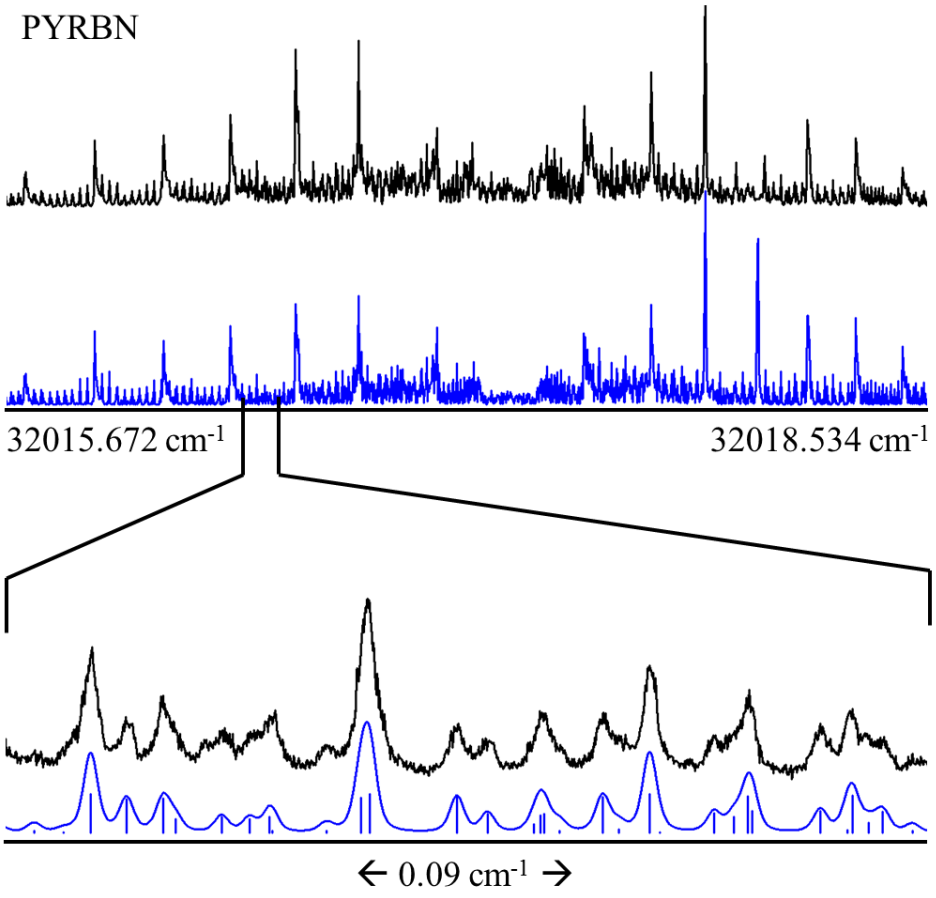

Figure 6-7. Rotationally resolved FES of PYRBN. The experimental trace is shown in black, and the simulation is shown in blue.

Table 6-2. Experimental inertial parameters derived from the UV spectrum of PYRBN.[a]

	S_0	S_1
A (MHz)	3083.0(1)	3005.7(1)
B (MHz)	366.1(1)	367.2(1)
C (MHz)	331.8(1)	331.7(1)
ΔI (uÅ^2)	-21.13(5)	-20.82(5)
κ	-0.975	-0.973
assigned lines	200	
OMC (MHz)	2.9	
origin (cm^{-1})	32017.232	
TM (*a*/*b*/*c*; %)	0/100/0	
FWHM (L/G; MHz)	20/30	

[a]S_0 inertial parameters calculated at the M05-2X/6-31+G* level are: *A* = 3097.6, *B* = 366.7, and *C* = 332.3 MHz; ΔI = -20.5 uÅ^2; κ = -0.975.

rotational constants and electronic origin frequency, among other parameters, determined from this fit. As clearly indicated by the observed *b*-type selection rules, the gas phase S_1 state of PYRBN is assigned as the ^1L_b state.

The ground state inertial defect ($\Delta I''$) derived from the experimentally determined rotational constants of PYRBN is -21.1 uÅ^2, qualitatively similar to the $\Delta I''$ values of PP[37] and PBN (-26.9 and -21.6 uÅ^2, respectively). However, the reason for this similarity is not the same as that found in PP and PBN. In PYRBN, the saturated pyrrolidine ring is puckered, resulting in heavy atom positions above and below the phenyl ring plane. This saturated ring nonplanarity results in a large negative $\Delta I''$. In contrast, the similar $\Delta I''$ values in PP and PBN are due to substantial twisting between the unsaturated rings in the phenylpyrroles. (Comparatively, the inertial defect of the equatorial conformer of pyrrolidine as determined from its rotational spectrum in a supersonic jet is -18.5 uÅ^2.[64]) Also, no *c*-type transitions were found in the spectrum of PYRBN. Their presence in the S_1-S_0 spectra of PP and PBN are a clear indication of significant ring torsion in the vibrationally averaged structures of those systems, something not present in the spectra of PYRBN. The calculated twist angle of PYRBN predicted by hybrid DFT (M05-2X/6-31+G*) is 6° in the ground state, small compared to the phenylpyrroles, and the associated theoretical rotational constants are A = 3097.6, B = 366.7, and C = 332.3 MHz.

Very little change in the B or C rotational constants is observed on excitation of PYRBN, whereas a small decrease in A (due to benzene ring expansion upon excitation) was measured. (This also accounts for the very symmetric nature of its high resolution spectrum, Fig. 6-7.) More telling is the nearly identical ΔI measured for each electronic state; $\Delta I''$ = -21.1 and $\Delta I'$ = -20.8 uÅ^2, respectively. Clearly, there is little or no change in twist angle for the pyrrolidine ring relative to the benzonitrile ring upon excitation to the $S_1(L_b)$ state in PYRBN, as this would

significantly increase (in magnitude) the measured inertial defect relative to S_0. This is different from the geometric changes observed in both PBN and DMABN upon excitation,[36] the reasons for which will be discussed later.

Stark effects measurements also were made on PYRBN. Independent simulations and linear least squares fits of spectra taken in electric fields ranging from 85 to 423 V/cm yield the following measured EDMs; $\mu'' = 8.23(3)$ and $\mu'(L_b) = 10.52(3)$ D, entirely along the *a* inertial axis of PYRBN.

6.5 DISCUSSION

Through the use of high resolution microwave and electronic spectroscopy, the S_0 and S_1 geometries of PP,[37] PBN, ABN,[29] DMABN,[36] and PYRBN in the gas phase have all been determined. Importantly, the lowest lying electronic state is of 1^1B symmetry (the ^1L_b state) for all five molecules. However, while the S_1-S_0 electronic transitions to the 1^1B state involve the same (by symmetry) molecular orbitals, the geometric consequences of such an excitation can be quite different, depending on the nature of either the donor or acceptor. In both PP and PBN, the donor group is pyrrole, which in solution at least, is not a very good electron donor (pK_a = -3.8).[65] Both of the pyrrole derivatives exhibit a pretwist in S_0, which is measured as $\phi'' = 36°$ for PP (see Appendix D) and $\phi'' = 32°$ for PBN. As evidenced by the abundance of low frequency Franck-Condon (FC) progressions in the vibrationally resolved FES of both pyrrole derivatives, the minimum energy geometries in S_1 must be considerably different than those found in S_0.[30,33,37] We find here by measuring the inertial parameters of PP and PBN in both S_0 and S_1, that both molecules become more planar upon electronic excitation. In PP, $\phi' = 20°$ when eight

quanta of the torsion mode are excited; the twist angle at the zero-point vibration level must be less than 20°, as exciting higher quanta of the torsion in S_1 should lead to larger twist angles. In PBN band 1, $\phi' = 14°$ is found for the tentatively assigned electronic 1^1B origin. For both pyrrole derivatives, we have therefore measured remarkable changes in the ring twist angle upon excitation to the 1^1B states of $\Delta\phi = -16°$ and $\Delta\phi = -18°$, respectively. This energetic preference for a more planar structure must arise from improved conjugation between the ring π systems upon excitation, resulting also in an increase in the π-bond order of the bond connecting the two conjugated rings.

While the addition of a cyano group to the electron accepting benzene ring does not appear to significantly alter the preferred 1^1B geometry of the pyrrole derivatives, it does significantly lower the energy of the second excited state, which is of 2^1A symmetry. At excitation energies only 400 cm^{-1} above the presumed PBN origin, the 2^1A electronic surface perturbs the observed electronic transitions to such an extent that a 90° rotation of the ETM is observed in the rotationally resolved FES, from *b*-type to *a*-type. Clearly, the energy gap $\Delta E(S_1,S_2)$ is smaller for PBN than for PP in the gas phase, as no large increase in fluorescence intensity at higher excitation frequencies was observed for PP.[21] The 2^1A state is more planar than both the ground and first excited states of PBN, with a lower twist angle of merely $\phi' = 9°$, yielding a decrease in twist angle upon excitation to S_2 of $\Delta\phi' = -23°$. The planarity of 2^1A measured in the gas phase corresponds well with the calculated structure of the quinoidal form of 2^1A, termed $2^1A(Q)$.[41,44] We hypothesize that the $2^1A(Q)$ state identified here as the low-lying excited S_2 state of PBN is responsible for the red emission observed in argon matrix experiments[66-68] and acetonitrile clusters formed in a supersonic jet.[35]

When local π system conjugation within the donor moiety is lost, the pretwist between donor and acceptor is suppressed, as was found in the ground states of ABN, DMABN, and PYRBN. Instead, a large amount of electron density (*i.e.*; a lone pair) is localized on the nitrogen atom of the amino group in ABN and DMABN, giving rise to non-zero inversion angles (analogous to the sp^3 hybridization invoked to rationalize the pyramidal structure of ammonia). However, the optimized S_0 geometry of PYRBN (M05-2X/6-31+g*) has a locally planar NR_2 arrangement, with a small twist angle relative to the benzonitrile ring of $\phi'' = 6°$. No pretwist is observed in ABN and DMABN; the ground state inversion angles of these two molecules are reported as 34° (Ref. 29) and 14.6° (Ref. 63), respectively.

The charge density localized on the donor amino nitrogen in the ground state is transferred, at least in part, to the benzonitrile acceptor in all three cases upon excitation to the 1^1B state. However, this results in a measured change to the vibrationally averaged amino inversion angle upon excitation only for the case of DMABN. In ABN, the change in inversion angle is negligible, as indicated by the nearly identical inertial defects measured in each electronic state.[29] In contrast, the dimethylamino group of DMABN rearranges into a planar geometry along the inversion coordinate, and the entire donor group twists to an angle of $\phi' = 25°$, placing one methyl group above, and another methyl group below the benzonitrile plane. By allowing this twist, the dimethylamino group is able to stabilize a larger charge separation than in the case of ABN, which weakens the N-CH_3 bonds in S_1 relative to S_0, and decreases the barrier to internal rotation of the individual methyl groups.[36] A clear low frequency FC progression is observed in the vibrationally resolved FES of DMABN which is explained by the existence of unique geometries in S_0 and S_1. In PYRBN, no change in twist angle is observed in S_1, as indicated by the nearly identical inertial defects measured for each electronic state. The absence

of low frequency activity in the vibrationally resolved FES of PYRBN is additional proof of little change in geometry upon excitation to 1^1B.[26]

The consequences of increased or decreased donor-acceptor conjugation are further explored by measuring the permanent EDMs of each compound. The center of negative charge in the ground state of PP lies within the pyrrole ring, as evidenced by the orientation and magnitude of its permanent dipole, $\mu'' = -1.56(1)$ D.[37] Replacing the benzene ring in PP with the benzonitrile ring in PBN results in a change in both the magnitude and direction of its permanent EDM, $\mu'' = 3.34$ D [a consequence of the larger dipole of benzonitrile itself ($\mu'' = 4.48$ D)[32]], again demonstrating the electron withdrawing capabilities of pyrrole. Upon excitation to the 1^1B state, the dipole of PP decreases in magnitude to $\mu' = 0.94(1)$ D, but reverses its vector direction, as the center of negative charge now lies on the benzene ring acceptor. In contrast, the dipole of PBN increases in magnitude to $\mu' = 6.02(10)$ D with no change in direction. Taking the signs into account we see that the differences in the EDMs of the two states of PP and PBN are about the same, 2.50 and 2.59 D. The largest measured value of the EDM of PBN is that for the 2^1A state, $\mu' = 6.33(10)$ D. Even with the increase in spatial overlap between the π systems of each ring in the pyrrole derivatives, charge is still moving from the donor to acceptor, which results in an increase in negative charge on the benzene or benzonitrile moieties, respectively.

The largest effect of π system conjugation, the sharing of electrons over the entire molecule, is made clear upon inspection of the μ_a dipoles measured for ABN,[32] DMABN, and PYRBN. The ground state EDMs of all three molecules with saturated donor groups are large: $\mu'' = 6.41$ D for ABN,[32] $\mu'' = 6.43$ D for DMABN, and $\mu'' = 8.24$ D for PYRBN, much larger than those for PP and PBN. Evidently, extended conjugation decreases their ground state dipoles, relative to their saturated-donor counterparts. Within the saturated-donor family, PYRBN has the

largest μ″, consistent with the geometric finding that its inversion angle of 0° (and therefore the amount of electron density on the donor nitrogen) is less than in DMABN (14.6°) or ABN (34°). More electron density from the donor nitrogen is already present in the benzonitrile ring of PYRBN than in ABN or DMABN, which also necessitates a small but non-zero twist angle in the ground state of PYRBN.

Upon excitation to $S_1(1^1B)$, the excited state μ_a EDMs of these three molecules are quite different. In ABN, $\mu' = 7.20$ D, a small change upon excitation of $\Delta\mu = 0.79$ D.[32] While the ground state EDMs of ABN and DMABN are effectively equal, the excited state EDM of DMABN is $\mu' = 8.72$ D, significantly larger than that found in ABN. For DMABN, $\Delta\mu = 2.29$ D for excitation to the 1^1B excited state. For PYRBN, the largest excited state EDM is found, with a measured value of $\mu' = 10.52$ D. However, the change in dipole upon excitation is nearly identical to that of DMABN, at $\Delta\mu = 2.28$ D. In the case of ABN, some projection of the total EDM remains on the *c* inertial axis in S_1, partially explaining the small $\Delta\mu$ observed relative to DMABN and PYRBN. However, the fact that the NH_2 donor does not reach planarity upon excitation shows that a smaller amount of charge is transferred to benzonitrile in ABN than in the other two cases. In both DMABN and PYRBN, a twist exists in S_1. While more dramatic in DMABN, the change in dipole moment upon excitation is the same as in PYRBN, suggesting that electronically, the 1^1B states of these two molecules are very similar. When little or no twist exists in the ground states of the saturated donor molecules, the twist angle either remains the same or increases in their excited states. Scheme 6-2 summarizes the dipole moments (in units of Debye) and twist angles of the $S_1(1^1B, {}^1L_b)$ states of all five molecules considered in this work.

The EDMs of both ABN and DMABN have been previously measured in solutions of cyclohexane, benzene, and 1,4-dioxane using time-resolved microwave conductivity (TRMC)

Scheme 6-2

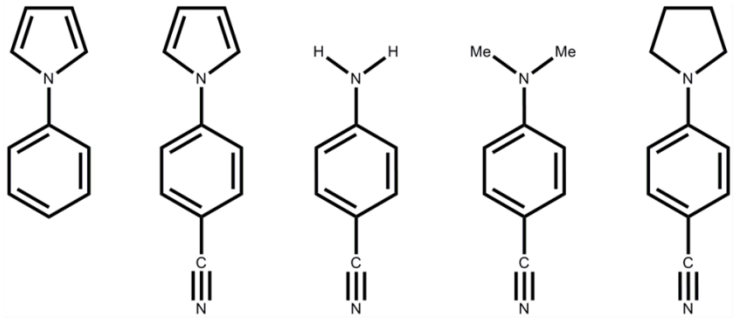

and fluorescence spectroscopy techniques.[69] There, the ground state dipole moment of 6.6 D determined for both ABN and DMABN is in good agreement with the gas phase data. In the S_1 state, the EDMs were measured to be 8.3 D for ABN and 9.9 D for DMABN. These S_1 EDMs are larger than the corresponding gas phase values by 1.1-1.2 D. The authors claim[69] that each S_1 dipole measured by TRMC is an upper limit to the EDM of the isolated molecule, particularly in the case of DMABN, where the first excited state is hypothesized to be increasingly influenced by the onset of a higher excited state as solvent polarizability and polarity is increased. Using the same $\mu'' = 6.6$ D determined in Ref. 69, the S_1 EDM of DMABN was also determined by measuring the electric field-induced changes in absorption and emission spectra in a polymer film of PMMA.[70] There, the excited state EDM of DMABN also was overestimated by more than 1 D, with a reported value of 9.8-10 D.

The low lying electronic surfaces of these donor-acceptor molecules have been well-studied by various theoretical methods. The highest level *ab initio* work available in the literature

for these compounds exists only for DMABN, where the resolution-of-the-identity coupled-cluster singles-and-doubles method RI-CC2 was employed using a triple-ζ valence basis set TZVPP by Köhn and Hättig.[42] Here, the relaxed geometries of three states were optimized: the ground 1^1A state, the 1^1B state, and the 2^1A state. The ground state was predicted to have an amino inversion angle of 23° and a dipole moment of $\mu'' = 7.4$ D, both in modest agreement with gas phase data of 14.6° (Ref. 63) and $\mu'' = 6.4$ D. Predictions for the 1^1B state also are in modest agreement with experiment, where the inversion angle is now 0° and a slight twist of the dimethylamino group was calculated to be $\phi' = 19°$. The predicted dipole moment of $\mu' = 10.1$ D is larger than the experimental value of $\mu' = 8.7$ D. Thus, the RI-CC2 calculations do a reasonable job of reproducing the experimentally determined quantities of DMABN in both S_0 and S_1. Their prediction of a twisted ($\phi' = 90°$) 2^1A state therefore seems very plausible.

Several theoretical investigations using relaxed CASSCF excited state geometries and subsequent single-point CASPT2 calculations have been reported,[38,39] and recently have focused on the importance of quinoidalization to ICT phenomenon.[41,44] In DMABN, ICT is generally understood to arise from a twisted ($\phi' = 90°$) 2^1A state. However, in the pyrrole derivatives PP and PBN, two ICT states were predicted, one planar and one twisted. The authors conclude that both PICT and TICT may be possible in the pyrrole derivatives, owing to the existence of an additional donor orbital within the π system of pyrrole. In the case of PBN, experiment clearly shows that a planar minimum exists on the 2^1A surface, corresponding to the 2^1A(Q) structure predicted in the above-mentioned work. However, we see no experimental evidence for a second minimum of the 2^1A(AQ) variety, predicted to possess a larger dipole moment which would be further stabilized as an ICT state in solution. A comparison between theory and experiment is made in Table 6-3.

Although DFT methods offer a significant reduction in computational cost relative to *ab initio* theories, improving their predictive success for relaxed geometries in excited electronic states is still an active area of research.[71] Very recently, the inability of standard DFT methods to accurately calculate the potential energy surfaces of excited states has been addressed by Wiggins *et al*.[46] using a Coulomb-attenuated functional approximation (CAM-B3LYP). This promising method, performed only on DMABN up to this point, also should be tested on the potential energy surfaces of other charge transfer systems with experimental and theoretical data readily available in the literature, such as those reported here.

6.6 SUMMARY

The transformation of a reactant molecule into a product molecule in intramolecular charge transfer (ICT) processes can span several different potential energy surfaces (LE, ICT, *etc*.); and the connections between them also can involve conical intersections along different vibrational coordinates. But all of these surfaces support molecular eigenstates to which contributions are made from the different canonical structures. Thus, studies of the electronic spectra of doorway states to ICT at high resolution can provide information about these dynamics despite the fact that such spectra are "vertical", and obey the Franck-Condon principle, since rotational motion is typically slow compared to the time scales of interconversion.

The present study reveals new information about such processes in a family of 4-aminobenzonitriles, absent the perturbations produced by neighboring solvent molecules. We

Table 6-3. Permanent electric dipole moments and twist angles of PP, PBN, ABN, DMABN, and PYRBN measured in the gas phase (first row). Standard deviation is shown in parentheses. Also listed are the available theoretical data for each electronic transition observed (Refs. 41 and 44), second row.

	μ'' (D)	μ' (D)	$\Delta\mu$ (D)	ϕ'' (°)	ϕ' (°)	$\Delta\phi$ (°)
PP[a]	-1.56(1)	0.94(1)	+2.50(1)	36	20	-16
$1^1B(LE) - 1^1A$	-1.9	0.1	+2.0	36.8	19.4	-17.4
PBN band 1	--	--	--	32	14	-18
$1^1B(LE) - 1^1A$	3.5	2.8	-0.7	36.5	36.3	-0.3
PBN band 2[b]	3.43	6.02(10)	+2.6(1)	32	13	-19
PBN band 3[b]	3.43	6.33(10)	+2.9(1)	32	9	-23
$2^1A(Q) - 1^1A$	3.5	10.6	+7.1	36.5	0	-36.5
ABN[c]	6.41(3)	7.20(3)	+0.79(4)	0	0	0
$1^1B(LE) - 1^1A$	6.2	6.0	-0.2	0	0	0
DMABN[d]	6.43(3)	8.72(2)	+2.29(4)	0	25	+25
$1^1B(LE) - 1^1A$	6.5	7.0	+0.5	0	0	0
$1^1B(AQ) - 1^1A$	6.5	14.8	+8.3	0	90	+90
PYRBN	8.23(3)	10.52(3)	+2.29(4)	6	6	0
$1^1B(LE) - 1^1A$[e]	7.4	10.4	+3.0	0	0	0

[a] μ data from Ref. 37

[b] μ'' calculated using MP2/aug-cc-pVTZ//M05-2X/6-31+G* theory, and μ' calculated from the appropriate experimentally derived dipole function (see Appendix D).

[c] Data from Ref. 32.

[d] ϕ data from Ref. 36.

[e] Data not available in the literature. Calculated here for both electronic states at the CASSCF(12,10)/D95V//M05-2X/6-31+G* level.

have measured the rotationally resolved electronic spectra of PBN, DMABN, and PYRBN in the presence of an electric field. These measurements, along with several supporting microwave spectroscopy experiments, provide the moments of inertia of each molecule in their ground and excited states, as well as their gas phase permanent electric dipole moments in both electronic states. Thereby probed are the differences in the equilibrium geometries of the two states, and the changes in charge distribution that are responsible for them.

We find that excitation of PP and PBN by light changes their structures from twisted ones to more planar ones, whereas excitation of ABN and PYRBN by light has little effect on their structures. In contrast, DMABN twists upon excitation by light, and becomes more planar at the amino nitrogen. Despite these differences, the changes in electron distribution in all five molecules are about the same; $\Delta\mu$ = 2.0 – 2.5 D in PP, PBN, DMABN, and PYRBN. Only in ABN is $\Delta\mu$ smaller; $\Delta\mu$ appears to be larger in the ^1L_a state of PBN. The excited state permanent electric dipole moments of molecules containing *para* cyano groups are substantially larger than those without them; these change by more than an order of magnitude on going from PP to PYRBN. Thus, whether or not the PICT or TICT model applies to charge transfer processes in these systems seems to depend on the extent to which the donating nitrogen atom (or group containing it) has a localized lone pair, and whether or not the ground state molecule is twisted. Further high resolution experiments should address the extent to which these findings are modified by the attachment of weakly bound solvent molecules.

6.7 ACKNOWLEDGEMENTS

A. Held, S. Humphrey, J. McCombie, J. Ribblett, W. Sinclair, and M. J. Walker assisted with early zero-field experiments on PYRBN; L. Alvarez-Valtierra, J.W. Young, and C.L. Clements assisted with later electric field experiments on various molecules. We thank them for their help, and also thank J.P. Simons and J.A. Thomas for insightful discussions about this work. Our current research is supported by the NSF (CHE-0911117) and by the Andrew Mellon Predoctoral Fellowship Program at the University of Pittsburgh (A.J.F.).

6.8 REFERENCES

1. K. A. Zachariasse, T. von der Haar, A. Hebecker, U. Leinhos, and W. Kuehnle, *Pure Appl. Chem.* **65**, 1745 (1993).

2. E. Lippert, W. Lueder, and H. Boos, in *Advances in Molecular Spectroscopy*, edited by A. Mangini (Pergamon Press, Oxford, 1962), Vol. 1, p. 443.

3. K. Rotkiewicz, K. H. Grellmann, and Z. R. Grabowski, *Chem. Phys. Lett.* **19**, 315 (1973).

4. T. Hagan, D. Pilloud, and P. Suppan, *Chem. Phys. Lett.* **139**, 499 (1987).

5. C. Lerf and P. Suppan, *J. Chem. Soc., Faraday Trans.* **88**, 963 (1992).

6. R. Günther, D. Oelkrug, and W. Rettig, *J. Phys. Chem.* **97**, 8512 (1993).

7. C. Cornelissen-Gude and W. Rettig, *J. Phys. Chem. A* **102**, 7754 (1998).

8. S. Jiang and D. H. Levy, *J. Phys. Chem. A* **107**, 6785 (2003).

9. T. Yoshihara, V. A. Galievsky, S. I. Druzhinin, S. Saha, and K. A. Zachariasse, *Photochem. Photobiol. Sci.* **2**, 342 (2003).

10. J. R. Platt, *J. Chem. Phys.* **17**, 484 (1949).

11. A. Siemiarczuk, Z. R. Grabowski, A. Krowczynski, M. Asher, and M. Ottolenghi, *Chem. Phys. Lett.* **51**, 315 (1977).

12. W. Rettig, *Angew. Chem. Int. Ed. Engl.* **25**, 971 (1986).

13. E. Lippert, W. Rettig, V. Bonacic-Koutecky, F. Heisel, and J. A. Miehe, *Adv. Chem. Phys.* **68**, 1 (1987).

14. Z. R. Grabowski, K. Rotkiewicz, and W. Rettig, *Chem. Rev.* **103**, 3899 (2003).

15. K. A. Zachariasse, M. Grobys, T. von der Haar, A. Hebecker, Y. V. Il'ichev, O. Morawski, I. Rueckert, and W. Kuehnle, *J. Photochem. Photobiol., A* **105**, 373 (1997).

16. K. A. Zachariasse, S. I. Druzhinin, W. Bosch, and R. Machinek, *J. Am. Chem. Soc.* **126**, 1705 (2004).

17. T. Yoshihara, S. I. Druzhinin, and K. A. Zachariasse, *J. Am. Chem. Soc.* **126**, 8535 (2004).

18. S. I. Druzhinin, S. A. Kovalenko, T. Senyushkina, and K. A. Zachariasse, *J. Phys. Chem. A* **111**, 12878 (2007).

19. S. I. Druzhinin, S. A. Kovalenko, T. A. Senyushkina, A. Demeter, R. Machinek, M. Noltemeyer, and K. A. Zachariasse, *J. Phys. Chem. A* **112**, 8238 (2008).

20. S. I. Druzhinin, S. Kovalenko, T. A. Senyushkina, A. Demeter, R. Machinek, M. Noltemeyer, and K. A. Zachariasse, *J. Phys. Chem. A* **113**, 520 (2009).

21. T. Kobayashi, M. Futakami, and O. Kajimoto, *Chem. Phys. Lett.* **130**, 63 (1986).

22. J. A. Warren, E. R. Bernstein, and J. I. Seeman, *J. Chem. Phys.* **88**, 871 (1988).

23. V. H. Grassian, J. A. Warren, E. R. Bernstein, and H. V. Secor, *J. Chem. Phys.* **90**, 3994 (1989).

24. R. D. Gordon, *J. Chem. Phys.* **93**, 6908 (1990).

25. E. R. Bernstein, V. H. Grassian, and J. A. Warren, *J. Chem. Phys.* **93**, 6910 (1990).

26. B. D. Howells, M. T. Martinez, T. F. Palmer, J. P. Simons, and A. Walters, *J. Chem. Soc., Faraday Trans.* **86**, 1949 (1990).

27. M. J. Walker, Ph.D. Thesis, University of Nottingham, 1993.

28. O. Kajimoto, H. Yokoyama, Y. Ooshima, and Y. Endo, *Chem. Phys. Lett.* **179**, 455 (1991).

29. G. Berden, J. van Rooy, W. L. Meerts, and K. A. Zachariasse, *Chem. Phys. Lett.* **278**, 373 (1997).

30. K. Okuyama, Y. Numata, S. Odawara, and I. Suzuka, *J. Chem. Phys.* **109**, 7185 (1998).

31. F. P. Salgado, J. Herbich, A. G. M. Kunst, and R. P. H. Rettschnick, *J. Phys. Chem. A* **103**, 3184 (1999).

32. D. R. Borst, T. M. Korter, and D. W. Pratt, *Chem. Phys. Lett.* **350**, 485 (2001).

33. L. Belau, Y. Haas, and W. Rettig, *Chem. Phys. Lett.* **364**, 157 (2002).

34. H. Saigusa, N. Miyakoshi, C. Mukai, T. Fukagawa, S. Kohtani, R. Nakagaki, and R. Gordon, *J. Chem. Phys.* **119**, 5414 (2003).

35. L. Belau, Y. Haas, and W. Rettig, *J. Phys. Chem. A* **108**, 3916 (2004).

36. A. E. Nikolaev, G. Myszkiewicz, G. Berden, W. L. Meerts, J. F. Pfanstiel, and D. W. Pratt, *J. Chem. Phys.* **122**, 084309 (2005).

37. J. A. Thomas, J. W. Young, A. J. Fleisher, L. Alvarez-Valtierra, and D. W. Pratt, *J. Phys. Chem. Lett.* **1**, 2017 (2010).

38. L. Serrano-Andres, M. Merchan, B. O. Roos, and R. Lindh, *J. Am. Chem. Soc.* **117**, 3189 (1995).

39. B. Proppe, M. Merchan, and L. Serrano-Andres, *J. Phys. Chem. A* **104**, 1608 (2000).

40. A. B. J. Parusel, *Phys. Chem. Chem. Phys.* **2**, 5545 (2000).

41. S. Zilberg and Y. Haas, *J. Phys. Chem. A* **106**, 1 (2002).

42. A. Köhn and C. Hättig, *J. Am. Chem. Soc.* **126**, 7399 (2004).

43. I. Gómez, M. Reguero, M. Boggio-Pasqua, and M. A. Robb, *J. Am. Chem. Soc.* **127**, 7119 (2005).

44. S. Cogan, S. Zilberg, and Y. Haas, *J. Am. Chem. Soc.* **128**, 3335 (2006).

45. C. Hattig, A. Hellweg, and A. Kohn, *J. Am. Chem. Soc.* **128**, 15672 (2006).

46. P. Wiggins, J. A. G. Williams, and D. J. Tozer, *J. Chem. Phys.* **131**, 091101/1 (2009).

47. I. F. Galván, M. E. Martín, and M. A. Aguilar, *J. Chem. Theory Comput.* **6**, 2445 (2010).

48. I. F. Galván, M. E. Martín, A. Muñoz-Losa, M. L. Sánchez, and M. A. Aguilar, *J. Chem. Theory Comput.* **7**, 1850 (2011).

49. W. A. Majewski, J. F. Pfanstiel, D. F. Plusquellic, and D. W. Pratt, in *Laser Techniques in Chemistry*, edited by A. B. Myers and T. Rizzo (Wiley, New York, 1995), p. 101.

50. T. M. Korter, D. R. Borst, C. J. Butler, and D. W. Pratt, *J. Am. Chem. Soc.* **123**, 96 (2001).

51. D. M. Mitchell, P. J. Morgan, and D. W. Pratt, *J. Phys. Chem. A* **112**, 12597 (2008).

52. D. M. Miller, Ph.D. Thesis, University of Pittsburgh, 2010.

53. D. F. Plusquellic, Ph.D. Thesis, University of Pittsburgh, 1992.

54. D. F. Plusquellic, R. D. Suenram, B. Mate, J. O. Jensen, and A. C. Samuels, *J. Chem. Phys.* **115**, 3057 (2001).

55. R. G. Bird and D. W. Pratt, *J. Mol. Spectrosc.* **266**, 81 (2011).

56. L. Alvarez-Valtierra, S. T. Shipman, J. L. Neill, B. H. Pate, and A. Lessari, in *The Ohio State University International Symposium on Molecular Spectroscopy* (Columbus, OH, 2008), WF12.

57. T. Emilsson, H. S. Gutowsky, G. de Oliveira, and C. E. Dykstra, *J. Chem. Phys.* **112**, 1287 (2000).

58. Z. Kisiel, J. Kosarzewski, B. A. Pietrewicz, and L. Pszczolkowski, *Chem. Phys. Lett.* **325**, 523 (2000).

59. Z. Kisiel, E. Bialkowska-Jaworska, O. Desyatnyk, B. A. Pietrewicz, and L. Pszczolkowski, *J. Mol. Spectrosc.* **208**, 113 (2001).

60. M. J. Frisch, G. W. Trucks, H. B. Schlegel, G. E. Scuseria, M. A. Robb, J. R. Cheeseman, J. Montgomery, J. A., T. Vreven, K. N. Kudin, J. C. Burant, J. M. Millam, S. S. Iyengar, J. Tomasi, V. Barone, B. Mennucci, M. Cossi, G. Scalmani, N. Rega, G. A. Petersson, H. Nakatsuji, M. Hada, M. Ehara, K. Toyota, R. Fukuda, J. Hasegawa, M. Ishida, T. Nakajima, Y. Honda, O. Kitao, H. Nakai, M. Klene, X. Li, J. E. Knox, H. P. Hratchian, J. B. Cross, V. Bakken, C. Adamo, J. Jaramillo, R. Gomperts, R. E. Stratmann, O. Yazyev, A. J. Austin, R. Cammi, C. Pomelli, J. W. Ochterski, P. Y. Ayala, K. Morokuma, G. A. Voth, P. Salvador, J. J. Dannenberg, V. G. Zakrzewski, S. Dapprich, A. D. Daniels, M. C. Strain, O. Farkas, D. K. Malick, A. D. Rabuck, K. Raghavachari, J. B. Foresman, J. V. Ortiz, Q. Cui, A. G. Baboul, S. Clifford, J. Cioslowski, B. B. Stefanov, G. Liu, A. Liashenko, P. Piskorz, I. Komaromi, R. L. Martin, D. J. Fox, T. Keith, M. A. Al-Laham, C. Y. Peng, A. Nanayakkara, M. Challacombe, P. M. W. Gill, B. Johnson, W. Chen, M. W. Wong, C. Gonzalez, and J. A. Pople, GAUSSIAN 03, Revision C.02 (Gaussian, Inc., Wallingford, CT, 2004).

61. T. H. Dunning, Jr. and P. J. Hay, in *Modern Theoretical Chemistry*, edited by H. F. Schaefer, III (Plenum, New York, 1977), Vol. 3, p. 1.

62. J. K. G. Watson, in *Vibrational Spectra and Structure*, edited by J. R. Durig (Elsevier Scientific Publishing Company, New York, 1977), Vol. 6, p. 1.

63. R. G. Bird, J. L. Neill, V. J. Alstadt, J. W. Young, B. H. Pate, and D. W. Pratt, *J. Phys. Chem. A*, Articles ASAP, dx.doi.org/10.1021/jp111075r (2011).

64. W. Caminati, A. Dell'Erba, G. Maccaferri, and P. G. Favero, *J. Mol. Spectrosc.* **191**, 45 (1998).

65. *CRC Handbook of Chemistry and Physics*, 86th ed. (CRC Press, Taylor & Francis Group, Boca Raton, FL, 2005).

66. D. Schweke and Y. Haas, *J. Phys. Chem. A* **107**, 9554 (2003).

67. D. Schweke, H. Baumgarten, Y. Haas, W. Rettig, and B. Dick, *J. Phys. Chem. A* **109**, 576 (2005).

68. D. Schweke, Y. Haas, and B. Dick, *J. Phys. Chem. A* **109**, 3830 (2005).

69. W. Schuddeboom, S. A. Jonker, J. M. Warman, U. Leinhos, W. Kuehnle, and K. A. Zachariasse, *J. Phys. Chem.* **96**, 10809 (1992).

70. T. Yoshizawa, Y. Iwaki, N. Osaka, T. Nakabayashi, K. A. Zachariasse, and N. Ohta, *J. Phys. Chem. B* **108**, 19132 (2004).

71. R. Li, J. Zheng, and D. G. Truhlar, *Phys. Chem. Chem. Phys.* **12**, 12697 (2010).

7.0 EXCITED STATE PROTON TRANSFER IN *SYN*-2-(2′-PYRIDYL)PYRROLE OCCURS ON THE NANOSECOND TIMESCALE IN THE GAS PHASE.

Reprinted with permission from *Journal of Physical Chemistry Letters*.

Philip J. Morgan, Adam J. Fleisher, Vanesa Vaquero-Vara, David W. Pratt, Randolph P. Thummel, Michał Kijak, and Jacek Waluk, *J. Phys. Chem. Lett*. **2**, 2114 (2011).

PJM, AJF, VV, MK, and JW performed the experimental measurements. PJM analyzed the spectra. AJF performed theoretical calculations. RPT synthesized the sample. AJF and DWP wrote the paper.

7.1 ABSTRACT

Microwave and UV excitation spectra of 2-(2′-pyridyl)pyrrole (2PP) have been recorded at high resolution in the gas phase. Analyses of these data show that the *syn* conformer of 2PP is a planar molecule in both the ground (S_0) and first excited (S_1) electronic states, and that the S_1 state undergoes a relatively slow excited state proton transfer (ESPT) reaction when excited by light, as measured by the homogeneous line broadening that is observed in its UV spectrum. Apparently, excitation of the S_1 state moves electronic charge from the pyrrole ring to the pyridine ring, but the simultaneous transfer of the proton is inhibited by an unfavorably oriented dipole under solvent-free conditions. The rate of the ESPT reaction is enhanced by more than an order of magnitude with simultaneous excitation of a 144 cm^{-1} in-plane vibrational mode.

7.2 COMMUNICATION

We wish to report the observation of homogeneous line broadening in the high resolution fluorescence excitation spectrum of *syn*-2-(2′-pyridyl)pyrrole (2PP) in the gas phase, which makes possible the measurement of the rate of an excited state hydrogen atom transfer reaction in the isolated molecule, free of the perturbations of external solvent molecules.

Interest remains high in reactions of this type, loosely referred to as excited state proton transfer (ESPT) reactions,[1] since the pioneering study of Herek, *et al.*[2] on methyl salicylate (MS). Relevant recent experiments include studies of 2-(2′-hydroxyphenyl)-5-phenyloxazole (HPPO),[3] the 7-azaindole (7AI) dimer,[4] methanol complexes of 7-hydroxyquinoline (HYQ),[5] and water complexes of 7AI.[6] But in all of these cases except the first, the course of the ESPT reaction was

monitored by the appearance of a red-shifted emission of the product on short time scales, following picosecond (or less) pulsed excitation of the reactant, leading to ambiguities concerning the nature of the prepared state. Only in HPPO was homogeneous line broadening observed, from which an ESPT rate was determined, but even in this case excitation was provided by a nsec pulsed Nd:YAG pumped dye laser having a large bandwidth.[3] Thus, as will become apparent, all of the cited experiments utilized excitation sources whose frequency and/or coherence widths are much larger than the homogeneous widths of the individual rovibronic transitions in the S_1-S_0 electronic spectrum of 2PP.

Our experiments were performed in the collision-free environments of a supersonic jet for the microwave experiments [using a chirped-pulse Fourier transform microwave (FTMW) spectrometer][7] and a molecular beam for the UV experiments (using a ~ 1 MHz (0.00003 cm^{-1}) wide laser).[8] Previous studies of 2PP[9] have shown that the isolated molecule exhibits dual fluorescence, a strong "normal" fluorescence (F_1) that is attributed to 2PP (see I), and a much weaker red-shifted emission (F_2) that is attributed to the tautomer of 2PP, 1,2-dihydro-2-(2H-pyrrol-2-ylidene)-pyridine (2DP, II). The maximum of F_1 in the jet is blue shifted with respect to the solution value, but the maximum of F_2 appears at the same wavelength in both the gas phase and in solution.

Scheme 7-1

I

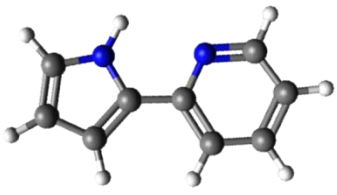

II

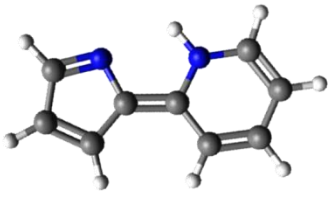

Figure 7-1 shows the high resolution S_1-S_0 fluorescence excitation spectrum of the origin band of 2PP, recorded in a molecular beam by monitoring the total emission following excitation at ~ 318 nm with the narrow-band laser. Immediately apparent is the partially resolved rotational structure in the spectrum. This was analyzed using the following procedure. First, ground state rotational constants of 2PP were determined from a fit to Watson's A-reduced Hamiltonian[10] of nine measured μ_a-type transitions in an independently measured microwave spectrum. (No μ_b- or μ_c-type transitions were observed in this spectrum.) Next, excited state rotational constants of 2PP were determined from a fit to rigid-rotor Hamiltonians of the observed rotational structure in the UV spectrum in Fig. 7-1 using the program JB95.[11] In this fit, ground state constants were kept fixed to their microwave values, and excited state constants were varied in a least-squares fashion to minimize differences between observed and calculated frequencies. Ultimately, 70 individual rovibronic transitions were fit, with a standard deviation of 4.9 MHz at a rotational temperature of ~ 5 K. Finally, each of the individual features in the spectrum was fit using a Voigt lineshape profile, resulting in a Gaussian width of 18-20 MHz, a Lorentzian width of 210 +/- 20 MHz, and an overall band character that is 90% *a*-type and 10% *b*-type, giving an electronic transition moment that makes an angle of θ = +/- 18 +/- 5° with respect to the *a* inertial axis of the 2PP frame.

Tables 7-1 and 7-2 list the rotational constants that were derived from this analysis and compares them with selected theoretical values.[12] First, we note the excellent agreement between experiment and theory for the ground electronic state of 2PP (Table 7-1); the calculated values of *A*, *B*, and *C* are nearly identical to the measured ones, especially when zero-point vibrational motions are taken into account. 2PP is a planar molecule in its ground electronic state. The

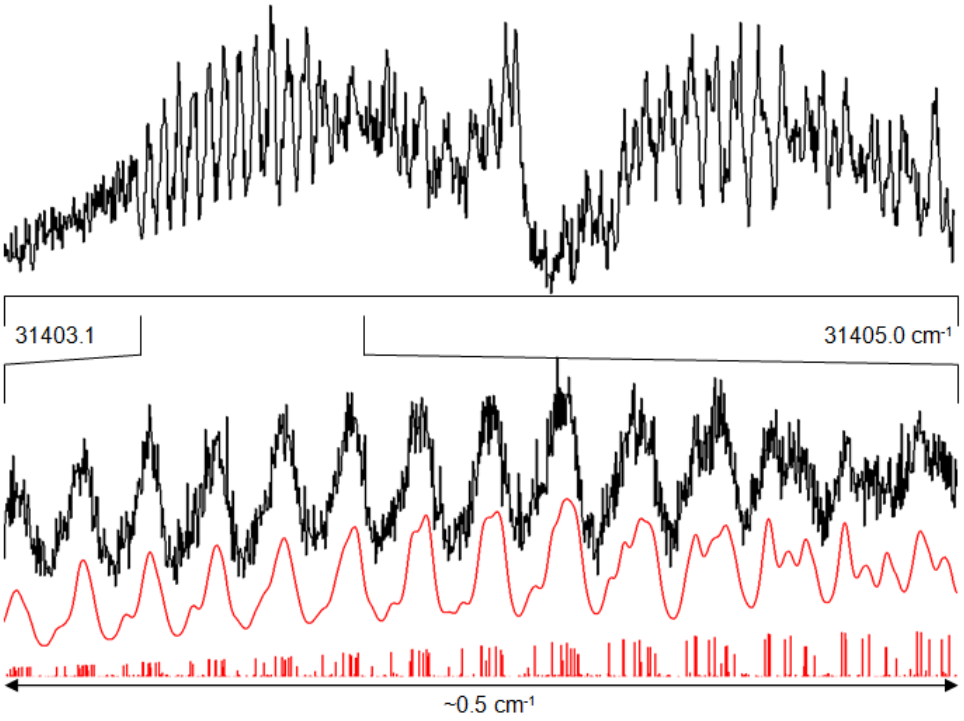

Figure 7-1. Rotationally resolved fluorescence excitation spectrum of the origin band in the S_1-S_0 electronic transition of *syn*-2-(2′-pyridyl)pyrrole (2PP) in the gas phase, at ~ 318 nm. The lower part of the figure shows an expanded scale view of a portion of the P-branch region. The black trace is the experimental spectrum, and the red trace is the simulated spectrum with and without a convoluted line shape function; the vertical lines represent the individual rovibronic transitions responsible for the spectrum.

Table 7-1. Inertial parameters of 2PP in its ground electronic state.[a]

Parameter	2PP Microwave	2PP Theoretical[b]	2DP Theoretical[b]
A″ (MHz)	3561.72(22)	3575.6	3513.2
B″ (MHz)	710.4228(14)	711.8	724.2
C″ (MHz)	592.5936(14)	593.9	600.6
ΔI″ (uÅ^2)	-0.444(12)	-0.41	-0.28
μ_a″ (D)		-1.38	-5.37
μ_b″ (D)		0.11	0.37
|μ″| (D)		1.38	5.38
OMC (kHz)	14		
assigned lines	9		

[a]Standard deviations in the final digits are shown in parentheses. See Appendix E for transition assignments.

[b]Geometry optimization calculations, which include zero-point vibrational level contributions in S_0, were done at the M05-2X/6-31+G* level of theory using anharmonic frequency corrections. Permanent electric dipoles were calculated using an MP2/aug-cc-pVDZ point calculation on the previously optimized vibrationally averaged geometry.

Table 7-2. Inertial parameters of 2PP in its excited electronic state.[a]

Parameter	2PP Experimental	2PP Theoretical[b]	2DP Theoretical[b]
A′ (MHz)	3427.5(10)	3481.1	3495.6
B′ (MHz)	725.72(10)	724.9	726.7
C′ (MHz)	599.22(10)	600.3	602.1
$\Delta I'$ (uÅ^2)	-0.43(28)	-0.42	-0.61
μ_a' (D)		1.20	-0.94
μ_b' (D)		-0.06	0.22
$\lvert\mu'\rvert$ (D)		1.21	0.97
Origin (cm^{-1})	31404.1		
a/*b*/*c* type	90/10/0	99/1/0	86/14/0
OMC (MHz)	4.9		
assigned lines	70		

[a]Standard deviations in the final digits are shown in parentheses.

[b]Geometry optimization calculations, which include zero-point vibrational level contributions in S_1, were done at the CIS/6-31+G* level of theory using anharmonic frequency corrections. Permanent electric dipoles were calculated using a CIS/aug-cc-pVDZ point calculation on the previously optimized vibrationally averaged geometry.

calculated permanent electric dipole moment (EDM) of 2PP also accords with experiment; μ makes its largest projection on the *a*-inertial axis (μ_a = - 1.38 D), thereby explaining the absence of strong μ_b- and μ_c-type transitions in the microwave spectrum, and (according to theory) points towards the pyrrole ring. The predicted values of the rotational constants and EDM of the proton transferred structure, 2DP, in its ground electronic state are significantly different from those of 2PP.

Next, we consider the properties of the excited electronic state (Table 7-2). Here, the agreement between the experimental and calculated rotational constants is less impressive, but it is adequate to conclude that the carrier of the spectrum is the non-proton transferred structure, 2PP, rather than 2DP. This accords with expectations; the F_2 emission makes only a small contribution to the total fluorescence intensity.[9] 2PP also is a planar molecule in its S_1 state. The large decrease in *A* (-134 MHz), compared to the ground state, may be attributed to increases in bond lengths perpendicular to *a*, reflecting expansions of the pyridine and pyrrole rings upon excitation. The small increases in *B* and *C* (+15.3 and +6.6 MHz, respectively) indicate that the pyridine and pyrrole rings are moving closer together in the excited state. Theory predicts the C-C bond linking the two rings to have a length of 146 pm in the S_0 state and 139 pm in the S_1 state. The shorter length of this bond in the S_1 state may reveal incipient motion along the ESPT reaction coordinate, as this bond is a double bond in 2DP. Though the F_2 emission is relatively weak, the eigenstates excited in our experiments may contain small contributions from the proton-transferred structure.

According to theory, the S_1-S_0 transition is principally a π,π* (HOMO-LUMO) transition that moves electron density from the pyrrole ring to the pyridine ring, strengthening the bond between them. The calculated transition dipole moment (TDM) makes an angle of 5.8° with the *a*

inertial axis, in agreement with experiment. Owing to the motion of charge, theory predicts that direction of the permanent EDM is reversed in the S_1 state of 2PP, but has about the same magnitude; whereas the magnitude of the EDM in the S_1 state of 2DP is greatly enhanced, compared to the ground S_0 state, but has the same sign. A similar reversal in sign of the EDM has been observed in the S_1-S_0 spectrum of the related molecule, 1-phenylpyrrole (1PhP).[13]

Direct evidence for the ESPT reaction in 2PP is provided by the homogeneous line broadening observed in its high resolution UV spectrum, 210 MHz, which considerably exceeds the Doppler contribution to the linewidth of 18-20 MHz. The Lorentzian contribution gives a measured lifetime of 0.80 ± 0.05 nsec for the S_1 state. Now, molecules of this type typically exhibit fluorescence lifetimes that are an order of magnitude longer than this. For example, the S_1 (π,π^*) state of 1PhP has a lifetime of 13 nsec.[13] The calculated oscillator strength of the S_1-S_0 transition of 2PP is 0.33,[14] whereas that of 1PhP is substantially less.[13] Thus, while it is possible that the observed line broadening is caused by an enhanced radiative decay of 2PP, we attribute the increased spectral width of the S_1-S_0 origin band of 2PP to an ESPT reaction in the S_1 state.

Proof of this conjecture is provided by the measurement of the high resolution spectrum of the + 144 cm^{-1} vibronic band in the S_1-S_0 spectrum of 2PP, shown in Fig. 7-2. This band exhibits significantly broader lines, compared to the origin band in Fig. 7-1. While it proved impossible to assign individual features in the spectrum shown in Fig. 7-2, its overall contour can be simulated with a Lorentzian contribution that is ten times larger than that of the origin band, giving an S_1 lifetime that is ten times shorter, 0.08 nsec (80 psec). Previous gas phase studies of the low resolution fluorescence excitation spectrum of 2PP with selective detection of the F_2 emission[9] revealed a large increase in the relative intensity of this band and other bands built on the 144 cm^{-1} vibration, compared to a spectrum that was detected by monitoring the total

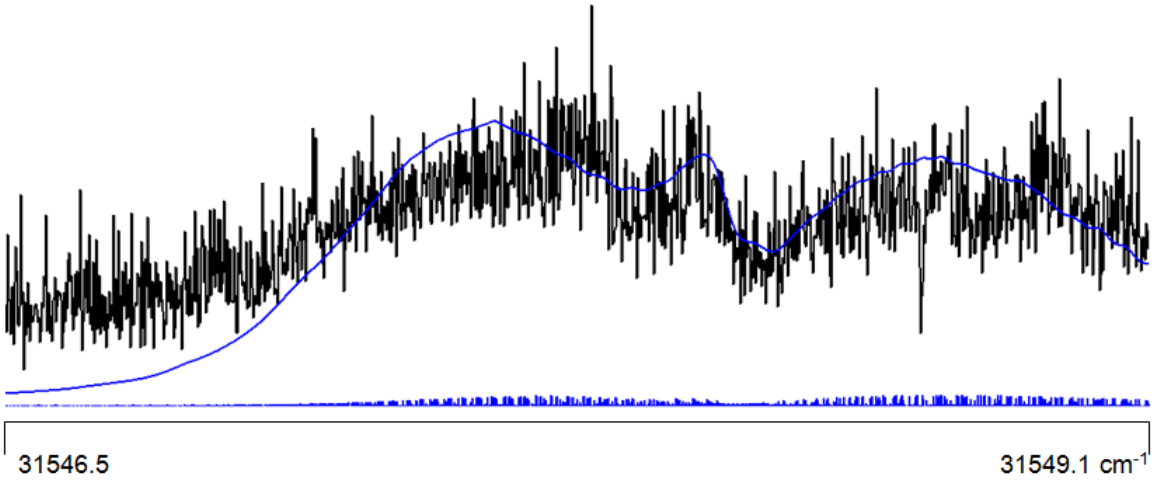

Figure 7-2. Contour fit of the high resolution fluorescence excitation spectrum of the 0,0 + 144 cm^{-1} vibronic band in the S_1-S_0 electronic transition of 2PP. The experimental spectrum is shown in black, and the simulation is shown in blue.

emission, suggesting that this vibration is a promoting mode for the ESPT reaction. Thus, the reduced lifetimes of both observed vibrational levels in the S_1 state of 2PP may safely be attributed to an ESPT reaction.

Previous studies of 2PP and related molecules in the condensed phase[15] suggest time scales of the order of psec or less for the ESPT reaction. So, it was initially surprising to discover that the reaction rate is considerably slower that this for the isolated molecule in the gas phase. One possible explanation for this result is, of course, that since the previous experiments were performed with psec and fsec lasers, the molecules were in the statistical limit with respect to the ensuing dynamics. All vibrational modes could be accessed under these conditions, speeding up ESPT. Another possibility is that the process is "solvent-assisted" in the condensed phase. In cyclic water or alcohol complexes of molecules like 7AI, simulations[16] have shown that very efficient and fast proton-transfer reactions can be expected. But a recent gas phase study of an isolated 7AI-H_2O complex in the gas phase[17] has revealed that ESPT does not occur within the lifetime of the S_1 state, despite a favorable position of the attached water molecule. In this case, photoexcitation produces "instantaneous" charge transfer, but fast proton transfer does not occur.

Rode and Sobolweski[13] have recently examined the role of electron and proton transfer processes in hydrogen-bonded systems using *ab initio* methods. In the case of 2PP, they find that the S_1 state of the *syn* conformer shows a small barrier (about 0.2 eV) for transfer of a hydrogen atom to the pyridine ring. A second highly polar charge transfer state of π,π^* character drives the proton transfer, which leads to a conical intersection and ultrafast conversion. However, in the bare molecule, access to this state is blocked by the barrier; the S_1 state of 2DP is a saddle point on the potential energy surface, and is unstable with respect to torsion around the central CC bond. There is no evidence for torsional activity in the high resolution spectra of 2PP. Instead,

we find (as did Kijak, *et al.*[9]) that an in-plane vibrational mode promotes the process, and that the polarization of the + 144 cm^{-1} band in the S_1-S_0 spectrum of 2PP is similar to that of the origin band, suggesting that vibronic coupling is not involved. (The important role of vibronic coupling in mediating access to conical intersections has been discussed elsewhere.[18]) Thus, from our perspective, the barrier that slows the ESPT process in the isolated molecule is more likely to have its origin in the orientation of its permanent electric dipole.[19] If the dipole moments of the normal and tautomeric forms differ either in their magnitude or in their orientation (or both), a barrier might then exist along the ESPT coordinate in the isolated molecule that cannot be compensated for by solvent reorganization. Our calculations on the present system suggest that the excited state permanent EDMs of 2PP and 2DP have approximately the same magnitude but are oriented in opposite directions (see Table 7-2). The same is true for 7AI-H_2O.[17] Solvent molecules are not required in the salicylic acid/MS systems, since the dipoles of the two connecting states are more nearly aligned, and there is no barrier, even in the isolated molecule.[20] Therefore, it is perhaps not surprising that the ESPT reaction of 2PP in the gas phase is significantly slower than the corresponding reaction in solution.

7.3 ACKNOWLEDGEMENTS

Some theoretical calculations were performed at the Center for Simulation and Modeling (SAM) at the University of Pittsburgh. This research has been supported by the National Science Foundation (CHE-0714751, RPT, and CHE-0911117, DWP), the Robert E. Welch Foundation (E-621, RPT), and the Andrew Mellon Predoctoral Fellowship Program (AJF). We are grateful for their support.

7.4 REFERENCES

1. *Hydrogen Bonding and Transfer in the Excited State*, edited by K.-L. Han and G.-J. Zhao, (Wiley-Interscience, New York, 2010).

2. J. L. Herek, S. Pedersen, L. Banares, and A. H. Zewail, *J. Chem. Phys.* **97**, 9046 (1992).

3. A. Douhal, F. Lahmani, A. Zehnacker-Rentien, and F. Amat-Guerri, *J. Phys. Chem.* **98**, 12198 (1994).

4. D. E. Folmer, E. S. Wisniewski, S. M. Hurley, and A. W. Castleman, Jr., *Proc. Natl. Acad. Sci.* **96**, 12980 (1999).

5. Y. Matsumoto, T. Ebata, and N. Mikami, *J. Phys. Chem. A* **106**, 5591 (2002).

6. G. A. Pino, I. Alata, C. Dedonder, C. Jouvet, K. Sakota, and H. Sekiya, *Phys. Chem. Chem. Phys.* **13**, 6325 (2011).

7. R. G. Bird, J. L. Neill, V. J. Alstadt, J. W. Young, B. H. Pate, and D. W. Pratt, *J. Phys. Chem. A*, Articles ASAP, dx.doi.org/10.1021/jp111075r (2011).

8. W. A. Majewski, J. F. Pfanstiel, D. F. Plusquellic, and D. W. Pratt, in *Laser Techniques in Chemistry*, edited by A. B. Myers and T. R. Rizzo, (John Wiley and Sons, New York, 1995), p. 101.

9. M. Kijak, Y. Nosenko, A. Singh, R. P. Thummel, and J. Waluk, *J. Am. Chem. Soc.* **129**, 2738 (2007).

10. J. K. G. Watson, in *Vibrational Spectra and Structure*, edited by J. R. Durig, (Elsevier Scientific Publishing Company, Amsterdam, 1977), Vol. 6, p. 1.

11. D. F. Plusquellic, R. D. Suenram, B. Mate, J. O. Jensen, and A. C. Samuels, *J. Chem. Phys.* **115**, 3057 (2001).

12. M. J. Frisch, G. W. Trucks, H. B. Schlegel, G. E. Scuseria, M. A. Robb, J. R. Cheeseman, J. Montgomery, J. A., T. Vreven, K. N. Kudin, J. C. Burant, J. M. Millam, S. S. Iyengar, J. Tomasi, V. Barone, B. Mennucci, M. Cossi, G. Scalmani, N. Rega, G. A. Petersson, H. Nakatsuji, M. Hada, M. Ehara, K. Toyota, R. Fukuda, J. Hasegawa, M. Ishida, T. Nakajima, Y. Honda, O. Kitao, H. Nakai, M. Klene, X. Li, J. E. Knox, H. P. Hratchian, J. B. Cross, V. Bakken, C. Adamo, J. Jaramillo, R. Gomperts, R. E. Stratmann, O. Yazyev, A. J. Austin, R. Cammi, C. Pomelli, J. W. Ochterski, P. Y. Ayala, K. Morokuma, G. A. Voth, P. Salvador, J. J. Dannenberg, V. G. Zakrzewski, S. Dapprich, A. D. Daniels, M. C. Strain, O. Farkas, D. K. Malick, A. D. Rabuck, K. Raghavachari, J. B. Foresman, J. V. Ortiz, Q. Cui, A. G. Baboul, S. Clifford, J. Cioslowski, B. B. Stefanov, G. Liu, A. Liashenko, P. Piskorz, I. Komaromi, R. L. Martin, D. J. Fox, T. Keith, M. A. Al-Laham, C. Y. Peng, A. Nanayakkara, M. Challacombe, P. M. W. Gill, B. Johnson, W. Chen, M.

W. Wong, C. Gonzalez, and J. A. Pople, GAUSSIAN 03, Revision C.02 (Gaussian, Inc., Wallingford, CT, 2004).

13. J. A. Thomas, J. W. Young, A. J. Fleisher, L. Alvarez-Valtierra, and D. W. Pratt, *J. Phys. Chem. Lett.* **1**, 2017 (2010).

14. M. F. Rode and A. L. Sobolewski, *Chem. Phys*. **347**, 413 (2008).

15. D. Marks, H. Zhang, P. Borowicz, J. Waluk, and M. Glasbeek, *J. Phys. Chem. A* **104**, 7167 (2000).

16. D. Kina, A. Nakayama, T. Noro, T. Taketsugu, and M. S. Gordon, *J. Phys. Chem. A* **112**, 9675 (2008).

17. J. W. Young and D. W. Pratt, *J. Chem. Phys.*, in press.

18. C. Brand, J. Küpper, D. W. Pratt, W. L. Meerts, D. Kruegler, J. Tatchen, and M. Schmitt, *Phys. Chem. Chem. Phys*. **12**, 4968 (2010) and the following paper.

19. See, for example, A. Sytnik, D. Gormin, and M. Kasha, *Proc. Natl. Acad. Sci*. **91**, 11968 (1994).

20. J. W. Young, A. J. Fleisher, and D. W. Pratt, *J. Chem. Phys.* **134**, 084310 (2011).

APPENDIX A

SUPPORTING INFORMATION FOR CHAPTER 2.0

A.1 BARRIER HEIGHT ANALYSIS

The effective inertial defect ΔI_{eff} measured for the A subband of InA in Chapter 2.0 contains second-order contributions from the coupling of torsion and overall rotation. The ΔI_{eff} of the A subband is related to the effective rotational constants *via*

Equation A-1

$$\Delta I_{\text{eff}} = \frac{k}{C_{\text{eff}}} - \frac{k}{A_{\text{eff}}} - \frac{k}{B_{\text{eff}}}$$

where k = 505379.005 uÅ^{2}MHz. The ammonia molecule sits in the *ab* plane of the InA complex at angles of 32° in S_0 and 36° in S_1. Therefore, there is no projection of the internal rotation axis of NH_3 onto the *c* inertial axis of the complex, and the effective rotational constants are related to the static rotational constants *via*

Equation A-2

$$A_{\text{eff}} = A + FW_{v\sigma}^{(2)}\rho_a^2$$

Equation A-3

$$B_{\text{eff}} = B + FW_{v\sigma}^{(2)}\rho_b^2$$

Equation A-4

$$C_{\text{eff}} = C$$

Above, F is the internal rotor constant in MHz, and can be calculated from the known moment of inertia of NH_3 (I_α),[1] the projection of the internal rotor axis onto the inertial axes of the system, and a reducing factor r.

Equation A-5

$$F = \frac{k}{rI_\alpha}$$

Equation A-6

$$r = 1 - \left[\frac{\lambda_a^2 I_\alpha}{I_a} - \frac{\lambda_b^2 I_\alpha}{I_b} - \frac{\lambda_c^2 I_\alpha}{I_c}\right]$$

In InA, we calculated F'' = 188.0 GHz in S_0 and F' = 187.7 GHz in S_1. Additionally, ρ_a and ρ_b are the projection of I_α onto either the a or b inertial axes of InA, and are calculated using the direction cosines λ_g and Eqs. A-7 and A-8.

Equation A-7

$$\rho_a = \frac{\lambda_a I_\alpha}{I_a}$$

Equation A-8

$$\rho_b = \frac{\lambda_b I_\alpha}{I_b}$$

In defining the above equations, our goal is to estimate the static rotational constants *A*, *B*, and *C* in order to calculate values of $W^{(2)}$ in each electronic state. In Table 2-4 of Chapter 2.0, the optimized static structures of InA consistently yield inertial defect values of ΔI_{stat} = -2.67 uÅ^2. Therefore, the static rotational constants are related to ΔI_{stat} *via*

Equation A-9

$$\Delta I_{\text{stat}} = \frac{k}{C} - \frac{k}{A} - \frac{k}{B}$$

where *A*, *B*, and *C* are defined in Eqs. A-2 through A-4. If we rearrange Eqs. A-2 through A-4 and substitute for the static rotational constants, it becomes possible to vary $W^{(2)}$ to reproduce ΔI_{stat} in each electronic state.

$$\Delta I_{\text{stat}} = \frac{k}{C_{\text{eff}}} - \frac{k}{A_{\text{eff}} - FW_{00}^{(2)}\rho_a^2} - \frac{k}{B_{\text{eff}} - FW_{00}^{(2)}\rho_b^2}$$

The $W^{(2)}$ values determined in this way are related to the barrier height[2,3] *via* Herschbach's equations[4] and available data tables.[5] For the ground state of InA, we calculated $V_3'' = 44$ cm^{-1}. In the excited state, we calculated a slightly larger barrier height of $V_3' = 48$ cm^{-1}. This change in barrier height upon excitation predicts an *E-A* band tunneling splitting of -9930 MHz, in excellent agreement with the experimental estimate of ~9900 MHz.

We have checked this procedure by completing the same *A* subband analysis for NH_3 internal rotors previously analysis using high resolution electronic spectroscopy.[6-8] Table A-1 lists the V_3 barrier heights calculated from the *A* subband inertial defect as compared to the more accurate V_3 values calculated from a direct rotational fit of the *E* subbands, which provide the first-order perturbation coefficients $W^{(1)}$. Clearly, the ΔI analysis consistently overestimates the V_3 barrier heights. We therefore conclude that the V_3 barriers to hindered internal rotation of NH_3 in the InA complex are less than $V_3'' = 44$ and $V_3' = 48$ cm^{-1}, respectively.

Table A-1. Predicted V_3 barrier heights (cm^{-1}) using *A* subband ΔI_{eff} values (uÅ^2) from select NH_3 complexes. All predicted V_3 values overestimate the barrier height as compared to V_3 calculated from the first-order perturbation coefficients $W^{(1)}$ determined by fitting the respective *E* subbands.

State	Parameter	*c*2HNA[a]	*t*2HNA[b]	*t*1HNA[c]	*t*HQA[d]	InA[e]
S_0	ΔI_{eff} from *A* band	-0.936	-1.262	-1.215	-0.980	+0.27
	V_3 from ΔI_{eff}	71.3	84.1	81.5	74.4	44
	V_3 from *E* band	41.1	34.2	39.9	35.5	--
S_1	ΔI_{eff} from *A* band	-1.286	-1.443	-1.117	-1.381	+0.04
	V_3 from ΔI_{eff}	83.4	91.5	77.9	88.8	48
	V_3 from *E* band	53.8	58.2	46.5	58.8	--

[a] *cis*-β-naphthol-NH_3 (Ref. 6).
[b] *trans*-β-naphthol-NH_3 (Ref. 6).
[c] *trans*-α-naphthol-NH_3 (Ref. 7).
[a] *trans*-hydroquinone-NH_3 (Ref. 8).
[e] This work.

Finally, we have calculated the theoretical inertial defect values for the complexes listed in Table A-1 by requiring the reproduction of each V_3 barrier height calculated from each E subband fit (labeled ΔI_{theor}). The following equation, which removes both static and measured inertial defect contributions from the theoretical values, leaves a barrier-dependent inertial defect term ΔI_{cor}.

Equation A-10

$$\Delta I_{\text{theor}} = \Delta I_{\text{exp}} + \Delta I_{\text{stat}} + \Delta I_{\text{cor}}$$

This ΔI correction factor appears linearly related to the measured V_3 barrier heights over the range of 30-65 cm^{-1}, as shown in Fig. A-1. This interesting observation requires more attention in order to understand and interpret the physical meaning and predictive capabilities of such a linear relationship.

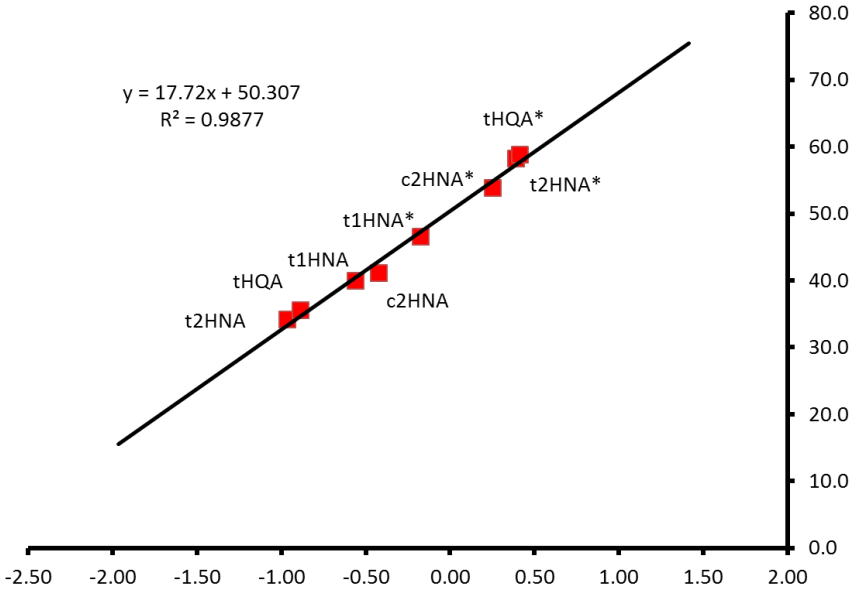

Figure A-1. Plot of V_3 *vs.* ΔI_{cor} for the four complexes listed in Table A-1. A best-fit trendline equation is shown in the top left corner. An asterisk (*) indicates an excited S_1 state.

A.2 REFERENCES

1. V. A. Job, N. D. Patel, R. D'Cunha, and V. B. Kartha, *J. Mol. Spectrosc*. **101**, 48 (1983).

2. A.C. Fantoni and W. Caminati, *J. Chem. Soc., Faraday Trans*. **92**, 343 (1996).

3. W. Caminati, J. C. Lopez, S. Blanco, S. Mata, and J. L. Alonso, *Phys. Chem. Chem. Phys*. **12**, 10230 (2010).

4. D.R. Herschbach, *J. Chem. Phys*. **31**, 91 (1959).

5. *Tables Relating to Mathieu Functions*, (Columbia University Press, New York, 1951).

6. D. F. Plusquellic, X.-Q. Tan, D. W. Pratt, *J. Chem. Phys*. **96**, 8026 (1992).

7. S.J. Humphrey and D.W. Pratt, *J. Chem. Phys*. **104**, 8332 (1996).

8. S.J. Humphrey and D.W. Pratt, *J. Chem. Phys*. **106**, 908 (1997).

APPENDIX B

SUPPORTING INFORMATION FOR CHAPTER 3.0

Table B-1. Theoretical permanent EDMs of *cis*-2HN and *cis*-2HNA. The dipole moment angle with respect to the *a* inertial axis is defined as θ_a. S_0 calculations were done using the MP2 level of theory and the indicated basis set, while S_1 calculations were done using the CIS level of theory. Components of the molecular polarizability tensor for *cis*-2HN are also included.

	***cis*-2HN**		***cis*-2HN · NH_3**			
	6-31G**	Error (%)	6-31G**	Error (%)	6-31++G**	Error (%)
S_0						
μ_a (D)	0.32	7.0	-3.14	22.6	-2.70	5.5
μ_b (D)	-1.11	16.7	-3.20	9.2	-3.08	5.1
μ_c (D)	0.00		-0.04		0.04	
μ (D)	1.15	13.9	4.49	15.4	4.10	5.4
θ_a (deg)	73.8		134.4		131.2	
α_a (Å^3)	23.46					
α_b (Å^3)	16.60					
S_1						
μ_a (D)	0.26	263.5	-3.51	6.6	-3.33	11.4
μ_b (D)	-1.38	19.0	-3.13	2.5	-2.91	9.3
μ_c (D)	0.00		0.00		-0.01	
μ (D)	1.41	20.5	4.70	4.9	4.42	10.5
θ_a (deg)	79.4		138.3		138.9	
α_a (Å^3)	30.41					
α_b (Å^3)	17.79					

APPENDIX C

SUPPORTING INFORMATION FOR CHAPTER 4.0

Table C-1. Calculated electrostatic interaction energies of *cis*-2HNW. Below, *cis*-2HN is designated as 1 and H_2O is designated as 2. The angles θ_1 and θ_2 are the angles μ_1 and μ_2 make with the line R_{CM}.

	S_0	S_1
μ_1 (D)	1.011	1.17
μ_2 (D)	1.78	1.78
μ_{ind} (D)	0.57	0.73
θ_1 (°)	46.0	33.1
θ_2 (°)	24.4	12.9
R_{CM} (Å)	5.14[a]	5.08[a]
Q (e)	0.08	0.06
d (Å)	2.90[b]	2.88[b]
$E_{\mu\mu}$ (cm^{-1})	-64.7	-120.5
$E_{\alpha\mu}$ (cm^{-1})	-35.2	-49.0
E_{CT} (cm^{-1})	-252.1	-136.7
$E_{complex,rel}$ (cm^{-1})	-352.0	-306.2

[a]Calculated assuming the COM of water is in the *ab* plane of 2HN.
[b]HF and CIS calculated heavy atom distances using the 6-31+G* basis set.

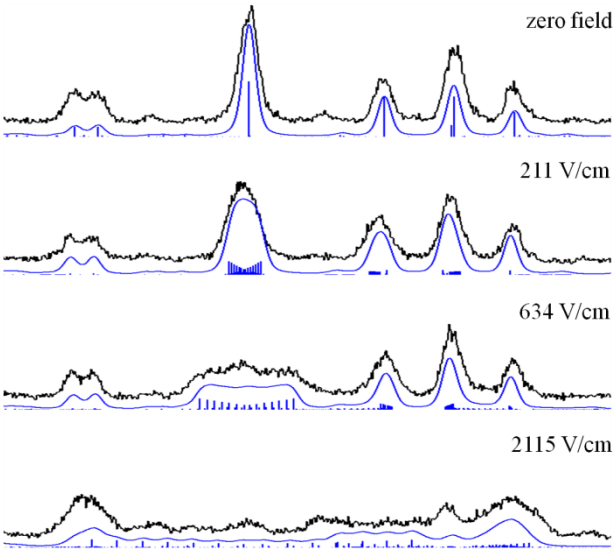

Figure C-1. Stark effect in the electronic spectrum of *trans*-2HN at full rotational resolution. The blue trace is simulated using the dipole moments listed in Table 4-4. The most intense transition in the zero field spectrum is assigned the quantum numbers |854› ← |963›.

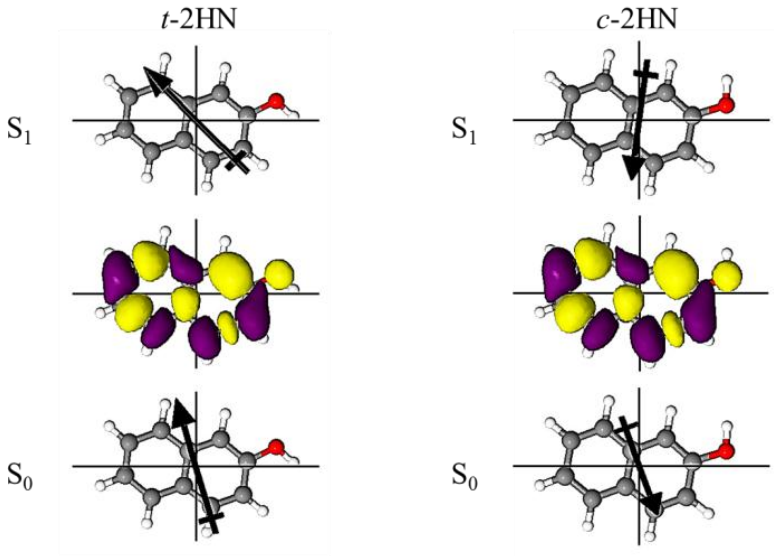

Figure C-2. Experimental ground and excited state dipole moments of *trans* and *cis*-2HN (scale: 1.0 D = 4.0 Å). The center images are the weighted electron density differences upon $S_1 \leftarrow S_0$ excitation calculated at the CIS/6-31G** level. Purple indicates electron density gain upon excitation, whereas yellow indicates electron density loss.

APPENDIX D

SUPPORTING INFORMATION FOR CHAPTER 6.0

D.1 THEORETICAL DETAILS

In order to include PYRBN in the comparison between experiment and theory reported in Table 6-3, the PYRBN ground state geometry was optimized using M05-2X density functional theory[1] and the 6-31+G* basis set (keyword *Int=Ultrafine*).[2] Then, two point calculations were performed at the complete active space self-consistent field (CASSCF) level; one for the ground S_0 state and another for the excited S_1 state. An active space including 12 electrons and 10 molecular orbitals (6 π and 4 π^*) was chosen for these calculations, using the D95V basis set[3] for each electronic state (keywords *SCF=Tight* and *Density=Current*).[2]

The Cartesian coordinates (X, Y, Z in standard orientation) of the optimized structure are shown in Table D-1. Since both the vibrationally and rotationally resolved spectra of PYRBN show little evidence of significant geometric change upon excitation, the "vertical" excitation investigated here by theory should be sufficient for the purposes of Table 6-3. Attempts to optimize the PYRBN geometry using CASSCF with a sufficiently large active space are currently underway.

Table D- 1. Cartesian coordinates of the PYRBN optimized geometry (Å).

Atomic number	X	Y	Z
6	1.9189	1.2024	-0.0976
6	2.6298	0.0000	0.0002
6	1.9188	-1.2024	0.0977
6	0.5359	-1.2084	0.0985
6	-0.1919	0.0000	-0.0003
1	2.4604	2.1363	-0.1779
1	2.4603	-2.1363	0.1782
1	0.0137	-2.1504	0.1901
6	-2.3605	1.2146	0.0273
6	-2.3605	-1.2145	-0.0273
6	-3.7680	0.6925	0.3274
1	-2.3215	1.7341	-0.9382
1	-2.0028	1.9001	0.7991
6	-3.7681	-0.6925	-0.3268
1	-2.3210	-1.7334	0.9385
1	-2.0033	-1.9005	-0.7990
1	-3.9009	0.5952	1.4075
1	-4.5463	1.3512	-0.0569
1	-4.5463	-1.3512	0.0579
1	-3.9016	-0.5953	-1.4069
7	-1.5534	0.0000	-0.0006
6	4.0633	0.0000	0.0004
7	5.2211	0.0000	-0.0001
6	0.5359	1.2084	-0.0988
1	0.0138	2.1504	-0.1907

Figure D-1 illustrates the molecular orbitals involved in the S_1-S_0 electronic excitation of PYRBN. As was found in the high resolution experiments, the S_1 state of PYRBN is the ^1L_b state, with a *b*-type electronic transition moment (ETM).

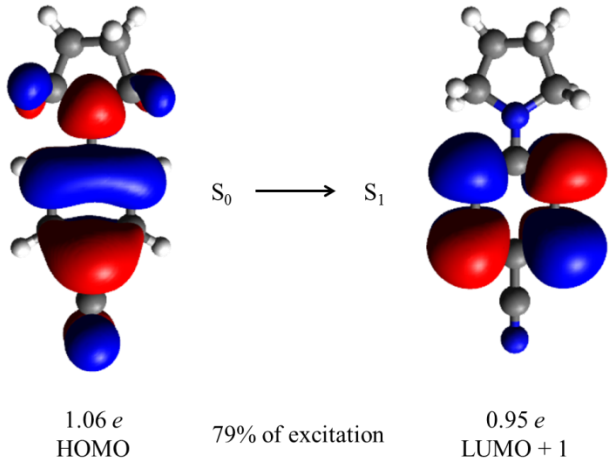

Figure D-1. CASSCF(12,10)/D95V molecular orbitals principally involved in the lowest energy π-π* excitation of PYRBN. Orbital populations were taken from the final density matrix. The vertical excitation energy is 4.54 eV, or approximately 36600 cm^{-1}, without corrections for dynamic electron correlation or zero-point energy.

D.2 MICROWAVE SPECTRA AND ASSIGNMENTS

The CP-FTMW spectrum of PBN recorded from 6.5 – 17 GHz at the University of Pittsburgh is shown in Fig. D-2. A portion of the Stark CP-FTMW spectrum of DMABN recorded at the University of Virginia is shown in Fig. D-3, and individual rotational transition assignments are listed in Table D-2.

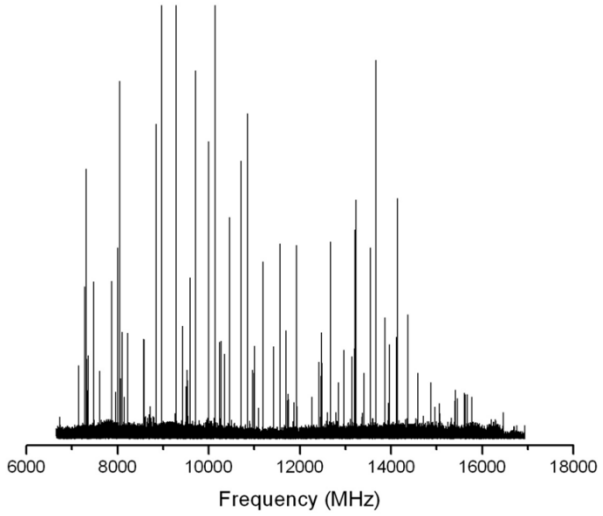

Figure D-2. CP-FTMW spectrum of PBN recorded from 6.5 – 17 GHz.

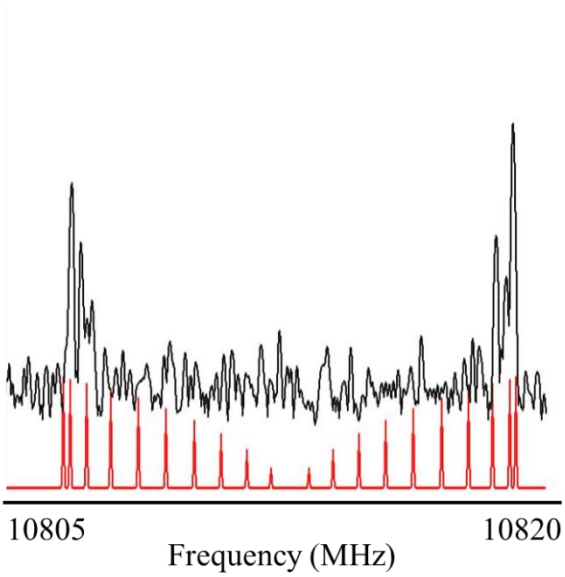

Figure D-3. A portion of the Stark CP-FTMW spectrum of DMABN recorded at an applied electric field of 23.7 V/cm.

Table D-2. List of assigned rotational transitions in the Stark CP-FTMW spectrum of DMABN using QSTARK.[4,5] The F and M_F quantum numbers are in units of 1/2, and the frequencies are in MHz. The standard deviation of the fit is 0.057 MHz.

J	K_a	K_c	←	J	K_a	K_c	F	M_F	←	F	M_F		Obs	Obs - Calc	Calc
7	4	3	←	6	4	2	14	4	←	12	4	20.1	7551.6224	-0.05099	7551.6734
7	4	3	←	6	4	2	14	2	←	12	2	20.1	7553.4582	-0.03716	7553.4954
7	4	4	←	6	4	3	14	0	←	12	0	20.1	7555.294	-0.01094	7555.3049
7	4	4	←	6	4	3	14	2	←	12	2	20.1	7557.106	-0.03416	7557.1402
7	3	4	←	6	3	3	14	4	←	12	4	20.1	7558.1074	-0.04732	7558.1547
7	4	4	←	6	4	3	14	4	←	12	4	20.1	7558.9657	0.00264	7558.9631
7	3	5	←	6	3	4	14	0	←	12	0	20.1	7559.3233	-0.06304	7559.3863
7	3	4	←	6	3	3	14	2	←	12	2	20.1	7559.6571	-0.0759	7559.733
7	3	5	←	6	3	4	14	2	←	12	2	20.1	7561.6121	0.03884	7561.5733
7	3	4	←	6	3	3	14	0	←	12	0	20.1	7561.8982	-0.02064	7561.9188
8	4	4	←	7	4	3	16	4	←	14	4	20.1	8634.305	-0.03924	8634.3442
8	5	4	←	7	5	3	16	2	←	14	2	20.1	8634.8534	-0.03368	8634.8871
8	4	4	←	7	4	3	16	2	←	14	2	20.1	8635.4971	-0.06189	8635.559
8	4	5	←	7	4	4	16	4	←	14	4	20.1	8639.1449	-0.05968	8639.2046
8	3	6	←	7	3	5	16	0	←	14	0	20.1	8642.2205	-0.01844	8642.2389
9	5	4	←	8	5	3	18	2	←	16	2	20.1	9713.1252	-0.04361	9713.1688
9	5	5	←	8	5	4	18	0	←	16	0	20.1	9714.1981	-0.03303	9714.2311
9	5	5	←	8	5	4	18	2	←	16	2	20.1	9715.271	-0.024	9715.295
9	4	5	←	8	4	4	18	2	←	16	2	20.1	9718.3228	0.08273	9718.2401
9	4	6	←	8	4	5	18	0	←	16	0	20.1	9718.9903	-0.01458	9719.0049
9	3	7	←	8	3	6	18	0	←	16	0	20.1	9725.9998	0.10231	9725.8975
9	3	6	←	8	3	5	18	0	←	16	0	20.1	9735.0836	-0.04161	9735.1252
10	5	6	←	9	5	5	20	0	←	18	0	20.1	10795.6171	-0.07844	10795.6955
10	4	6	←	9	4	5	20	6	←	18	6	20.1	10800.5285	0.01	10800.5185
10	4	6	←	9	4	5	20	4	←	18	4	20.1	10801.1961	0.05656	10801.1395
10	4	7	←	9	4	6	20	4	←	18	4	20.1	10803.6757	0.07546	10803.6002
10	4	7	←	9	4	6	20	6	←	18	6	20.1	10804.2955	0.07323	10804.2223
10	3	7	←	9	3	6	20	4	←	18	4	20.1	10825.2764	0.10099	10825.1754
10	3	7	←	9	3	6	20	0	←	18	0	20.1	10825.8724	-0.11145	10825.9839
11	6	6	←	10	6	5	22	0	←	20	0	20.1	11873.1022	-0.08578	11873.188
11	5	6	←	10	5	5	22	4	←	20	4	20.1	11876.6546	-0.01737	11876.672
11	5	6	←	10	5	5	22	2	←	20	2	20.1	11877.2745	0.02262	11877.2519
11	5	7	←	10	5	6	22	2	←	20	2	20.1	11878.4428	0.03082	11878.412
11	5	7	←	10	5	6	22	4	←	20	4	20.1	11878.9911	-0.00108	11878.9922
11	5	7	←	10	5	6	22	6	←	20	6	20.1	11879.611	0.03851	11879.5725
11	5	7	←	10	5	6	22	8	←	20	8	20.1	11880.1832	0.03031	11880.1529

11	4	7	←	10	4	6	22	4	←	20	4	20.1	11885.8337	-0.00598	11885.8397
11	4	7	←	10	4	6	22	0	←	20	0	20.1	11887.0974	0.00885	11887.0885
11	3	9	←	10	3	8	22	6	←	20	6	20.1	11895.6327	-0.13743	11895.7701
12	6	6	←	11	6	5	24	4	←	22	4	20.1	12953.5913	-0.00634	12953.5976
12	5	7	←	11	5	6	24	2	←	22	2	20.1	12960.2194	-0.03687	12960.2563
12	5	8	←	11	5	7	24	2	←	22	2	20.1	12961.1254	-0.02335	12961.1488
12	5	8	←	11	5	7	24	4	←	22	4	20.1	12961.6261	0.0309	12961.5952
12	5	8	←	11	5	7	24	6	←	22	6	20.1	12962.0314	-0.0103	12962.0417
12	5	8	←	11	5	7	24	8	←	22	8	20.1	12962.5082	0.01992	12962.4883
12	3	9	←	11	3	8	24	12	←	22	12	20.1	13018.5366	0.12188	13018.4147
12	3	9	←	11	3	8	24	10	←	22	10	20.1	13018.775	0.07004	13018.705
12	3	9	←	11	3	8	24	8	←	22	8	20.1	13019.0372	0.08889	13018.9483
12	3	9	←	11	3	8	24	6	←	22	6	20.1	13019.2518	0.1104	13019.1414
12	3	9	←	11	3	8	24	4	←	22	4	20.1	13019.371	0.08955	13019.2815
13	7	7	←	12	7	6	26	0	←	24	0	20.1	14032.1732	0.0044	14032.1688
13	6	8	←	12	6	7	26	0	←	24	0	20.1	14036.6554	-0.04226	14036.6977
13	6	8	←	12	6	7	26	2	←	24	2	20.1	14037.0846	-0.03405	14037.1186
13	6	8	←	12	6	7	26	4	←	24	4	20.1	14037.5376	-0.00179	14037.5394
13	6	8	←	12	6	7	26	6	←	24	6	20.1	14037.9667	0.00653	14037.9602
13	6	8	←	12	6	7	26	8	←	24	8	20.1	14038.372	-0.00899	14038.381
13	5	9	←	12	5	8	26	2	←	24	2	20.1	14044.6663	-0.06212	14044.7284
13	5	9	←	12	5	8	26	6	←	24	6	20.1	14045.4054	-0.02505	14045.4304
13	5	9	←	12	5	8	26	8	←	24	8	20.1	14045.763	-0.01845	14045.7814
13	5	9	←	12	5	8	26	10	←	24	10	20.1	14046.073	-0.0595	14046.1325
7	4	3	←	6	4	2	14	4	←	12	4	20.1	7551.6786	0.00521	7551.6734
8	2	7	←	7	2	6	16	0	←	14	0	20.1	8606.0762	0.00752	8606.0687
8	2	7	←	7	2	6	16	4	←	14	4	20.1	8606.1716	0.00666	8606.1649
8	2	7	←	7	2	6	16	8	←	14	8	20.1	8606.5292	0.07669	8606.4525
8	2	7	←	7	2	6	16	10	←	14	10	20.1	8606.7677	0.1007	8606.667
8	2	7	←	7	2	6	16	12	←	14	12	20.1	8606.9822	0.05442	8606.9278
8	2	7	←	7	2	6	16	14	←	14	14	20.1	8607.1491	-0.08497	8607.2341
8	2	6	←	7	2	5	16	0	←	14	0	20.1	8734.87	-0.05868	8734.9287
8	2	6	←	7	2	5	16	6	←	14	6	20.1	8734.7269	0.00666	8734.7202
8	2	6	←	7	2	5	16	8	←	14	8	20.1	8734.6077	0.04886	8734.5588
8	2	6	←	7	2	5	16	10	←	14	10	20.1	8734.2739	-0.07832	8734.3522
8	2	6	←	7	2	5	16	14	←	14	14	20.1	8733.7732	-0.03294	8733.8061
10	5	6	←	9	5	5	20	2	←	18	2	20.1	10796.4039	-0.06697	10796.4709
10	5	6	←	9	5	5	20	0	←	18	0	20.1	10795.6171	-0.07844	10795.6955
10	5	5	←	9	5	4	20	2	←	18	2	20.1	10794.878	-0.04633	10794.9243
10	6	5	←	9	6	4	20	0	←	18	0	20.1	10792.16	-0.05146	10792.2115
11	3	8	←	10	3	7	22	4	←	20	4	20.1	11920.2093	0.00086	11920.2084
11	3	8	←	10	3	7	22	0	←	20	0	20.1	11920.4044	-0.10121	11920.5056

D.3 TWIST ANGLE ANALYSIS

A relaxed potential energy surface (PES) scan of the PBN ring torsional angle (ϕ) was performed using M05-2X DFT (keyword *Int=Ultrafine*)[2] and 6-31+G* basis set, over the angle range ϕ = 0° to ϕ = 90° in 3° increments. The energies of these 31 structures, along with the energy of the overall minimum energy geometry, were extrapolated over 360°, plotted *vs*. the torsional angle ϕ, and fit to an expansion of torsional potential functions shown in Eq. D-1.

Equation D-1

$$V(\phi) = \sum_n \left[\frac{V_n}{2}(1 - \cos n\phi) \right] + C_\tau$$

Also included in Eq. D-1 is a constant, C_τ. The following terms were derived from the PES scan; V_2 = 535, V_{4+} = -410, V_{4-} = -410, V_8 = -81, and C_τ = 1088 cm^{-1}. Phase shifts of ± 35.3° were applied to the V_4 terms, identified above as V_{4+} and V_{4-}, respectively. The theoretical barrier to ring planarity at ϕ = 0° is $V''(0)$ = 469 cm^{-1}, whereas the barrier to ring perpendicularity at ϕ = 90° is $V''(90)$ = 1003 cm^{-1}. The standard deviation between the PES function and the energies of all 125 calculated structures is 28 cm^{-1}. The PES is illustrated in Fig. D-4.

A plot of the inertial defect ($\Delta I = I_c - I_a - I_b$) in units of uÅ^2 *vs*. ring torsional angle ϕ for all 32 geometries (ϕ = 0 to 90°) is shown in Fig. 6-5 of the main text. The data points were fit to a 2nd order polynomial in order to determine the ϕ angle that best fit the experimentally determined ΔI in S_0. The best fit value of ϕ″ = 32° occurs for a structure with ΔI_{calc} = -21.5 uÅ^2.

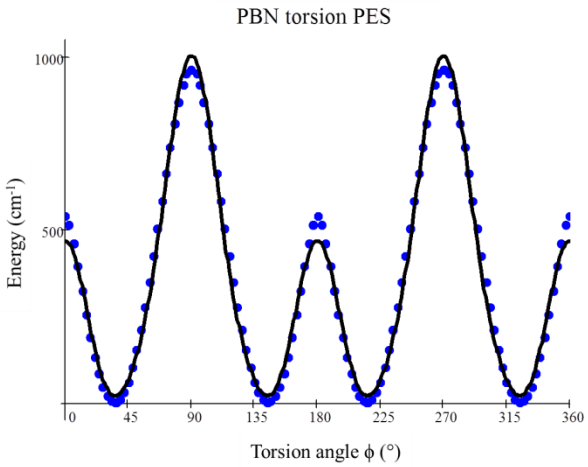

Figure D-4. The ground state PES for ring torsion in PBN is shown in black. Data points rendered blue were calculated at the M05-2X/6-31+G* level from $\phi = 0°$ to $\phi = 90°$, and then extrapolated over the entire 360° shown above.

The excited state torsion, or twist, angles ϕ' were also estimated from the ground state plot of ΔI vs. ϕ for Bands 1, 2, and 3. The measured inertial defects of PBN Bands 1, 2, and 3 are -6.97 (average of red and blue bands), -6.70, and -4.50 uÅ^2, respectively (*cf*. Table 6-1). The resulting ring torsional angles are 14° for Band 1, 13° for Band 2, and 9° for Band 3. To justify the use of a ground state ΔI vs. ϕ plot like that in Fig. 6-5 to determine excited state parameters, we assume that the light-induced changes in the individual ring geometries are negligible compared to the extreme changes in ring twist angles indicated by the drastic changes in ΔI. For comparison, $\phi' = 20°$ was determined in the same fashion for PP using Eq. D-1 and Figs. D-5 and D-6. This value compares favorably with $\phi' = 19.8°$ previously determined from a FC analysis of the vibrationally resolved FES[6] and $\phi' = 20.9°$ calculated at the SA-CASSCF level.[7]

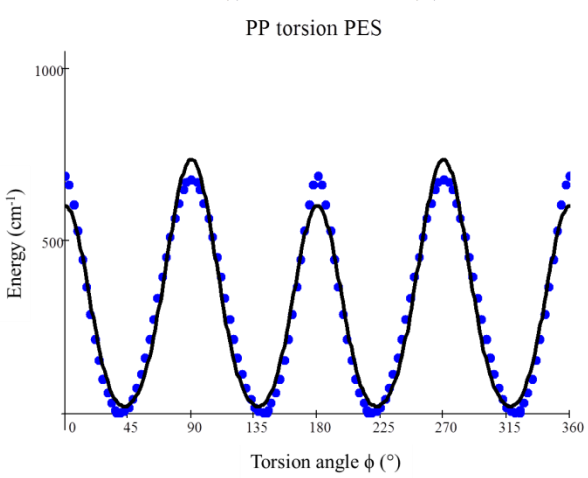

Figure D-5. The ground state PES for ring torsion in PP is shown in black. Data points rendered blue were calculated at the M05-2X/6-31+G* level from $\phi = 0°$ to $\phi = 90°$, and then extrapolated over the entire 360° shown above. The following Eq. D-1 parameters were fit to the blue data points: V_2 = 67, V_{4+} = -210, V_{4-} = -210, V_8 = -38, and C_τ = 698 cm^{-1}. For PP, the V_4 shift is 39.65°.

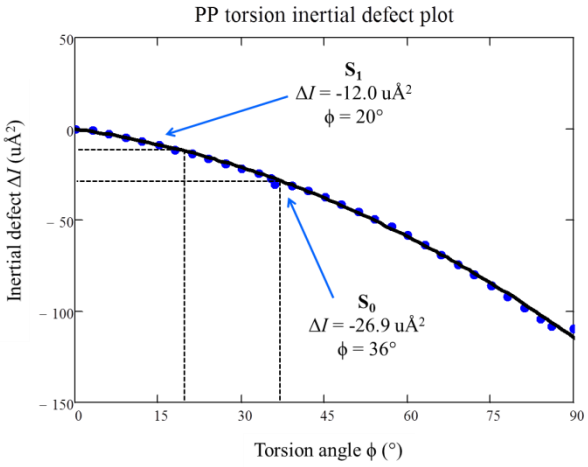

Figure D-6. Plot of ΔI vs. ϕ as calculated from the ground state torsional PES shown in Fig. D-5 (blue data points). These data points were fit to a 2nd order polynomial (black curve), and used to determine ϕ for all PP electronic states. The S_0 and S_1 extrapolations are shown in the figure.

While the inertial defect plots in Figs. 6-5 and D-6 are good representations of the ground and excited states, the potential energy surfaces in Figs. D-4 and D-5 clearly are not. In PBN, the minimum excited state twist angle for Band 1 is 14°, much smaller than the value of 32° found in S_0. Therefore, we believe that the splitting found in band 1 is a consequence of hindered internal rotation about the bond connecting the two unsaturated rings in the excited (S_1) state. The corresponding splitting in the S_0 state is likely to be much smaller, since the effective barrier height in the ground S_0 state is likely to be much larger, owing to the larger separation of the two minima.[8] We note that at +400 cm^{-1}, the molecule must exist above this barrier, while still remaining well below the larger barrier to perpendicularity.

D.4 DIPOLE CORRELATION ANALYSIS

During the Stark spectral fitting process in PBN Band 2, μ'' was fixed at different values ranging from 2.5 to 4.1 D, necessitating a matching range of $\mu' = 5.0$ to 6.8 D to reproduce the experimental splitting in the Stark spectra. The high linear correlation observed between μ in S_0 and S_2 is plotted in Fig. D-7. A best fit to the trendline $\mu' = 1.0765\mu'' + 2.325$ (units of Debye, D) with $R^2 = 0.9978$ was obtained, where a double-prime ($''$) denotes a ground state parameter (S_0), and a prime ($'$) denotes an excited state parameter (S_x, x = 1 or 2). For Band 3, μ'' was set at values ranging from 2.4 to 4.4 D, requiring S_2 dipole moments that range from $\mu' = 5.2$ to 7.5 D to maintain a fit of the experimental spectrum. The best fit trendline for Band 3 is $\mu' = 1.1827\mu'' + 2.2725$ with an $R^2 = 0.9988$, and is also shown in Fig. D-7.

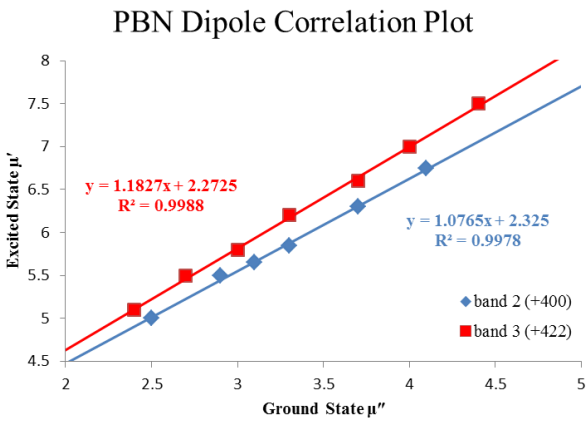

Figure D-7. Linear dipole function for PBN, showing the high correlation between the measured μ″ and μ′ values determined for PBN band 2 (blue diamonds) and PBN band 3 (red squares).

To determine reliable values of μ′, the structure of PBN was optimized with the ring torsion angle frozen at 32° (*A* = 3508.8, *B* = 383.4, *C* = 351.1 MHz; Δ*I* = -22.1 uÅ^2 from theory), and the dipole moment of this "experimentally derived" structure was determined *via* an MP2/aug-cc-pVTZ single point calculation to be μ″ = 3.43 D. Inserting the value of μ″ = 3.43 D into the experimentally determined linear dipole functions shown in Fig. D-7 leads to μ′(L_a) = 6.02(10) D for Band 2, and μ′(L_a) = 6.33(10) D for Band 3 in PBN. This approach of carrying out a single point calculation using MP2/aug-cc-pVXZ (X = D, T, or Q) on a geometry optimized using hybrid density functional theory has been shown to reliably reproduce accurate S_0 permanent EDMs at minimal computational cost in previous work[9] and for the family of ICT molecules listed in Table D-3.

Table D-3. Calculated rotational constants (*A*, *B*, *C*) in MHz are compared to the experimentally determined values below. Following the M05-2X/6-31+G* optimization, the dipole moment was calculated using MP2 theory (keywords *SCF=Tight* and *Density=Current*)[2] and either a double-ζ (D), triple-ζ (T), or quadruple-ζ (Q) basis set of the form aug-cc-pVXZ where X = D, T, or Q. The percent error in calculated parameters is shown in the column "%". The molecules investigated are abbreviated as follows: AN = aniline,[10] BN = benzonitrile,[11] ABN = 4-aminobenzonitrile,[11] DMABN = 4,4′-dimethylaminobenzonitrile, PYR-eq = pyrrolidine (equatorial conformer),[12] PYRBN = 4-(1-pyrrolidinyl)benzonitrile, P = pyrrole,[13] PP = 1-phenylpyrrole,[14] and PBN = 4-(1*H*-pyrrol-1-yl)benzonitrile.

	AN					BN					ABN				
	Exp	M052X	%	MP2	%	Exp	M052X	%	MP2	%	Exp	M052X	%	MP2	%
A	5618.1	5642.0	0.4			5656.7	5676.0	0.3			5579.3	5596.7	0.3		
B	2594.2	2600.9	0.3			1547.4	1549.3	0.1			990.3	992.1	0.2		
C	1777.2	1783.0	0.3			1214.8	1217.1	0.2			841.4	843.1	0.2		
μ_a	1.13	1.17	3.2	1.14	1.0	4.48	4.76	6.3	4.48	0.1	6.41	6.72	4.8	6.31	1.5

	DMABN					PYR-eq					PYRBN				
	Exp	M052X	%	MP2	%	Exp	M052X	%	MP2	%	Exp	M052X	%	MP2	%
A	3469.3	3469.0	0.0			6864.7	6911.0	0.7			3083.0	3097.6	0.5		
B	578.6	581.0	0.4			6792.0	6822.8	0.5			366.1	366.7	0.2		
C	499.6	501.0	0.3			3902.3	3923.5	0.5			331.8	332.3	0.2		
			Q										Q		
			T										T	8.08	2.1
μ_a	6.426	7.85	22.2	7.49	16.5		0.05	###	0.08	###	8.23	8.46	2.8	8.06	2.1

	P					PP					PBN				
	Exp	M052X	%	MP2	%	Exp	M052X	%	MP2	%	Exp	M052X	%	MP2	%
A	9130.6	9188.2	0.6			3508.3	3525.7	0.5			3492.2	3508.2	0.5		
B	9001.3	9042.4	0.5			703.5	703.9	0.1			382.6	383.3	0.2		
C	4532.1	4557.4	0.6			604.8	608.8	0.7			350.0	351.6	0.5		
			Q	-1.86	7.1			Q					Q		
			T	-1.87	7.4			T					T		
μ_a	-1.74	-1.99	14.6	-1.90	9.3	-1.56	-1.75	12.1	-1.78	13.9		3.71	###	3.43	###

Table D-3 shows an excellent overall correlation between theory and experiment when determining rotational constants and EDMs in this fashion. While the EDM of BN is in excellent agreement, the calculation slightly overestimates the total EDM of pyrrole (P). Therefore, the value of 3.43 D calculated for PBN may be a slight underestimate of the experimental ground state value. This would, in turn, yield a slight underestimate of the excited S_2 state value reported in this work. This effect is small, with a percentage error of no more than 15% (~ 0.5 D in S_0).

D.5 REFERENCES

1. Y. Zhao, N. E. Schultz, and D. G. Truhlar, *J. Chem. Theory Comput*. **2**, 364 (2006).

2. M. J. Frisch, G. W. Trucks, H. B. Schlegel, G. E. Scuseria, M. A. Robb, J. R. Cheeseman, J. Montgomery, J. A., T. Vreven, K. N. Kudin, J. C. Burant, J. M. Millam, S. S. Iyengar, J. Tomasi, V. Barone, B. Mennucci, M. Cossi, G. Scalmani, N. Rega, G. A. Petersson, H. Nakatsuji, M. Hada, M. Ehara, K. Toyota, R. Fukuda, J. Hasegawa, M. Ishida, T. Nakajima, Y. Honda, O. Kitao, H. Nakai, M. Klene, X. Li, J. E. Knox, H. P. Hratchian, J. B. Cross, V. Bakken, C. Adamo, J. Jaramillo, R. Gomperts, R. E. Stratmann, O. Yazyev, A. J. Austin, R. Cammi, C. Pomelli, J. W. Ochterski, P. Y. Ayala, K. Morokuma, G. A. Voth, P. Salvador, J. J. Dannenberg, V. G. Zakrzewski, S. Dapprich, A. D. Daniels, M. C. Strain, O. Farkas, D. K. Malick, A. D. Rabuck, K. Raghavachari, J. B. Foresman, J. V. Ortiz, Q. Cui, A. G. Baboul, S. Clifford, J. Cioslowski, B. B. Stefanov, G. Liu, A. Liashenko, P. Piskorz, I. Komaromi, R. L. Martin, D. J. Fox, T. Keith, M. A. Al-Laham, C. Y. Peng, A. Nanayakkara, M. Challacombe, P. M. W. Gill, B. Johnson, W. Chen, M. W. Wong, C. Gonzalez, and J. A. Pople, GAUSSIAN 03, Revision C.02 (Gaussian, Inc., Wallingford, CT, 2004).

3. T. H. Dunning Jr. and P. J. Hay, in *Modern Theoretical Chemistry*, edited by H. F. Schaefer III, (Plenum, New York, 1977), Vol. 3, p. 1.

4. Z. Kisiel, J. Kosarzewski, B. A. Pietrewicz, and L. Pszczolkowski, *Chem. Phys. Lett*. **325**, 523 (2000).

5. Z. Kisiel, E. Bialkowska-Jaworska, O. Desyatnyk, B. A. Pietrewicz, and L. Pszczolkowski, L. *J. Mol. Spectrosc.* **208**, 113 (2001).

6. K. Okuyama, Y. Numata, S. Odawara, and I. Suzuka, *J. Chem. Phys*. **109**, 7185 (1998).

7. I. F. Galván, M. E. Martín, A. Muñoz-Losa, M. L. Sánchez, and M. A. Aguilar, *J. Chem. Theory Comput*. **7**, 1850 (2011).

8. W. Gordy and R. L. Cook, *Microwave Molecular Spectra,* 2nd ed. (John Wiley & Sons, New York, 1984).

9. A. J. Fleisher, J. W. Young, D. W. Pratt, A. Cembran, and J. Gao, *J. Chem. Phys*. **134**, 114304 (2011).

10. D. G. Lister, J. K. Tyler, J. H. Høg, and W. Larsen, *J. Mol. Struct*. **23**, 253 (1974).

11. D. R. Borst, T. M. Korter, and D. W. Pratt, *Chem. Phys. Lett*. **305**, 485 (2001).

12. W. Caminati, A. Dell'Erba, G. Maccaferri, and P. G. Favero, *J. Mol. Spectrosc*. **191**, 45 (1998).

13. L. Nygaard, J. T. Nielsen, J. Kirchheiner, G. Maltesen, J. Rastrup-Andersen, and G. O. Sørensen, *J. Mol. Struct*. **3**, 491 (1969).

14. J. A. Thomas, J. W. Young, A. J. Fleisher, L. Alvarez-Valtierra, and D. W. Pratt, *J. Phys. Chem. Lett.* **1**, 2017 (2010).

APPENDIX E

SUPPORTING INFORMATION FOR CHAPTER 7.0

Table E-1. Observed frequencies and residuals for the rotational transitions of *syn*-2-(2′-pyridyl)pyrrole.

$J^{'}$	$K_{-1}^{'}$	$K_{+1}^{'}$	$J^{''}$	$K_{-1}^{''}$	$K_{+1}^{''}$	Obs. / MHz	Obs.-calc. / MHz
5	1	5	4	1	4	6205.55	-0.007
5	0	5	4	0	4	6444.55	0.029
5	2	5	4	2	4	6793.28	0.000
6	1	6	5	1	5	7437.84	-0.006
6	0	6	5	0	5	7696.41	0.015
6	2	6	5	2	5	8141.02	-0.014
7	0	7	6	0	6	8930.80	0.008
8	0	8	7	0	7	10147.90	0.002
9	0	9	8	0	8	11349.50	-0.016